Dipl.-Ing. Florian NIEDERMAYR, BSc.

HUMAN THERMOREGULATION MODEL OF RF-EMF INTERACTION

DOCTORAL THESIS

for obtaining the academic degree of
Doktor der technischen Wissenschaften

Doctoral School Electrical Engineering
Biomedical Engineering

Advisor:
Univ.-Prof. Dipl.-Ing. Dr. N. Leitgeb

Institute of Health Care Engineering with European Testing Institute

Graz, April 2012

STATUTORY DECLARATION

I declare that I have authored this thesis independently, that I have not used other than the declared sources / resources and that I have explicitly marked all material which has been quoted either literally or by content from the used sources.

…… ……..

date (signature)

für Karin

Abstract

A thermal model has been developed which allows accurate temperature computations in high resolution anatomical models. The model is based on the basic thermal model described by Pennes which neglects any of the thermoregulatory mechanisms in humans. The thermal model developed here overcomes major simplifications by the mathematical consideration of these mechanisms which is needed for modeling a physiologically correct reaction to a thermal stimulus. The local blood perfusion, as well as the local metabolic rate, is modified as a function of the local tissue temperature. The model implemented increases the blood temperature on the basis of the absorbed energy. The heat exchange at the tissue/air interface, including the skin and respiratory tract, is also improved. The model takes not only the heat dissipation by radiation, conduction and convection into consideration but also the insensible loss of water by evaporation. Furthermore, the thermal model also accounts for the active heat dissipation by sweating. The generic implementation of the thermal model makes it possible to use it for different human models (children, adults, pregnant women) and it is also possible to take implants into consideration. The performance of the model is validated by comparing the simulation results to actual temperature measurements in humans.

The thermal model is used to compute the temperature elevation in humans exposed to radiofrequency electromagnetic fields. Until now, the tissue heating caused by radiofrequency electromagnetic fields could only be estimated by a surrogate, namely the specific absorption rate. The temperature elevations in children of different sizes and ages as well as pregnant women at different gestational stages exposed to plane waves is computed. Furthermore, the temperature elevation in human bodies is computed for a diagnostic modality (magnetic resonance imaging) and a therapeutic modality (medical diathermy).

Keywords: *anatomical models, dosimetry, numerical simulations, Pennes equation, thermoregulatory model*

Kurzfassung

Ein thermisches Modell wurde entwickelt, welches Temperaturberechnungen in hochauflösenden anatomischen Modellen ermöglicht. Das Modell basiert auf einem vereinfachten thermischen Modell das von Pennes entwickelt wurde und sämtliche thermoregulatorische Mechanismen vernachlässigt. Das in dieser Arbeit entwickelte Modell beseitigt diese Vereinfachungen durch die mathematische Berücksichtigung dieser Mechanismen, um eine physiologisch korrekte Reaktion auf einen thermischen Stimulus modellieren zu können. Dazu wird die Durchblutung als auch die Stoffwechselrate in Abhängigkeit der lokalen Temperatur variiert. Die Bluttemperatur wird als Funktion der absorbierten Energie erhöht. Der Wärmeaustausch an der Gewebe/Luft-Grenzschicht, dies umfasst sowohl die Haut als auch den Atemtrakt, wurde ebenfalls verbessert. Das Modell berücksichtigt nun nicht nur den Wärmeverlust durch Strahlung, Konduktion und Konvektion, sondern auch den Wasserverlust durch Verdunstung. Außerdem wird mit dem thermischen Modell die aktive Wärmeabgabe durch Schwitzen berücksichtigt. Durch die generische Implementierung des thermischen Modells kann es an unterschiedlichsten Modellen (Kindern, Erwachsenen, Schwangeren) eingesetzt werden, eine Berücksichtigung von Implantaten ist ebenfalls möglich. Die Performance des Modells wird durch den Vergleich der Simulationsergebnisse mit tatsächlichen Temperaturmessungen validiert.

Das thermische Modell wird dazu verwendet, die Temperaturerhöhung in Humanmodellen zu berechnen, die gegenüber hochfrequenten elektromagnetischen Feldern exponiert sind. Bis jetzt konnte die Gewebserwärmung durch hochfrequente elektromagnetische Felder nur indirekt über ein Surrogat, nämlich der spezifischen Absorptionsrate, bestimmt werden. Die Temperaturerhöhung im Körperinneren bei Kindern unterschiedlichen Alters und Größe und bei schwangeren Frauen in unterschiedlichen Schwangerschaftsstadien, exponiert gegenüber ebenen Wellen, wurde berechnet. Außerdem wurde die Temperaturerhöhung in digitalen Humanmodellen für eine diagnostische Behandlungsmethode (Magnetresonanztomographie) und eine therapeutische Behandlungsmethode (Diathermie) berechnet

Schlüsselwörter: *anatomische Modelle, Dosimetrie, numerische Simulation, Pennes Gleichung, thermoregulatorisches Modell*

TABLE OF CONTENTS

Table of Symbols

Symbols	Definition	Description
A	W/m^3	metabolic rate
C	kJ/(kg°C)	specific heat capacity
E	V/m	electric field strength
H	A/m	magnetic field strength
H	W/(m²°C)	heat transfer coefficient
J	A/m^2	current density
K	W/(m°C)	thermal conductivity
P_{ext}	W	water loss through the skin
P_{ins}	W	insensible water loss
P_{int}	W	water loss through the lungs
PLD	W/m^3	power loss density
SAR	W/kg	specific absorption rate
SAR_{10g}	W/kg	localized specific absorption rate averaged over any 10g contiguous tissue
SAR_{WB}	W/kg	whole body specific absorption rate
SW	W/m²	heat loss due to sweating
ε	F/m	permittivity
μ	H/m	magnetic permeability
ρ	kg/m^3	mass Density

List of Abbreviations

ASD	Applicator Skin Distance
BHT	Bioheat Transfer
CFL	Courant-Friedrichs-Levy
CNS	Central Nervous System
CST	CST Studio Suite 2011®
CT	Computer Tomography
DLL	Dynamic Link Library
EMF	Electromagnetic Field
GUI	Graphical User Interface
ICNIRP	International Commission of Non-Ionizing Radiation Protection
M	Material Matrix
MGE	Maxwell's Grid Equations
MRI	Magnetic Resonance Imaging
RF	Radio Frequency
SWD	Short Wave Diathermy
UFO	Uterofetal Unit
US	Ultrasound
VBA	Visual Basic
WHO	World Health Organization

1. Introduction

1.1. Preface

The use of electronic devices emitting radio frequency (RF) electromagnetic fields is still increasing exponentially. This includes electromagnetic sources in every-day life such as cell phones or electronic article surveillance systems. The electromagnetic fields (EMF) of these sources are usually low. Considerably higher fields are used for medical applications (e.g. medical resonance imaging, medical diathermy) or at certain workplaces (e.g. dielectric and induction heating).

Therefore, limiting values have been proposed to restrict RF-EMF exposure and protect people from adverse health effects. The compliance with such RF-EMF exposure limits can be assured by measurements. This approach is, in general, rather complex as, due to the disparity of the sources covering a wide frequency range, several measuring instruments might be needed. The complexity increases even further if measurements in the near field region of the source have to be performed. The biggest constraint with regard to measurements is its very limited ability to measure the field quantities within the human body.

An alternative method to evaluate the RF-EMF exposure is numerical dosimetry. This method allows the computation of the field quantities in numerical human models.

Several off-the-shelf software packages are available on the market. They are able to compute the induced current density (J) and the specific absorption rate (SAR) of the internal organs and tissues with high accuracy over a wide frequency range for arbitrary exposure setups [1] [2].

The implementation of thermal models able to compute the induced temperature elevation caused by the absorbed RF-EMF energy deposition is still the subject of ongoing research efforts. In particular, the consideration of thermoregulatory reactions of the human body to external heat loads is still not sufficiently accounted for in the existing thermal models.

1.2. Objectives

The goal of this work is to develop a new thermoregulatory simulation model, capable of determining the temperature distribution and its elevation inside the body in a quantitative manner, by considering the thermoregulatory mechanisms of the human body.

The well-known and widely used Pennes equation is used as basis for this model. This model was originally designed to describe the heat balance in the upper arm and was later extended to describe the heat balance in the whole human body. This simplified thermal model has to be improved and extended by taking into account thermoregulatory mechanisms. The boundary conditions at the tissue/air interface should be better adapted to the physiological conditions. Therefore, the heat transfer at the skin and in the lungs, as well as the water loss through evaporation, has to be considered and the heat loss caused by sweating has to be taken into account. The thermal model should further be modified to account for the blood temperature elevation caused by external heat loads. In addition, the local blood perfusion as well as the local metabolic rate has to be modified as a function of the local tissue temperature. The model must be implemented as flexibly as possible so that it can be used for different human models (children, adults, pregnant women) and it should also be possible to take implants into consideration.

An accurate assessment of the RF-EMF energy induced temperature elevation should be possible on the basis of this model. The model and the results derived should be used to demonstrate the compliance with the RF-EMF exposure limits.

The first chapter of this work describes the basic thermoregulatory mechanisms in humans and the interaction mechanisms of RF-EMF fields and the human body. In addition, the RF-EMF exposure limits are explained with a special focus on the relation between SAR and temperature elevation. In the second chapter, the simulation methods for both the thermal and the electromagnetic simulations are described in detail. The human models used and the basis for the electrical and thermal tissue properties are also described. The third chapter gives an overview of the uncertainty budgets associated with numerical simulations. The validation of the electromagnetic and thermal simulations is realized in the fourth chapter.

Finally, chapters five through nine present first meaningful results for various exposure scenarios based on the developed thermal model.

1.3. Thermoregulation in the Human Body

Humans have the capability to keep their core temperature within a small margin of variation, close to 37°C, even under varying ambient conditions. The processes regulating the heat dissipation to the environment have therefore to be controlled in order to adapt to the climatic environment [3].
The dissipation of heat is the most important control mechanism regulating the thermal control loop in humans [4]. The body can protect itself against hyperthermia or hypothermia by controlling the heat losses, these processes can be summarized as the so called physical control mechanisms. Additionally, heat can be produced by chemical control mechanisms if the temperature falls below a certain level [5].

1.3.1. Heat production

Most of the heat in the human body is produced as a byproduct of metabolic processes. The metabolic rate and, as a result the heat production, varies with the work load, the ambient temperature, the food uptake and the day time. In addition to this, each muscle motion contributes to the overall heat production by friction energy [6].
The specific heat production of organs and tissues has been measured indirectly by their weight and oxygen uptake. It has been shown that 59% of the metabolism at rest occurs in the body core including the cranial, chest and abdominal cavities, although they represent only 8% of the total body weight [6]. The coronal plane in Figure 1-1 highlights the core area with a pronounced higher heat production, clearly differentiated from the surrounding muscle and skin, which makes up of 52% of the body weight but contributes only 28% to the overall heat production [5]. The concentration of the heat production in the body core helps to keep the core temperature constant during rest. These values change dramatically during work, resulting in a dominant, primarily superficial heat production in the muscles which facilitates the dissipation of heat to the environment [3].

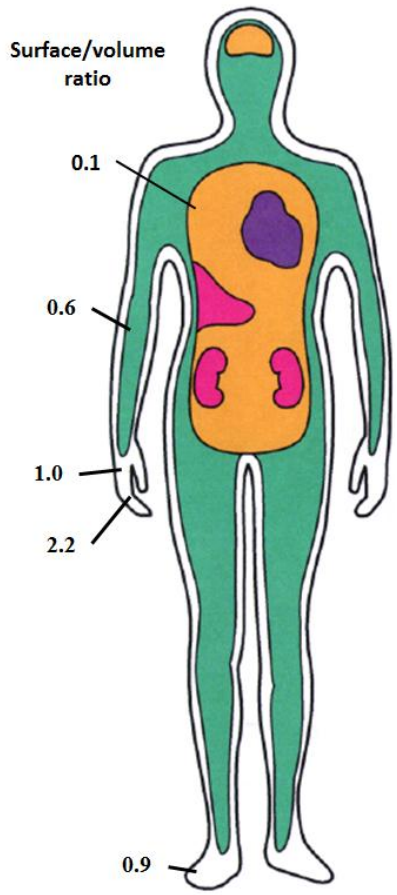

Portion of the heat production in %	rest	work
Brain	**18**	**3**
Chest and abdominal cavity	**41**	**22**
Muscle	**26**	**72 (up to 90%)**
Skin	**2**	**1**
Rest of the body	**13**	**2**

metabolic heat production in W/kg			
	23		***5***
	17		**2**
	10		

Figure 1-1: Topography of the heat production in the human body together with the relative and absolute heat production in different body regions **[7]**.

1.3.2. Skin temperature

The skin temperature is strongly related to the ambient temperature, with low skin temperatures at low ambient temperatures. The skin temperature is lower than the core temperature and decreases in proportion to its distance from the heat producing body core [8]. The disparity in the ratio between surface and volume (see left side of Figure 1-1) of different body parts further amplifies this effect, leading to the lowest skin temperatures in body protrusions such as the fingers and toes. The temperature field for a naked human is shown in Figure 1-2. The figure shows that the isothermal 37°C region is concentrated in the body core for low ambient temperatures and expands towards the extremities at higher temperatures.

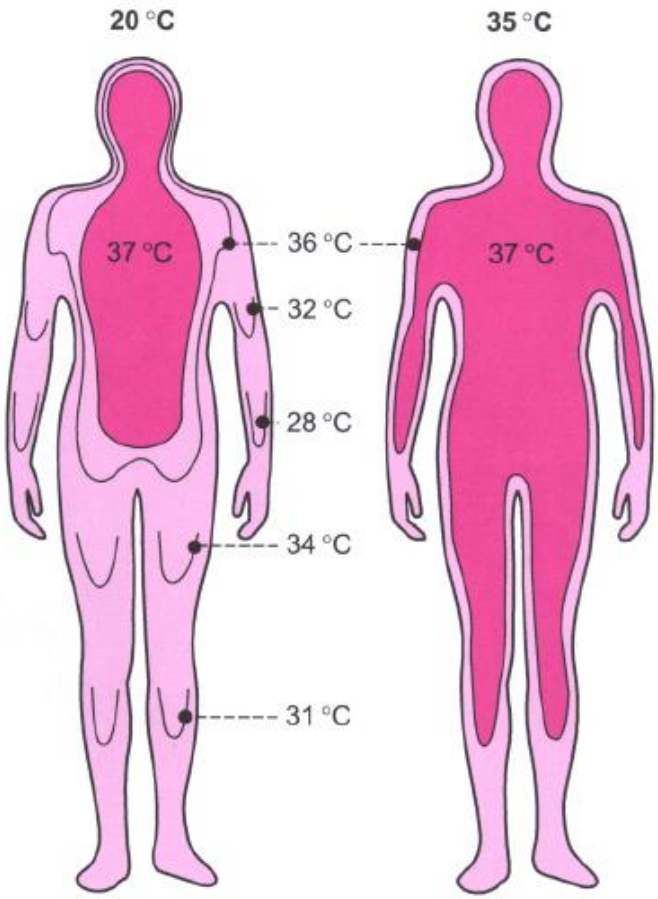

Figure 1-2: Isothermal regions in a naked human for an ambient room temperature of 20°C and 35°C **[3]**.

These effects do not only result in lower surface temperatures in the extremities but lead also to a faster fall in the temperature in these regions compared to the trunk and head if the ambient temperature declines [8].

The skin temperatures of the different body regions approach each other as the ambient temperature increases and exceed the core temperature in a naked man at rest at an ambient temperature of 40°C [3]. This inversion of the temperature gradient results in heat uptake by the body from the environment. The onset of sweating counteracts this mechanism [9].

1.3.3. Core temperature

The core temperature is almost constant at the center of the body with some characteristic deviations. The organs in the body core (e.g. liver, brain) are generally warmer than the arterial blood. Organs with a high metabolic rate are cooled down by the blood, leading to a warmer venous outflow compared to the arterial inflow [8]. In more superficial organs and tissue this effect is reversed, leading to a dissipation of heat from the warmer arterial blood to the environment. The most pronounced cooling of the blood is found in the extremities [5].

In general it is difficult to define a standardized place to measure the core temperature. The temperature in the rectum reacts slowly to external temperature changes, whereas the temperatures in the mouth and esophagus adapt faster to changing conditions although they may be affected by the breathing. It has been shown that the temperature of the eardrum can be used as an indirect measure of the brain temperature [8].

The core temperature of the organism varies throughout the day even under constant ambient conditions. The temperature in the extremities falls slightly during the day and the heat dissipation is throttled back which leads, in conjunction with a slightly elevated metabolic rate, to an increase in the core temperature. This effect is reversed in the evening. The stored heat is dissipated by increasing the skin temperature and decreasing the core temperature [8]. The peak-to-valley temperature variation of the temperature may be as high as 1.5°C, with distinct inter-individual variations [5] [3]. The average body core temperature of women is 0.44°C higher than in men, due to the menstrual cycle [10].

1.3.4. Heat dissipation

The heat produced in the human body is transferred by four physical processes [6]:

- **conduction:** heat transfer caused by a temperature gradient
- **convection:** heat transfer via a moving medium (e.g. gases or liquids)
- **radiation:** infrared radiation
- **evaporation:** heat loss through evaporation of water on the skin surface

The inner heat flow describes the heat transfer from its primary origin in the body core to the body surface and is mostly defined by conduction and convection. Conduction defines the heat flow in a medium in terms of the Brownian motion, trying to compensate for an existing temperature gradient. The heat conductivity coefficient (defined in W/(m°C)) of biological tissue is primarily defined by its water content [9]. The major heat transfer by conduction occurs in the capillary bed, at the blood-tissue interface [8]. The convection on the other side is the heat transfer caused by the flow of gases or liquids. This effect is dominated by the flowing blood, especially in the skin where the blood flow is controlled with a large range of variation and by that the outwards directed convective heat transfer [9].

Of crucial importance is also the counter flow principle in the extremities, where heat is delivered from the warmer blood in the arteries to the blood in the parallel located veins [11].

The external heat flow describes the heat dissipation at the skin and in the respiratory tract. Therefore, not only convection and conduction but also radiation and evaporation have to be considered [3]. Under normal conditions a resting air layer is created on the skin-air interface with good thermal isolation properties. The heat conduction is much lower than would be the case if the skin were to be in direct contact with solids or liquids. A swimmer, for example, has an approximately 200 times higher heat loss than if he were standing in the dry [9].

The temperature gradient at the skin-air interface leads to a slight air flow along the body axis, with the heated air ascending towards the head and being replaced by cooler air. The convection is dramatically increased with an impressed air flow, e.g. in wind or if the human runs [8]. The heat loss by radiation occurs in the form of electromagnetic waves in the infrared region and can be described by the Stefan- Boltzmann law [9].

The evaporation of water is the fourth mechanism by which heat is dissipated to the environment. The thermal energy is dissipated by the evaporation of water on the skin surface and the mucosa of the respiratory tract. 24 MJ are needed to evaporate 1l of water [9]. The evaporation of 0.5l of water is equals to ca. 1/6 of the overall heat production at rest during the day. The amount of heat that can be dissipated to the ambient is a function of the water vapor pressure on the skin surface and in the air. The water vapor pressure itself is a function of the temperature. This means that

even with an air humidity of 100%, heat can be transferred to the environment as long as the skin temperature is lower than the ambient temperature [6].

The contribution of the described mechanism to the overall heat dissipation is quite different. In the thermo-neutral region (27-32°C for naked humans [3]), 26% of the heat is dissipated by evaporation, whereas 18% is lost at the skin and the remaining 8% in the mucosa of the respiratory tract [12] [13]. Fifteen percent of the heat is lost through radiation, convection and conduction in the respiratory tract. The remaining 59% is dissipated at the skin surface, with 35% being lost through radiation and the remaining 24% by convection and conduction [5] [3] [9].

These values change dramatically if the ambient temperature increases. The evaporation of water remains the sole heat dissipating process if the ambient temperature exceeds 35°C [3]. In that case the direction of the heat transfer by conduction and convection is reversed, which means that the heat acquired through these processes has also to be dissipated by evaporation [3] [9].

1.3.5. Thermoregulation

The aim of the thermal regulation system in the human body is to stabilize the core temperature within a narrow range (36-38°C). The core temperature of humans is normally considerably higher than the ambient temperature, due to the metabolic processes and their high production rate of heat [8]. This ability ensures a high level of independence of the ambient climatic conditions and extends the potential habitat of humans [3].

The heat production of the organism in changing ambient conditions or due to work performed can alter the core temperature. The regulatory mechanisms try to counteract this effect and to achieve a balanced thermal budget where the heat production equals the heat dissipation [10].

The thermoregulatory system of humans can be described as a control system with several thermal sensors, linked controller centers and effectors which tries to increase or decrease the heat production and heat dissipation [9]. The effectors of the autonomic nervous system include the blood vessels in the skin and internal organs and their sympathetic, vasoconstrictive innervation, sweat glands with sympathetic innervation and, finally, the sympathetic innervation of the liver, muscles, fat, and adrenal medulla which increases the metabolic rate of these organs [10]. Additional

somatosensory effectors including skeletal muscles, respiratory muscles and thermoregulatory behavior (e.g. clothes, posture) are used to adapt the thermoregulation system of humans [9].

Thermal sensors are located in the skin and inside the body, controlling the thermoregulatory mechanisms [6]. The skin contains thermal sensors for cold and heat. The measured temperature is a function of their impulse frequency. The warm sensors cover the range from 25- 50°C, with a maximum at 38°C. The cold sensors cover the range from 15- 40°C [8]. The sum of all the signals from the cold and heat receptors defines the perceived temperature, which is a function of the included number of receptors and so that of the area covered [3]. The impulse frequency of cold sensors is three times higher compared to that of their heat counterparts and their local density is ten times higher, which leads to a dramatically higher perception of cold or decreasing temperatures [6]. This highlights the importance of the skin temperature measurement with regard to trigger actions to prevent hyperthermia. In general, cold stimuli lead to vasoconstriction and warm stimuli to a vasodilatation in the skin, the skin temperature also contributes to control of sweating [10].

The dominant internal thermoreceptors are located in the hypothalamus but their internal occurrence is not limited to this area [5]. Additional receptors are located in the spinal canal, in the vicinity of the esophagus, stomach, blood vessels and muscles [8]. The hypothalamus, however, dominates the internal temperature perception and the coordination of the thermoregulatory mechanisms. This not only includes the accurate adjustment of heat production and dissipation mechanisms but also the steering of behavior with regard to food uptake or adapting the posture [5].

Figure 1-3 illustrates the thermoregulatory control system of humans, including the previously defined mechanisms.

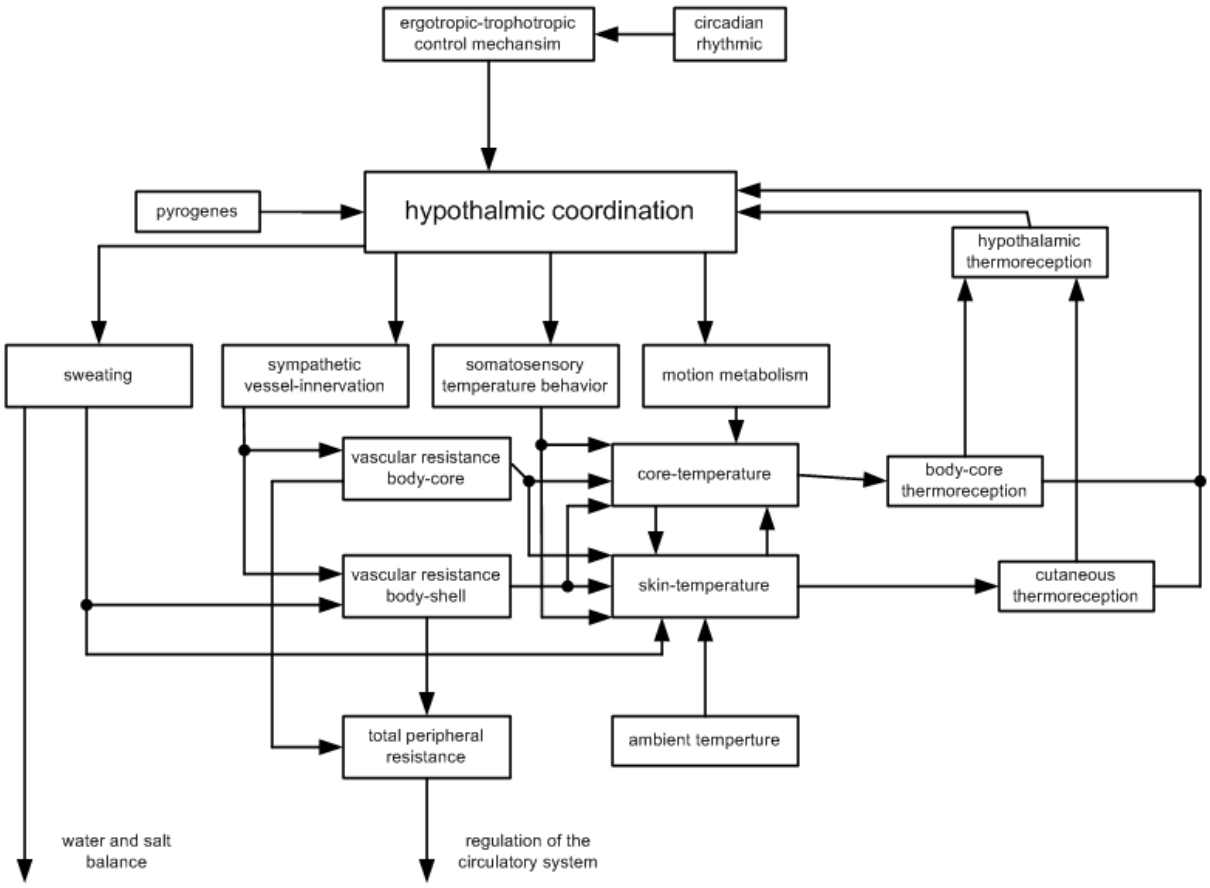

Figure 1-3: Thermoregulatory control system of the human organism [10] [3].

The body controls core temperature with a combination of different vegetative and somatosensory innervation. The adjustment of these mechanisms is based on the central consideration of the peripheral and central thermosensibility in the hypothalamus.

In the thermo-neutral region, at ambient temperatures of 27-32°C for naked and 18-22°C for clothed humans, the balance between heat production and dissipation is solely controlled by the vasoconstriction and vasodilatation of the vessels with the variation of the blood perfusion of the skin being the dominant factor [14].

The increase in the metabolic processes is initiated if the ambient temperature falls below the thermo-neutral region and this can be achieved by motor activity (e.g. muscle tension, shivering). Shivering increases the oxygen uptake and, by that, the heat production by a factor of up to five [8]. Moreover, heat dissipation is reduced by constriction of the skin blood vessels [5].

The thermoregulatory control system also reacts to an elevation of the ambient temperature above the thermo-neutral region or if the heat production is altered by physi-

cal activity [10]. The resultant temperature elevation leads to an increase in the activity level of the hypothalamus and activation of the heat dissipating mechanisms. This includes the vasodilatation of skin vessels, sensible water loss by sweating and behavioral adaptation (e.g. posture, changing clothes) [3]. Sweating stresses the salt and water balance of the organism. The water loss decreases the blood volume and, consequently, the internal heat transport capacity. The blood perfusion of the adrenal glands and urine production is reduced. This potential dehydration increases the core temperature: a loss of 1l of water equals a core temperature elevation of approximately 0.5°C [6]. The reduced physical and mental capacity is also attributed to the loss of water. The loss of electrolytes leads to muscle cramps, vomiting, dizziness and finally to collapse [5].

Fever can also be described using the previously described mechanisms. Fever is characterized by a higher set point value for the core temperature forvarious reasons, e.g. a reaction to an infecting microorganism [10]. The patient is cold, the skin is pale and dry. The onset of shivering increases heat production and the core temperature [3]. In addition, heat dissipation is limited by vasoconstriction of the skin blood vessels and the inhibition of sweating. The fever stops if the set point value for the core temperature is set lower, back to its normal value. The stored heat is dissipated by increasing the blood perfusion of the skin and extensive sweating [10]. Fever can also be triggered by pyrogenic drugs acting on the hypothalamus [3].

The thermoregulatory system is influenced by a number of factors including pathological, physiological and behavioral factors, leading to comparable reactions in different individuals [9]. Nevertheless, the energy expenditure and body temperature can vary considerably depending on the gender, age or body composition of the organism [3].

1.4. Interaction of RF-EMF with the Human Body

The interaction of RF-EMF with the human body is based on various processes. The electromagnetic waves can be scattered, transmitted, refracted or reflected. An accurate theoretical description of these interaction mechanisms is possible using the well-known Maxwell equations [15]. The electromagnetic fields interact with the human tissue in different ways, leading to various effects (e.g. stimulation of nerves or muscles and tissue heating). Parameters such as the SAR and the current density (J) can be derived from the induced field quantities.

Tissue heating is the dominant biophysical interaction mechanism of RF-EMF fields in humans [16]. Frictional energy is deposited inside the body by different processes, including the polarization of bound charges, displacement of free charges and rotation of dipoles such as the water molecules [17]. Various other biophysical mechanisms, such as the pearl chain effect [18] and the microwave auditory phenomenon [19], are of only secondary importance. Furthermore, it is generally accepted that the energy of RF-EMF fields is too low to trigger ionization or to damage DNA [15].

Although much research has been performed in recent years, it is still possible that, due to the complexity of the topic and the lack of knowledge, some of the interaction mechanisms have yet to be discovered [17].

It is of great scientific interest to understand the known interaction mechanisms fully, especially the tissue heating, and to derive reliable models from these findings. These models can be used for risk assessments and as a basis for limiting the RF-EMF exposure [20].

The RF-EMF energy absorbed is influenced by a variety of parameters. Field properties such as the wavelength, frequency and field orientation affect the energy absorbed [21]. Furthermore, the exposure is also a function of the human geometry (e.g. children/adult, slim/fat etc.) and the tissue parameters.

Nielsen et al. [22] have shown that the tissue heating caused by RF-EMF fields is equivalent to the heating caused by any other source (e.g. physical activity). Therefore, the same thermoregulatory mechanisms, such as an increased blood flow, sweating etc., can be applied in a mathematical model to compute the temperature elevation induced. However, there are also differences in the temperature perception and elevation process. Normally thermoregulation is controlled by the thermo receptors in the skin [23]. As a result of the possible high penetration of RF-EMF fields,

energy might be deposited deep inside the human body, whereby no stimulation of these receptors occurs. This could lead to a delay in thermoperception, increasing the potential risk of RF-EMF energy absorption [20].

Biological effects are observed if the temperature increases by more than 1°C in tissue [20]. A disruption of trained tasks in primates has been investigated for temperature elevations beyond this value [20]. Shellock et al. [24] have shown that a SAR of at least 4 W/kg is needed to induce such a temperature elevation. The current radio frequency exposure limits were derived on the basis of this relationship [20]. Their central goal is to protect humans from temperature-induced adverse health effects for the frequency range 100kHZ- 300GHz [20].

The current RF-EMF exposure guidelines [20] restrict only the SAR as an indirect measure of the induced temperature elevation because of the problems in measuring and/or computing the temperature elevation in the human body. Thereby many effects influencing tissue heating are neglected: for example, the diffusion of heat in adjacent but not directly exposed tissue or the heat exchange with the environment.

However, the implementation of powerful thermal models, such as the one presented within this work, may help to strengthen the role of temperature modeling in future RF-EMF exposure guidelines.

1.5. Radio Frequency Exposure Limits

In 1998 the International Commission of Non-Ionizing Radiation Protection (ICNIRP) published a guideline with the title “Guidelines for limiting exposure to time-varying electric, magnetic, and electromagnetic fields (up to 300 GHz)” [20]. The purpose of the guideline is to protect humans from known adverse health effects caused by electric, magnetic and electromagnetic fields. Since then many studies have investigated the potential health risk of these fields. However, no adverse health effects were observed below the basic restrictions and consequently the ICNIRP reconfirmed their basic restrictions in 2009 for the frequency range 100 kHz – 300 GHz [17].

The overall strategy of the ICNIRP guidelines is to identify the biologically relevant mechanisms and to link them to easily measurable external quantities. Consequently, basic restrictions were defined to limit the biologically effective quantity and, furthermore, reference levels are used to limit the external field quantities. The correlation between these quantities was established with laboratory experiments and numerical simulations for worst case scenarios [17]. Through this approach, compliance with the reference levels ensures compliance with the far more difficult measurable or computable basic restrictions. Conversely, a violation of the reference levels does not necessarily lead to a violation of the basic restriction. However, the compliance with the basic restrictions has to be demonstrated for these cases.

The dominant biological effect for electromagnetic fields above 100 kHz is the absorption of energy and the temperature elevation induced thereby. Several parameters, such as the frequency, polarization and intensity of the field, strongly influence absorption. Furthermore, the distance between electromagnetic sources and humans, as well as the geometry of the exposed individual (child, pregnant, slim, fat, etc.), influences the energy absorbed.

A temperature elevation in the range of 1-2 °C may lead to adverse health effects [25]. Due to the difficulties associated with temperature measurements in the human body, several studies were performed to link the temperature elevation to the SAR [24] [26]. The investigations revealed that a whole-body SAR (SAR_{WB}) of at least 4 W/kg is needed to induce a body core temperature elevation of 1°C at room temperature. More recent studies have confirmed these findings [27] [14].

On the basis of these findings it is assumed that a SAR_{WB} of 0.4 W/kg is an adequate limit for occupational exposure. The pronounced safety margin takes into account

ambient parameters such as temperature, humidity etc. To avoid hazardous local hotspots the localized SAR averaged over 10 g contiguous tissues (SAR_{10g}) is also limited (10 W/kg in the head and trunk, 20 W/kg in the limbs). Compared to small anatomical structures this mass might seem rather big. However, from a thermophysiological point of view, arbitrary temperature gradients within the human body are not possible. A local hotspot would lead to immediate heat exchange, for example by an increased blood flow. Moreover, the exposure time is of crucial importance and, therefore all SAR are to be averaged over any 6 minute period.

An additional safety margin of 5 is used to restrict the exposure of the general public so that the SAR_{WB} is 0.08 W/kg and the SAR_{10g} in the head/trunk 2 W/kg and 4 W/kg in the limbs. This should take into account a possible lower tolerance of the thermoregulatory system in children, the elderly or people under the influence of drugs. In an additional statement, the ICNIRP clarified that the safety factor should not be misinterpreted in a way that might compromise the safety of the exposed people [17]. Its purpose is to compensate for the lack of knowledge and uncertainties. Consequently, the ICNIRP changed the term safety factor to reduction factor [17]. Furthermore, it was clarified that the magnitude of the reduction factor is basically derived from the scientific evidence. In the case of a good understanding of the correlation between exposure and adverse outcome, a small reduction factor might be applicable.

The reference values for the electric and magnetic field values were derived from measurements and simulations. It is well known that the coupling of electromagnetic fields and the human body is best between 10 MHz and a few hundred MHz and consequently the reference values are lowest in this region. The reference values for the electric field strength (E) and the magnetic field strength (H) are linked by the impedance of free space E/H=377 OHM. A reduction factor of $\sqrt{5}$ is applied to derive the reference levels for the general public.

The ICNIRP points out that compliance with its guidelines does not exclude a potential malfunction or hazardous heating of implants (e.g. pacemakers, metallic prostheses). Furthermore, it might be necessary to violate the guidelines for diagnostic or therapeutic reasons (e.g. medical diathermy, magnetic resonance imaging). Nevertheless, the health of the patient and medical staff has to be ensured and therefore a variety of additional standards have been defined at the European level (see for example [28] [29] [30] [31]).

2. Methods

2.1. Thermal Modeling

Pennes [32] developed the first thermal model describing the thermal energy balance for blood perfused tissue. The model was originally developed to compute the heat transfer in the human forearm based on local thermal energy production through metabolic processes and heat transfer by the volume flow of blood [33].
All thermal tissue parameters, including the blood perfusion rate, the metabolic rate and the conductivity, are assumed to be time and temperature independent. These simplifications led to a widespread use of the equation (e.g. [34] [35]).
The original model has been modified and extended in the past by several authors, which led to a more general form, not restricted to the human forearm but applicable to the whole human body [36] [37]. The model is applicable for tissue temperatures in the physiological range, including temperature elevations of up to 50°C for example during thermal therapies such as medical diathermy [37].
Although modified, the equation is still commonly known as the Pennes equation or, alternatively, the bio-heat transfer (BHT) equation.
The generalized model is defined by the following equation:

$$\rho(\boldsymbol{r})C(\boldsymbol{r})\frac{\partial T(\boldsymbol{r},t)}{\partial t} = \nabla\big(K(\boldsymbol{r})\nabla T(\boldsymbol{r},\mathrm{t})\big) + A(\boldsymbol{r}) - B(\boldsymbol{r})(T(\boldsymbol{r},t) - T_B) + \mathrm{Q}_{EXT} \qquad 2.1$$

The mass density is defined by ρ (kg/m³), C (kJ/(kg°C)) describes the specific heat capacity, K ((W/(m°C)) the thermal conductivity, T (°C) the temperature of tissue, A (W/m³) the metabolic rate, B (W/(m³°C)) the blood flow coefficient, T_B (°C) the blood temperature and finally Q_{EXT} (W) represents a potential external heat source.
The equation describes the variation of the temperature at a specific point per unit time multiplied by the mass density and specific heat capacity at this point (left hand side) to the thermal energy accumulated or lost at this point, expressed by the four terms on the right hand side. The first term describes the heat transfer through ther-

mal conduction of the biological tissue. The second term takes into account the heat produced by metabolic processes and the third term accounts for the contribution of the blood flow to the BHT equation. This latter term defines the heat transfer between blood and tissue as the product of the blood perfusion coefficient and the difference between the temperature of arterial blood, T_B, entering and the temperature of venous blood, T_V, leaving the capillary bed [32]. Therefore, the heat transfer from blood to tissue Q_{BT} (W) should be written as:

$$Q_{BT} = -B(\boldsymbol{r}, t)\big(T_V(\boldsymbol{r}, t) - T_B(\boldsymbol{r}, t)\big) \qquad 2.2$$

The Pennes model assumes a thermal equilibrium between venous blood and tissue temperature [37]. Furthermore, it is assumed that the arterial blood temperature is constant in each capillary throughout the body, fixed at a temperature equivalent to the core temperature of 37°C. Similarly, the blood perfusion term is kept constant. With these assumptions, equation 2.2 simplifies to the form presented in equation 2.1. A major advantage of this approach is that no or only little information on the actual vascular architecture of the human model is needed [37]. The blood flow is modeled with one parameter only, namely the blood flow coefficient.

The fourth term takes into account the thermal energy deposited by an external source, for example by an RF-EMF energy deposition expressed by $Q_{EXT} = \rho(\mathbf{r})\mathrm{SAR}(\mathbf{r})$.

In addition to the BHT equation, an appropriate boundary equation on the tissue-air interface has to be defined [27] [14]. This equation is applied both at the skin-air boundary and the respiratory tract-internal air boundary (in the latter case without the heat loss through sweating, SW):

$$-K(\boldsymbol{r})\frac{\partial T_s(\boldsymbol{r}, t)}{\partial n} = H(\boldsymbol{r})(T_S(\boldsymbol{r}, t) - T_a) + P_{ins}(\boldsymbol{r})/S + SW(\boldsymbol{r}, T_S(\boldsymbol{r}, t)) \qquad 2.3$$

H (W/(m²°C)) describes the heat transfer coefficient, T_a the ambient temperature, P_{ins} (W) the heat loss through evaporation, S is the area of the boundary surface (m²) and SW (W/m²) the heat loss due to sweating. Pennes [32] considered only the heat loss through convection, radiation and conduction summarized by the heat transfer coeffi-

cient. The second and third terms of the boundary equation are not considered in the original form of the BHT equation and were added in this work.

The Pennes equation neglects thermoregulatory mechanisms, such as vasodilatation and sweating, which try to keep the core temperature close to 37°C. Normally these mechanisms are activated if the temperatures in tissues containing thermal sensors, such as the skin and the hypothalamus, are elevated above known set point values [37].

To overcome this limitation, mathematical models were introduced for some of the terms in equation 2.2 and 2.3 for the thermoregulatory model developed in this work.

A mathematical description of the additional thermal models is added to the following subchapters.

2.1.1. Mathematical representation of thermoregulatory mechanisms

2.1.1.1. Variation of the blood flow coefficient as a function of the temperature elevation

The elevation of the blood flow perfusion by vasodilatation is one of the dominant thermoregulatory reactions of the human body [38]. Stolwijk [11] first introduced an empirical mathematical model describing the local blood flow coefficient in the skin, based on measurements of the peripheral vasodilatation. This model was further improved by Spiegel [38] and Lee [39] and is defined by the following equation:

$$B\big(\boldsymbol{r}, T(\boldsymbol{r},t)\big) = \big(B\big(\boldsymbol{r}, T(\boldsymbol{r},0)\big) + F_{HB}\Delta T_H(\mathrm{t}) + F_{SB}\Delta T_S(t)\big)2^{\frac{T(\boldsymbol{r},t)-T_0(\boldsymbol{r},0)}{\mathrm{a}}} \qquad 2.4$$

The elevation of the blood flow coefficient in the skin is controlled by several feedback mechanisms. One of them is the local skin temperature elevation, accounted for by the exponential term. The local blood flow coefficient doubles for every a= 6°C increase of the local skin temperature.

This is not the only feedback mechanism controlling the local blood flow coefficient in the skin. It is well known that humans possess thermo sensors in the skin as well as in the hypothalamic area [5] [3]. These sensors steer the dissipation of heat by the

dilation of the blood vessels in the skin. The blood flow coefficient is altered if the body core temperature increases (controlled by the thermo sensors in the hypothalamus). Furthermore, the peripheral blood flow coefficient is also controlled by the average skin temperature. This latter mechanism ensures that the body can react fast enough to temperature changes in the environment, e.g. entering a warm room, long before the body core temperature elevates substantially.

The contribution of these mechanisms is proportional to the average temperature in the hypothalamus ($\Delta T_H(t)=T_H(t) - T_H(0)$) and the skin ($\Delta T_S(t)$), defined by the following equation:

$$\Delta T_S(\mathrm{t}) = \frac{\int_S (T(\boldsymbol{r},t) - \mathrm{T}(\boldsymbol{r},0))dS}{S} \qquad 2.5$$

with S (m^2) being the body skin surface.

The constants F_{HB} (17.5 kW/(m^3°C)) and F_{SB} (1.1 kW/(m^3°C)) are empirical values [27] [14], giving different weights to both feedback mechanisms, leading to an almost 16 times higher importance of the hypothalamic temperature elevation over the average temperature elevation in the skin [27].

It has been shown with measurements that the elevation of the blood flow coefficient in the skin was not enough to accurately compute the temperature elevation in the body with a theoretical thermal model [40] [41]. Ghatterjee et al. [42] introduced an additional empirical model for the blood flow coefficient of the internal tissues. The blood flow coefficient for all internal tissues is solely controlled by the local tissue temperature. For local tissue temperatures less than 39°C, the blood flow coefficient remains equal to the basal value. After increasing linearly with the temperature, the blood flow coefficient reaches a plateau at 44°C and saturates at five times the basal value for even higher local temperatures [43]. The following set of equations is used for the implementation of this thermal mechanism:

$$B\big(\boldsymbol{r},T(\boldsymbol{r},t)\big) = B\big(\boldsymbol{r},T(\boldsymbol{r},0)\big) \qquad T(\boldsymbol{r},t)\leq 39℃ \qquad 2.6$$

$$B\big(\boldsymbol{r},T(\boldsymbol{r},t)\big) = B\big(\boldsymbol{r},T(\boldsymbol{r},0)\big) \times \big(1 + 0.8(T(\boldsymbol{r},0) - 39)\big) \qquad 39℃ < T(\boldsymbol{r},t) < 44℃ \qquad 2.7$$

$$B\big(\boldsymbol{r},T(\boldsymbol{r},t)\big) = 5 \times B\big(\boldsymbol{r},T(\boldsymbol{r},0)\big) \qquad \mathrm{T}(\boldsymbol{r},t)\leq 44℃ \qquad 2.8$$

The validity of this approach has been shown by various studies (e.g. [27] [14] [43]).

2.1.1.2. Variation of the metabolic rate as a function of the temperature elevation

The thermal energy produced by metabolic processes increases with the local temperature [3]. Hoque et al. [44] introduced the following mathematical equation describing this process:

$$A\big(\boldsymbol{r}, T(\boldsymbol{r},t)\big) = A\big(\boldsymbol{r}, T(\boldsymbol{r},0)\big)1.1^{\frac{(T(\boldsymbol{r},t)-T(\boldsymbol{r},0))}{a}} \qquad 2.9$$

A(r,T(r,0)) (W/m³) is the basal metabolic rate at rest and a=1°C the empirical normalization factor for the local temperature elevation. The metabolic rate increases exponentially with regard to the local temperature elevation. Figure 2-1 demonstrates that even a pronounced local temperature elevation leads to a small increase of the metabolic rate, in the range of 1.5 % or less.

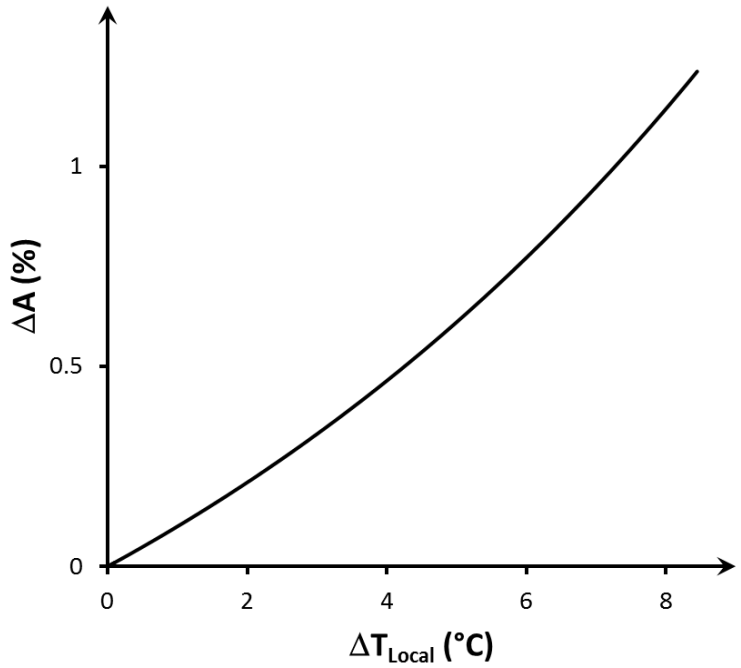

Figure 2-1: Relative increase of the local metabolic rate (ΔA) in percent of the basal metabolic rate and as function of the local tissue temperature elevation (ΔT_{Local}).

The validity of this mathematical model has been shown by Bernardi et al. [27].

2.1.1.3. Blood temperature variation as a function of the acquired thermal energy

From the definition of the BHT equation it is obvious that blood acts as a heat carrier, by taking the heat from body parts with a higher temperature in the body core to the surface of the body, where the heat is delivered to the skin layer due to its lower temperature. There the heat is dissipated by the heat loss through passive mechanisms like radiation, conduction and convection and active mechanisms like evaporation and sweating [5] [27]. The latter thermoregulatory mechanism is further amplified by the previously described adaption of the blood flow coefficient.

This process helps to maintain the body core temperature close to 37°C, even for changing environmental conditions.

A simplification of the BHT equation is the assumption that the net heat exchange between tissue and blood is zero, which results in a constant blood temperature, even if a severe external heat load is applied [45].

Bernardi et al. [27] first introduced a mathematical model to overcome this limitation. The model was further improved by Fujiwara et al. [46] and is defined by the following equation:

$$T_B(t) = T_{B0} + \int_t \frac{Q_{BN}(\mathrm{t})}{C_B \rho_B V_B} \mathrm{dt} \qquad 2.10$$

T_{B0} (°C) is the blood temperature at the steady state, $Q_{BN}(t)$ (W) is the net thermal energy acquisition of blood from body tissues, C_B (3.9 kJ/(kg°C)) the specific heat capacity of blood, ρ_B (1060 kg/m³) the density of blood and V_B (m³) the blood volume which changes for each human model as a function of age and size (see Table 5-1,Table 6-1,Table 7-1 and Table 8-2) [47].

The net thermal energy acquisition of blood can further be written as [46] [14]:

$$Q_B(t) = \int_V B(\boldsymbol{r}, t)\big(T(\boldsymbol{r}, t) - T_B(t)\big) \qquad 2.11$$

$$Q_{BN}(t) = Q_B(t) - Q_B(0) \qquad 2.12$$

The latter equation was introduced to compensate for the energy acquisition of blood at steady state [14]. It could be shown that equation 2.11 is not zero even at steady state and this is mainly attributed to numerical inaccuracies [45]. A non-physiological blood temperature elevation would occur if this effect were not compensated for.
Equation 2.10 can be rewritten as a first-order ordinary differential equation, which leads to the following form:

$$\frac{dT_B}{dt} = \frac{Q_B(t)}{C_B \rho_B V_B} - \frac{Q_B(0)}{C_B \rho_B V_B} \qquad 2.13$$

The time derivative on the left side of the equation can be discretized by using finite differences. After some rearrangements the following equation is obtained for the computation of the blood temperature:

$$T_B^{P+1} = \frac{\frac{T_B^P}{\Delta t} + \frac{B^P T(\boldsymbol{r})^P V_{BODY}}{C_B \rho_B V_B} + \frac{Q_B(0)}{C_B \rho_B V_B}}{\frac{1}{\Delta t} + \frac{B^P V_{BODY}}{C_B \rho_B V_B}} \qquad 2.14$$

V_{Body} (m^3) is the volume of the human model used and Δt the time interval used for solving the equation. The basal values of the parameters (linked to time step P) are used to compute the values for the next time step (P+1). The newly computed blood temperature (T_B^{P+1}) is used as an input for the BHT equation. These steps are repeated for the duration of the whole simulation process so that the continuous adaptation of the blood temperature is assured.
Either an implicit or explicit scheme of the equation can be used [37]. In this work only the presented explicit, although more time consuming, form was used since the implicit form might lead to a non-physiological oscillation of the blood temperature if too big a time step (Δt) were to be used [37].

2.1.1.4. Heat balance at steady state

As with any other thermal system, heat transfer will occur within the human body and to its environment until a steady state temperature is established [37].

To obtain a stable equilibrium, the thermal energy produced in one system, in this case by metabolic processes in the human body, has to be in balance with the heat taken up or given to another system, in this case the environment. Therefore, passive mechanisms such as the convection, conduction and radiation of heat as well as the heat dissipation by the active evaporation of water have to be considered at the tissue-air interface. This includes the skin surface as well as the surface of the respiratory tract.

These assumptions lead to the following equation if no external heat stress is applied:

$$\int_V A(\boldsymbol{r})dv = \int_S p_{ins}dS + \int_S (h_{conv}(\boldsymbol{r}) + h_{rad}(\boldsymbol{r}) + h_{cond}(\boldsymbol{r}))(T(\boldsymbol{r},t) - T_a)dS \qquad 2.15$$

The equation equates the whole body metabolic rate, described by the integral on the right hand side, to the heat lost by the active evaporation of water described by the rate of evaporation (p_{ins} in W/m²) integrated over the related surface and the heat dissipated by the passive mechanisms including the convection (h_{conv} in W/(m²°C)), the radiation (h_{rad} in W/(m²°C)) and conduction (h_{cond} in W/(m²°C)). The contribution of the latter mechanisms can be expressed by the product of their sum multiplied by the temperature gradient at the tissue-air interface (T(r,t) is the tissue temperature in °C, T_a is the ambient air temperature in °C), integrated over the related surface.

The model-specific values can be derived on the basis of this relationship. Values for the whole body metabolic rate, which varies with age and gender, were taken from the ICRP [48]. The heat loss due to the evaporation of water, also known as insensible loss of water, in the whole body is defined by the following equation:

$$P_{ins} = \int_S p_{ins}dS \qquad 2.16$$

The values used for all models, related to their age, size and gender, were taken from an experimental study performed by Margaret et. al [49]. Seventy percent of the

whole body insensible water loss occurs at the skin (P_{ext}), while the remaining thirty percent is lost from the respiratory tract due to breathing (P_{int}) [13].
The passive mechanisms can be summarized to a generalized heat transfer coefficient H (W/(m²°C)):

$$H(\boldsymbol{r}) = \int_S (h_{conv}(\boldsymbol{r}) + h_{rad}(\boldsymbol{r}) + h_{cond}(\boldsymbol{r}))(T(\boldsymbol{r},t) - T_a)dS \qquad 2.17$$

Eighty percent of the heat loss by these passive mechanisms occurs at the skin surface (H_{ext}) while the remaining twenty percent is lost through the respiratory tract (H_{int}) [50].
The values derived for all the human models and ambient temperatures used are listed in Table 4-2, Table 5-1,Table 6-1,Table 7-1 and Table 8-2.

2.1.1.5. Sweating as a function of the temperature elevation

The mathematical consideration of the heat lost through sweating is of essential importance to the suitability of the thermoregulatory model [37]. The mechanisms described in the last subchapter are not able to dissipate the heat sufficiently if an external heat stress, e.g. RF-EMF energy, is applied [43].
In this work an empirical mathematical model first introduced by Stolwwijk [11] and further improved by Bernardi et al. [27] is used to account for this physiological mechanism. The model used tries to make a best-fit to experimental data and various environmental conditions [38] and is defined by the following equation:

$$SW(\boldsymbol{r}, T_S(\boldsymbol{r},t)) = (F_{HS}\Delta T_H(\mathrm{t}) + F_{SS}\Delta T_S(t))2^{\frac{T(\boldsymbol{r},t)-T_0(\boldsymbol{r},0)}{\mathrm{a}}} \qquad 2.18$$

This model is very similar to the equation describing the blood flow coefficient in the skin. The same three feedback mechanisms are used to account for the heat loss due to sweating. The local heat loss due to sweating doubles if the local temperature increases by a=10°C. Once again, the average hypothalamic temperature elevation ($\Delta T_H(t)$) and the average skin temperature elevation ($\Delta T_S(t)$) form the other feedback signals. The constants F_{HS} (140 W/(m³°C)) and F_{SS} (13 W/(m³°C)) are empirical values [27] [14] which give different weights to the two feedback mechanisms, leading to

an almost 11 times higher importance to the average hypothalamic temperature elevation compared to the average skin temperature.

2.2. Thermal Field Computation

The computation of the temperature elevation caused by RF-EMF energy absorption is a two-step process. First, the SAR in the human body is computed (see chapter 2.3) and then the SAR is used in the BHT equation as an additional heat source. Additional software had to be implemented to compute the temperature elevation since the simulation software used (CST Studio Suite 2011®) does not support any of the previously described thermoregulatory mechanisms nor the improved heat exchange at the tissue/air interface.

However, a Dynamic Link Library (DLL) is provided which allows access to and manipulation of CST directly from Matlab®. Several routines were implemented in Matlab® including a graphical user interface. A detailed overview, including the past and returned values, is included in the Appendix (see A.1).

Figure 2-2 shows a flowchart of the whole process. At the beginning the electromagnetic field distribution is computed within CST. Then the actual Matlab® software can be started with these results as input. Next, a graphical user interface (GUI) opens where input parameters such as the human model used, blood temperature, simulation time and others can be defined. The chosen project is then initialized in CST through Matlab® and all the simulation parameters are set. Information regarding the discretization of the simulation domain is now gathered, including the dimensions of all mesh cells, and the coordinates of each voxel are loaded. This information was previously stored to tissue specific files generated in a pre-processing step. Finally, the boundary voxels on the tissue/air interface are determined. As a result of the coarse surface of the voxel model, not only the skin adjoins air (see Figure 2-3) and so the heat loss through sweating, convection, radiation, conduction and insensible water loss has also to be considered in these voxels in order to get reliable results.

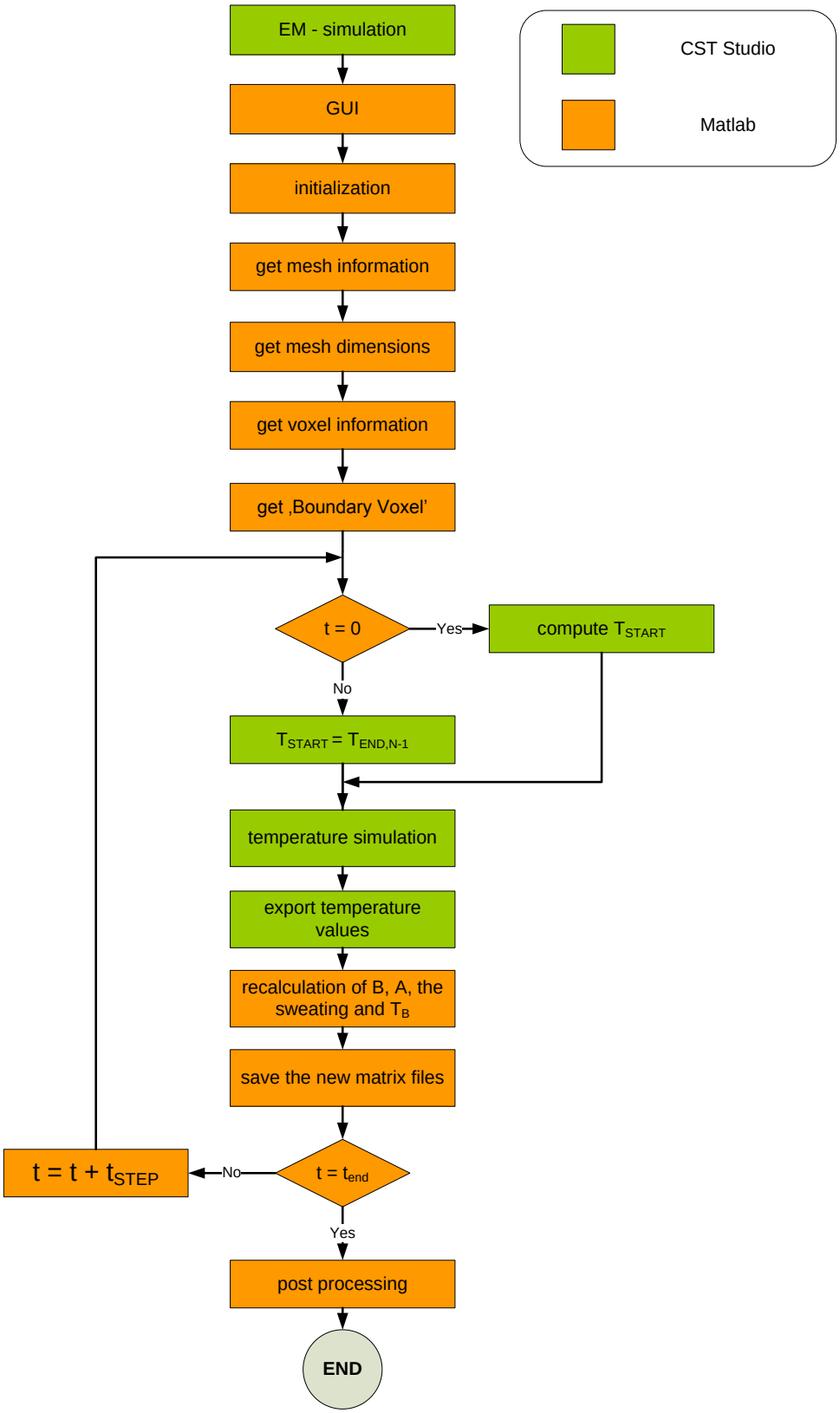

Figure 2-2: Flowchart describing the process-chain for the electromagnetic and thermoregulatory simulations.

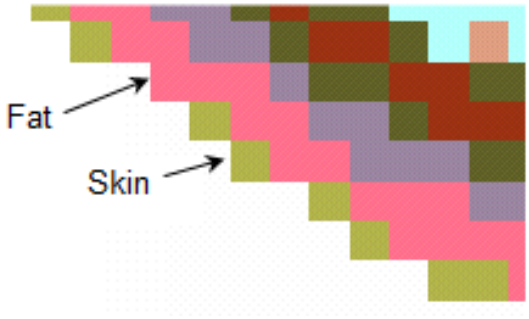

Figure 2-3: Small detail of a voxel model showing different tissues at the tissue/air boundary.

The actual thermal modeling starts after these pre-processing steps. In the first run the start temperature distribution at steady state with no RF-EMF exposure has to be computed. Next, the temperature elevation caused by the simulated RF-EMF energy absorption is computed for the chosen simulation time step. Then a VB macro exports the temperature of each voxel and the coordinates of the voxel center to tissue specific files. On the basis of the increased temperature and the thermoregulatory mechanisms (see chapter 2.1), parameters including the flow coefficient, metabolic rate, blood temperature and sweating are recomputed for each voxel. The newly computed blood temperature is a single value that can simply be passed to CST. The blood flow coefficient and the metabolic rate must be stored to their corresponding three dimensional material matrix files. The voxel values therefore have to be mapped to the underlying mesh (see Figure 2-4).

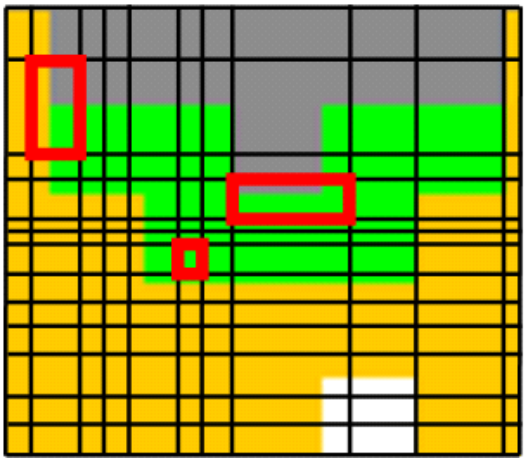

Figure 2-4: Small detail of a voxel model showing different tissues and the underlying mesh (black lines).

The red highlighted areas show that some mesh cells consist only of one tissue type, whereas others contain two or more tissue types. For these cells an averaged value, proportional to the volume fraction of each tissue, is stored to the material file.

The heat loss due to sweating at the surface of the model is converted to a volumetric heat loss and subtracted from the metabolic heat production in these voxels and saved to the material file.

These steps are carried out continuously until the predefined simulation time is reached.

In a post processing step all simulation results, including a temperature distribution for each time-step and the blood temperature elevation as a function of time, is saved to the project folder.

2.3. Electromagnetic Field Computation [51]

Numerical methods are a reliable and essential tool in the field of electromagnetic dosimetry. Normally it is not possible to measure electromagnetic fields in a living biological organism. This makes numerical simulation the sole noninvasive method to get a reliable field distribution within a human body. Electromagnetic exposure scenarios including numerical human models cannot be solved with known analytical methods. Therefore, over the last decades a variety of different numerical approaches have been implemented to solve Maxwell's equations for arbitrary configurations. Commonly used methods include the Finite Difference Method (FD), the Finite Element Method (FEM), the Boundary Element Method (BEM) and the Finite Integration Technique (FIT) [2].
In this work the commercial software package CST Studio Suite 2011® (CST) [1] has been used for the electromagnetic field computations. The program and the solvers are based on the FIT.

2.3.1. Finite Integration Technique FIT

The FIT was first introduced by T. Weiland [52] [53] and has since been an important basis for a variety of numerical algorithms to solve Maxwell's equations. A major advantage of this method is its universal discretization scheme, allowing the investigation of electromagnetic exposure scenarios ranging from static field problems to high frequency problems both in time and frequency domains. In contrast to the vast majority of numerical methods, FIT discretizes the integral form of Maxwell’s equations and not their differential form (see equations 2.19 through 2.22).

$$\oint_{\partial A} \vec{E} * d\vec{s} = \int_{A} \frac{\partial \vec{B}}{\partial t} * d\vec{A} \qquad \text{Faraday's law of induction} \qquad 2.19$$

$$\oint_{\partial A} \vec{H} * d\vec{s} = \int_{A} \left(\frac{\partial \vec{D}}{\partial t} + \vec{J} \right) * d\vec{A} \qquad Ampere's\ circuital\ law \qquad 2.20$$

$$\oint_{\partial A} \vec{D} * d\vec{A} = \int_{V} \rho * dV \qquad Gauss's\ law \qquad 2.21$$

$$\oint_{\partial A} \vec{B} * d\vec{A} = 0 \qquad Gauss's\ law\ for\ magnetism \qquad 2.22$$

To be able to solve these equations in combination with an arbitrary exposure scenario, it is necessary to define a finite calculation domain. This domain is split up into a, preferably, high number of small elements called grid cells as shown in Figure 2-5. The software offers the possibility to use orthogonal hexahedral grids, as well as topologically irregular grids (subgrids) and tetrahedral grids. The following explanation of the FIT method is based on an orthogonal hexahedral grid.

The spatial discretization of Maxwell's equation is applied to two orthogonally aligned mesh grids. Figure 2-5 shows that the electric grid voltage **e** is allocated on the edges of the primary grid **G** and the magnetic flux **b** on the corresponding faces. The magnetic voltages, **h**, and the dielectric flux **d** through the corresponding face are defined on the edges of the second grid $\widetilde{\mathbf{G}}$ [54].

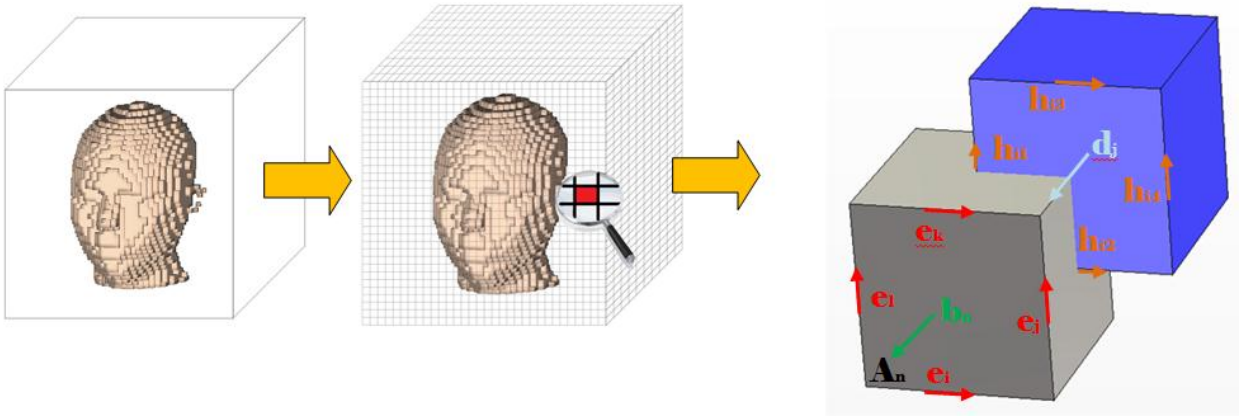

Figure 2-5: Connection between the calculation domain, the grid and a single grid cell.

Maxwell's equations are defined either on each edge or face of both grids. The integral on the left side of Faraday's law can be written as the sum of the four voltages on the edges of the grid cell (see Figure 2-6). This operation introduces no numerical uncertainty. The right hand side of the equation is defined by the time derivative of the enclosed magnetic flux. Next, this procedure is applied to each grid cell, which defines the matrix formulation for the whole calculation domain.

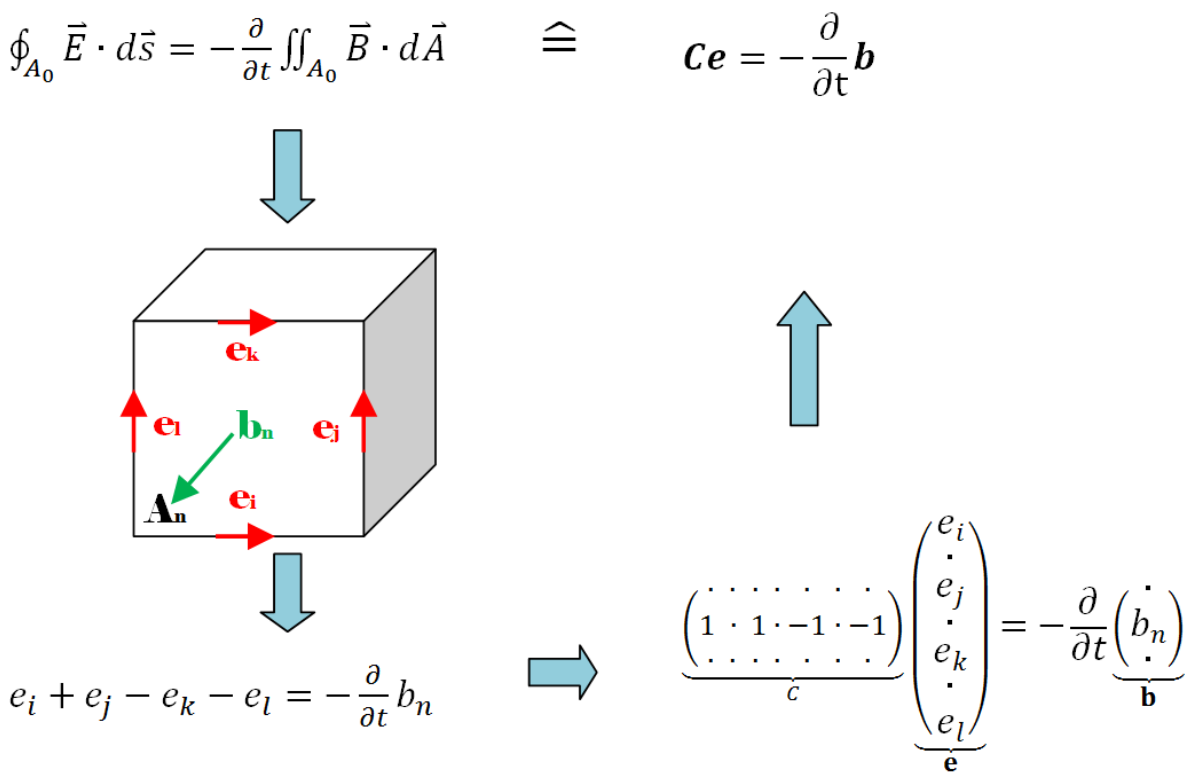

Figure 2-6: Relation between Faraday's law and the corresponding Maxwell Grid Equation.

Figure 2-6 shows that the matrix **C** is the discrete counterpart of the analytical curl operator in Faraday's law. With the same assumptions, a matrix $\tilde{\mathbf{C}}$ for Ampere's law is defined on the secondary grid. For the divergence equations the same discretization scheme is used, leading to the divergence operator **S** for the primary and $\tilde{\mathbf{S}}$ for the secondary grid. These assumptions lead to the discretized form of Maxwell's Grid Equations (MGE).

$$\mathbf{Ce} = -\frac{\mathbf{d}}{\mathbf{dt}}\mathbf{b} \qquad \text{Faraday's law of induction} \qquad 2.23$$

$$\tilde{\mathbf{C}}\mathbf{h} = -\frac{\mathbf{d}}{\mathbf{dt}}\mathbf{d} + \mathbf{j} \qquad Ampere's\ circuital\ law \qquad 2.24$$

$$\tilde{\mathbf{S}}\mathbf{d} = \mathbf{q} \qquad Gauss's\ law \qquad 2.25$$

$$\mathbf{Sb} = 0 \qquad Gauss's\ law\ for\ magnetism \qquad 2.26$$

The matrix operators contain only the elements ‘0’, ‘1’ and ‘-1’ and, therefore, solely topological information. None of the mathematical transformations presented, from the analytical to the discretized form, introduces a numerical error.

To solve an electromagnetic field problem for the calculation domain the material equations have to be defined as well. These equations define the required relation between voltage and flux. The material matrix M introduces a numerical inaccuracy which is a function of the averaged material parameters or the resolution of the grid. Again, the analytical equations can easily be transformed to their numerical counter-part, leading to the conductivity $\mathbf{M}_{\boldsymbol{\sigma}}$, permeability $\mathbf{M}_{\boldsymbol{\mu}}$ and permittivity $\mathbf{M}_{\boldsymbol{\varepsilon}}$ matrices [55].

$$\vec{D} = \varepsilon\vec{E} \qquad \boldsymbol{d} = \mathbf{M}_{\boldsymbol{\varepsilon}}\boldsymbol{e}$$

$$\vec{B} = \mu\vec{H} \qquad \boldsymbol{b} = \boldsymbol{M}_{\boldsymbol{\mu}}\boldsymbol{h}$$

$$\vec{J} = \sigma\vec{E} + \vec{J}_s \qquad \boldsymbol{j} = \boldsymbol{M}_{\boldsymbol{\sigma}}\boldsymbol{e} + \boldsymbol{j}_{\boldsymbol{s}}$$

Once all equations are defined the electromagnetic problem can be solved with a suitable solver, covering the range from DC to high frequencies.

2.3.2. Transient Solver

The transient solver is able to compute the electromagnetic behavior of a problem setup over a broad frequency range in one simulation run. Furthermore, the solver is

the method of choice for exposure scenarios with large dimensions and/or open boundaries. The energy and field values are computed for the simulation duration at discrete locations and at discrete time samples. Therefore, the previously defined MGE equations, in combination with a discretized time grid, are used. The substitution of the time derivate by central differences and their combination with the material equations leads to the following set of equations.

$$\boldsymbol{e}^{\boldsymbol{n+\frac{1}{2}}} = \boldsymbol{e}^{\boldsymbol{n-\frac{1}{2}}} + \Delta t \boldsymbol{M}_{\boldsymbol{\varepsilon}}^{\boldsymbol{-1}}\left[\widetilde{\boldsymbol{C}}\boldsymbol{M}_{\boldsymbol{\mu}}^{\boldsymbol{-1}}\boldsymbol{b}^{\boldsymbol{n}} + \boldsymbol{j}_{\boldsymbol{s}}^{\boldsymbol{n}}\right] \qquad 2.27$$

$$\boldsymbol{b}^{\boldsymbol{n+1}} = \boldsymbol{b}^{\boldsymbol{n}} + \Delta t \boldsymbol{C}\boldsymbol{e}^{\boldsymbol{n+\frac{1}{2}}} \qquad 2.28$$

These equations show that the unknowns, namely the electric voltage **e** as well as the magnetic flux **b,** are located alternatively in time. It is exactly this attribute which used in the well-known leap-frog scheme as shown in Figure 2-7.

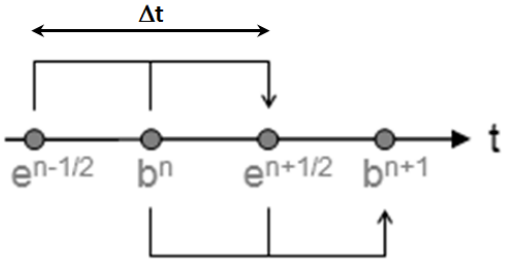

Figure 2-7: Iterative process to compute the electrical voltage and the magnetic flux with the leap frog scheme.

The scheme reveals that the actual field component is a function of the field values of the previous time step Δt. The stability limit for this method and, thereby, for the Δt is defined by the Courant-Friedrichs-Levy (CFL) criterion.

$$\Delta t \leq \frac{\sqrt{\varepsilon\mu}}{\sqrt{\left(\frac{1}{\Delta x}\right)^2 + \left(\frac{1}{\Delta y}\right)^2 + \left(\frac{1}{\Delta z}\right)^2}} \qquad 2.29$$

This equation shows that the smallest grid cell defines the upper limit of the time step. As a consequence, a high mesh resolution, even in a small subdomain of a large problem, leads to a long simulation time.

2.3.3. Generation of the Mesh

The mesh is used to transform the exposure scenario into a computer readable format. All components of the problem, including electromagnetic sources, boundary conditions and models have to be transformed. The calculation domain is therefore divided in small grid cells as shown in Figure 2-5. CST only supports the hexahedral mesh for problems including human voxel models. The software provides an expert system which automatically generates a mesh. The automatic mesh generation takes into consideration the frequency range, the dielectrically material properties and other parameters. In addition, the mesh can also be refined manually for all components in the simulation domain.

Round structures, very small structures or not orthogonally aligned structures may lose their original form when transformed to a numerical grid. Nevertheless, the body structure can be maintained with a dense mesh. The available random access memory and the need to restrict the simulation duration to a reasonable value (see 2.3.2) puts a practical limit on the density of the mesh.

Depending on the human model used, at least 21 and not more than 39 million mesh cells have been used for the simulations presented.

2.4. SAR Computation

The SAR can be computed within CST in a post processing step from the power loss distribution (PLD) and the tissue density (ρ).

$$PLD = \frac{d}{dt}\left(\frac{dW}{dV}\right) \quad \left[\frac{W}{m^3}\right] \tag{2.30}$$

$$SAR = \frac{PLD}{\rho} \quad \left[\frac{W}{kg}\right] \tag{2.31}$$

The software offers the possibility of computing the whole body SAR (SAR_{WB}) as well as the localized SAR (SAR_{10g}) averaged over a quadratic cube of 10g as defined by the IEEE [56]. Limiting the SAR over a mass of 10g should keep the temperature rise in the eye below 1°C.

The ICNIRP guidelines, however, require the SAR_{10g} to be averaged over any 10g of contiguous tissue [20]. It has been shown that the ICNIRP method is more conservative by a factor of up to 2.5 than the suggested IEEE approach [57]. The localized SAR values presented here are computed according to the ICNIRP guidelines and therefore a couple of self-written routines have been used. First, the point wise SAR is computed in CST and then a Visual Basic (VBA) macro is used to export the SAR of each voxel as well as the related coordinates and tissue density. Finally, a Matlab® routine picks the absolute maximum of each tissue. In an incremental process, the nearby voxel with the highest SAR value is added to the averaged, irregular volume. The algorithm stops when an averaging mass of 10g contiguous tissue is reached. Figure 2-8 shows an example output of the algorithm.

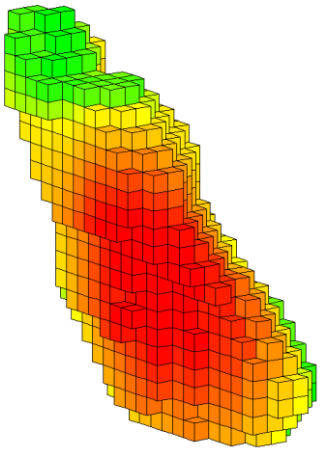

Figure 2-8: Example of a localized SAR averaged over 10g of contiguous tissue. The maximum occurs in the muscle near the left knee in a child model exposed to a plane wave at the ICNIRP reference level.

All tissues and organs are considered for the averaging process and evaluated separately. Together with the SAR_{10g} value, the position of the local maximum is provided by the algorithm. This information is required since the RF-EMF exposure regulations put different restrictions on the limits in the head/trunk and the limbs.

2.5. Human Models

The availability of high resolution and detailed numerical human models is of crucial importance for the success of numerical dosimetry. Modern models are created with medical diagnostic tools such as Magnetic Resonance Imaging (MRI) or Computer Tomography (CT) and are generally voxel based. A voxel ('volumetric pixel') is a cube of the size of a few mm^3. Each voxel is defined by its tissue type and the dielectric and thermal properties. Human models are defined by a spatial dataset in Cartesian coordinates and consist of a couple of million voxels.

Over the last decade numerous models have been developed covering different sizes, gender and ages of humans. In this work 20 of them, including pregnant and child models, have been used. A detailed overview of the model characteristics is included in the Appendix (see A.2). [58]

2.5.1. NORMAN

The model is based on a series of MRI scans covering different body parts of the same individual. The raw data was scaled, translated and rotated in a first post processing step to form one, homogenous body. In a semi-automated process the gray scaled pictures were differentiated in 37 tissues (see Figure 2-9). In some cases the differentiation was not possible due to the poor quality of the MRI scans. These areas were modeled according anatomical textbooks, e.g. the internal structure of the heart [21]. The original model does not include the hypothalamus, which is crucial for the thermal modeling (see chapter 2.1) so it was included on the basis of information from anatomical textbooks.

The standing male was normalized to a weight of 73 kg and a height of 176 cm, which corresponds to the dimensions of the 'reference man' defined by the ICRP [59]. This is where the model got its name 'normalized man' = NORMAN.

The model was segmented with a resolution of 2 mm.

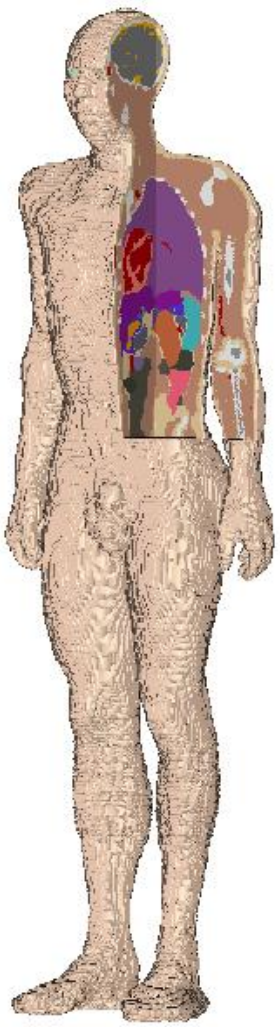

Figure 2-9: The model NORMAN with a resolution of 2x2x2 mm.

2.5.2. FEMONUM

Lazar et al. have implemented a method to generate pregnant models at different stages of pregnancy (from the 9th. to the 35th. week of gestation) and with the fetus in varying positions. The models are based on ultrasound images (US) for the first trimester and on MRI for the second and third trimesters [58]. Only the uterofetal unit (UFU) is differentiated, whereas the rest of the model is homogeneous. Up to 11 tissues were differentiated in the UFU, including lung, heart, brain, stomach, CSF and the eyes amongst others (see Table 2-3). The hypothalamus, which is crucial for the thermal modeling (see chapter 2.1), was inserted on the basis of anatomical textbooks.

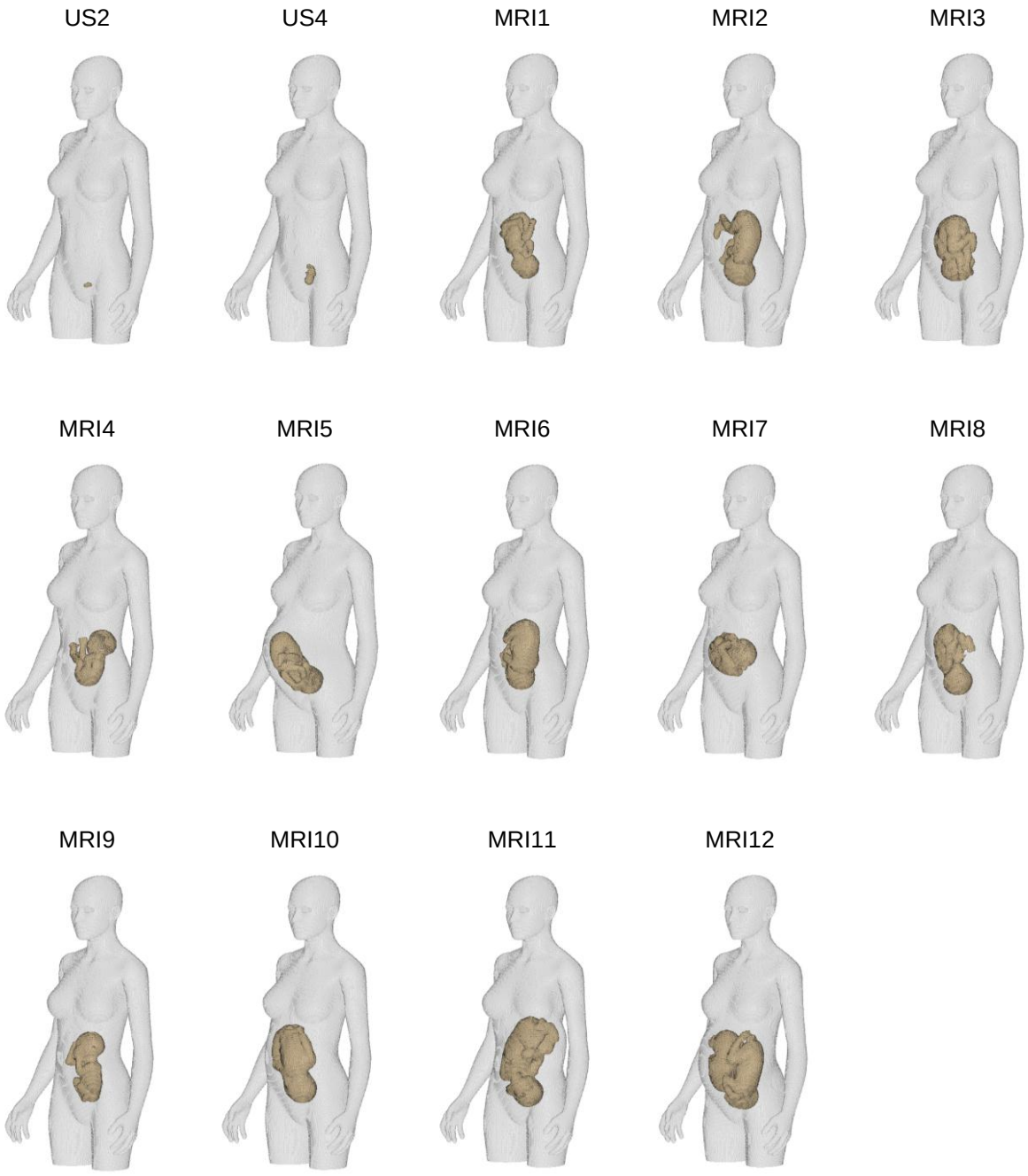

Figure 2-10: The pregnant human model FEMONUM in different stages of pregnancy and different positions of the UFU.

The two US models were the first pregnant models in the first trimester [58]. The twelve MRI models cover the most likely positions of the fetus [60] and the position of the placenta was also adjusted [61]. One of the models features a UFU with twins. The models were validated by clinical experts. Each model was segmented with a resolution of 2 mm. The format of the models provided was incompatible with the software used and had to be adapted with self-written Matlab® routines.

Table 2-1 shows the main characteristics of the pregnant models, a more detailed overview is included in the Appendix (see A.2).

Model	Stage of Pregnancy (week)	Weight of Mother (kg)	Weight of Fetus (g)	No. of tissues
US2	9	52.88	3	6
US4	13	52.91	38	6
MRI1	26	54.80	1036	13
MRI2	30	54.93	1879	13
MRI3	30	54.67	1849	13
MRI4	30	53.64	926	13
MRI5	32	59.37	2032	13
MRI6	32	54.99	1873	13
MRI7	32	55.01	1188	11
MRI8	32	54.72	1509	13
MRI9	33	54.43	1144	13
MRI10	33	55.59	2234	13
MRI11	34.5	55.68	2746	13
MRI12	34.5	58.79	1540^{Twin1} 1899^{Twin2}	22

Table 2-1: Characteristics of the 14 FEMONUM models sorted according the stage of pregnancy.

2.5.3. Child Models

The child models are provided by the IT'IS Foundation (Switzerland) [62]. The models are part of the 'Virtual Population' and are differentiated into up to 76 tissues. Three female and three male models were used for the simulations (see Figure 2-11).

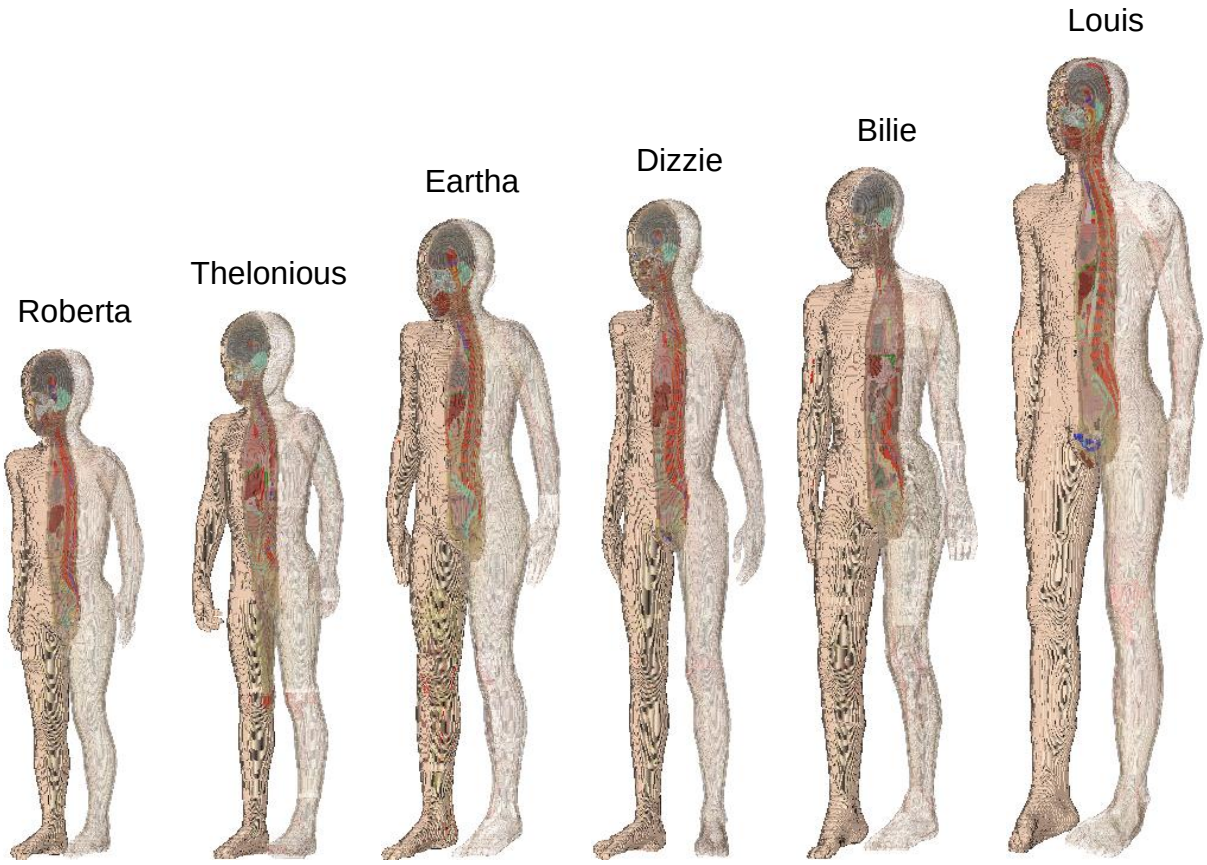

Figure 2-11: Children models featuring three female and three male models

The size and weight of the anatomically correct models is based on German averaged values and gathered from high resolution MRI scans. The tissues were differentiated semi-automatically, with the help of biologists and physicians [62]. The original data were provided in unstructured triangulated surfaces and were transformed with self-written Matlab® routines to the corresponding voxel model with a resolution of 2 mm. The main characteristics of the models are listed in Table 2-1. A more detailed overview is included in the Appendix (see A.2).

Name	Sex	Age (years)	Height (cm)	Weight (kg)	BMI (kg/m²)	No. of tissues
Louis	male	14	165	49,9	18,3	69
Billie	female	11	146	35,6	16,7	75
Dizzie	male	8	140	26,2	13,4	66
Eartha	female	8	135	30,3	16,6	75
Thelonious	male	6	117	19,5	14,2	76
Roberta	female	5	109	16	13,5	66

Table 2-2: Main characteristics of the child models, sorted according to their age.

2.6. Physical Properties of Human Tissue

2.6.1. Electrical Properties

The electrical properties of biological tissues have been measured in a number of studies over the last decades [63] [64]. This has led to a number of varying values, which, consequently, has added a large degree of uncertainty to the field of numerical dosimetry. The main reason for the differences between the studies could be the non-standardized measurement setup. Sometimes neither the origin (living or dead organisms) nor the preparation of the specimen is reported in the literature.

Gabriel et al. tried to overcome this problem in a series of publications. First they published a review of the existing literature [65] and followed this with their own measurements, with a clearly defined setup, for the missing tissues [66]. A parametric model was derived on the basis of this data to compute the electrical properties of human tissues for frequencies from 10 MHz to 100 GHz [67]. Nevertheless, the uncertainty remains quite high, ranging from ±5% up to ±15% [65]. The Institute of Applied Science of the University of Florence operates a homepage where the values for the electrical conductivity as well as for the permittivity can be downloaded, based on the parametric model[1].

To reduce the number of error sources a spreadsheet (Microsoft Excel 2010®) including some VBA macros was implemented. The spreadsheet loads the data for a specific frequency from the homepage. After linking the tissue values to the various models a simple, CST compatible, frequency and model specific tissue file is saved.

[1] http://niremf.ifac.cnr.it/tissprop/

The dielectric properties of the tissues change with age. This fact is mainly attributed to the declining water content, which primarily defines the dielectric properties, with age [66]. Measurements and simulations have been performed that account for this age dependency. These studies show that the SAR does not change systematically in children at different ages [68] [69]. Wang et al. [70] argue that the effect of the higher conductivity might be compensated by the decreased penetration depth of the electrical field due to the increased permittivity and therefore it seems justified to ignore age dependency in the children older than five years.

However, the values for the fetal tissue were adjusted for their significantly higher water content. Foster et al. introduced a model describing the electrical properties based on the water content of the tissue from 10 MHz to 100GHz [71].

$$\varepsilon' = 1.71 f^{-1.13} + \frac{\varepsilon_m - 4}{1 + \left(\frac{f}{25}\right)^2} + 4 \qquad 2.32$$

$$\sigma = 1.35 f^{0.13} \sigma_{0.1} + \frac{0.0222(\varepsilon_s^m - 4) f^2}{1 + \left(\frac{f}{25}\right)^2} \qquad 2.33$$

The units of the values have to be considered to obtain correct results. ε' is the relative permittivity, σ the conductivity in mS/cm and f the frequency in GHz. The extrapolated microwave permittivity ε_m and the conductivity at 100 MHz $\sigma_{0.1}$ are a function of the water content of the tissue and were gathered from the literature [71]. The water content of the fetus changes considerably during pregnancy and therefore the previously defined equations and parameters had to be adapted for each pregnant model. The water content of the fetal brain has to be further adjusted, since up to 15 % of it is in a bound state [71] [34]. The model described was applied to the fetus, based on data from [48] and to the fetal brain based on data from [71].
Table 2-3 gives an overview of the fetal tissues and the sources used for the electrical properties.

Tissue	Source
Amniotic Fluid	CSF, Gabriel et al. [66] [67], Hand et al. [34]
Bladder	Body fluid, Gabriel et al. [66] [67]
Brain	see text
CSF	CSF, Gabriel et al. [66] [67]
Eyes	Eyes, Gabriel et al. [66] [67]
Fetus	see text
Heart	Heart, Gabriel et al. [66] [67]
Lungs	Lungs deflated, Gabriel et al. [66] [67], Hand et al. [34]
Placenta	Muscle, Gabriel et al. [66] [67], Hand et al. [34]
Stomach	Body fluid, Gabriel et al. [66] [67]
Umbilical Cord	Muscle, Gabriel et al. [66] [67], Hand et al. [34]
Uterus/ Placenta	Uterus and Muscle, Gabriel et al. [66] [67], Hand et al. [34]

Table 2-3: Differentiated fetal tissues linked to the sources of the used electrical properties.

2.6.2. Thermal Properties

In order to compute the temperature inside the human models with the developed thermal model the following parameters have to be known:

- the metabolic rate A (W/m^3)
- the blood flow coefficient B (W/Km^3)
- the heat capacity C (kJ/(kgK)) and
- the heat conductivity K (W/(mK))

Unlike for the electrical properties, where Gabriel et al. [72] basically defined a standard, no such standard is available or accepted for the thermal parameters. Therefore, a number of sources from the literature had to be used to gather data for all tissues, including the fetal tissue. A detailed overview for all models used including the tissues, values for all four thermal parameters and the literature source used is included in the Appendix (see A.3).

No values could be found in the literature for some of the fetal tissues (heart, lungs, stomach and CSF) and so the same values as for the adults were taken. The basal metabolic rate can be computed on the basis of the defined values for all fetal tissues and the mother (see Table 6-1). A good agreement with measurements could be demonstrated for all models at different gestational stages [73].

The thermal properties for the child models were derived from the adult values.

The values for the tissue-specific metabolic rates were scaled such as to fit with the basal metabolic rate (see A.3). The same scaling factor was used for the blood flow coefficient [74]. The specific heat capacity and heat conductivity is assumed to be the same as in adults [75].

3. Uncertainty Budgets of Numerical Dosimetry

The numerical dosimetry is affected by a number of uncertainties, caused by the discretization of a real world problem and the numerical simulation itself. It is important to be aware of these uncertainties to avoid common pitfalls (e.g. too coarse mesh, inadequate boundary conditions) and to get reliable results.

3.1. Disagreement between Simulation Model and Reality

Resolution and degree of detail of the human models

The resolution of the human voxel dataset should be as high as possible to reproduce the anatomical structure and envelope of the organs with a high degree of detail. In this work all models have been discretized with a resolution of 2mm. A detailed voxel model also reduces the well-known staircase effect, caused by the coarse surface of voxel models [78]. Samaras et al. [79] pointed out that this effect may compromise the thermal results.

The heat exchange between the human body and the ambient is a function of the outer surface (see chapter 2.1) but the surface of a voxel model is larger than the surface of the actual human.

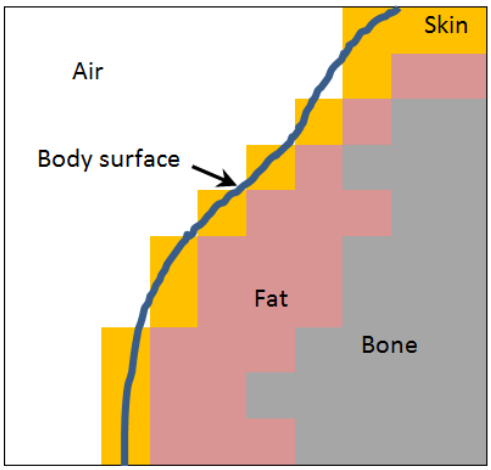

Figure 3-1: Small detail of a voxel model, showing the difference between the discretized surface and the actual body surface

Consequently, the energy outflow from a warm body would be overestimated and this would result in an underestimation of the temperature elevation caused by RF-EMF energy absorption.

Furthermore, it has to be considered that the large anatomical variability of humans may restrict the results gathered with a single model. Nevertheless, the use of a number of models, varying in age, size and height, allows for a minimizing of this uncertainty [78].

Electromagnetic source

In most cases an exact reproduction of the electromagnetic source is impossible. Such an accurate copy of the real world source would add too much detail and lead to a disproportionally long simulation time so reasonable simplifications might be inevitable [76]. The power generator feeding the medical diathermy applicator, for example, can be replaced with a simple numerical electric source, provided that the exposure itself is not compromised. Nevertheless, the validity of these simplifications must be demonstrated. This can be achieved by comparing the electromagnetic fields to the theoretically expected fields and, preferably, to real world measurements. A sufficient conformity could be demonstrated for all electromagnetic sources used in this work. The deviation from homogeneous electromagnetic fields was less than 0.5% for the plane wave exposure [77].

Similarly, a good adaptation of the MRI coil could be demonstrated (see chapter 0). The magnetic field inside the coils is homogeneous. Furthermore, the deviation from

the resonance frequency for none of the used coils is larger than 1%, which is in good agreement with the results of a previous study [76].
The agreement for the simulated medical diathermy applicator and real world field measurements achieved was better than 5% [77].

Physical properties of tissue

The uncertainty regarding the electrical properties is in the range of 10-15% [66] and up to 10% for the thermal properties [64]. The uncertainty is mainly caused by the measurement itself [66], the transferability of values based on animal tissue and ex vivo measurements.
Some recent models (e.g. the child models) are differentiated in up to 80 different tissues. Physical properties are not available for all of these tissues and therefore the same values may be assigned, based on reasonable assumptions, to different tissues (e.g. brain white matter = commissura anterior/ posterior).

3.2. Inaccuracy of the Numerical Simulation

Boundary conditions

The truncation of the computation domain is inevitable so suitable boundary conditions have to be chosen. Throughout this work open boundaries, producing no reflections, are used for the electromagnetic simulations. For the thermal simulations isothermal boundaries were chosen.
Several studies have investigated this uncertainty in the past. Finlay et al. [80] reported a variation of 1% of the SAR_{WB} based on the chosen boundary conditions.

Discretization error

The sampling of the electromagnetic field has to be sufficient in order to get reliable results so it is preferable that a high mesh is used. As a consequence the staircase effect, caused by the mesh adaptation of curved elements, is also reduced.

With regard to the voxel models, a mesh resolution of at least 2 mm, matching the voxel size, was used whenever possible.

Computation method

The dominant factors defining the uncertainty of the FIT are the accuracy settings for the solvers and they therefore have to be chosen carefully to ensure an uncertainty of a maximum of 5 % [51]. Hence, the remaining energy in the system had to decline fall below -30dB for the electromagnetic simulations. An accuracy of 10^{-12} has been chosen for the thermal steady state simulations. The transient thermal solver is based on an adaptive time integration method whose accuracy was set to 10^{-9}.

4. Validation of the Numerical Methods

In order to ensure the reliability of the numerical simulations, an extensive validation of the models used, discretization methods and solvers is needed. This includes a validation of the electromagnetic simulations, the thermal simulations carried out with the ordinary BHT-equation and a validation of the additionally implemented thermoregulatory mechanism.

4.1. Validation of the Finite Integration Technique

The standard EN 62311:2007, “Assessment of electronic and electrical equipment related to human exposure restrictions for electromagnetic fields (0 Hz - 300GHz)”, defines a method to validate the computed electromagnetic field distribution. An extremely simplified homogenous human model is used for this purpose.
The model is a cube with an edge length of 0.4 x 0.4 x 1.8 m and an electrical conductivity of 0.1 S/m. The magnetic field source is a quadratic current path (50 mm edge length), driven by 1 A at 50 Hz. The distance between coil and cube has to be 10 mm.

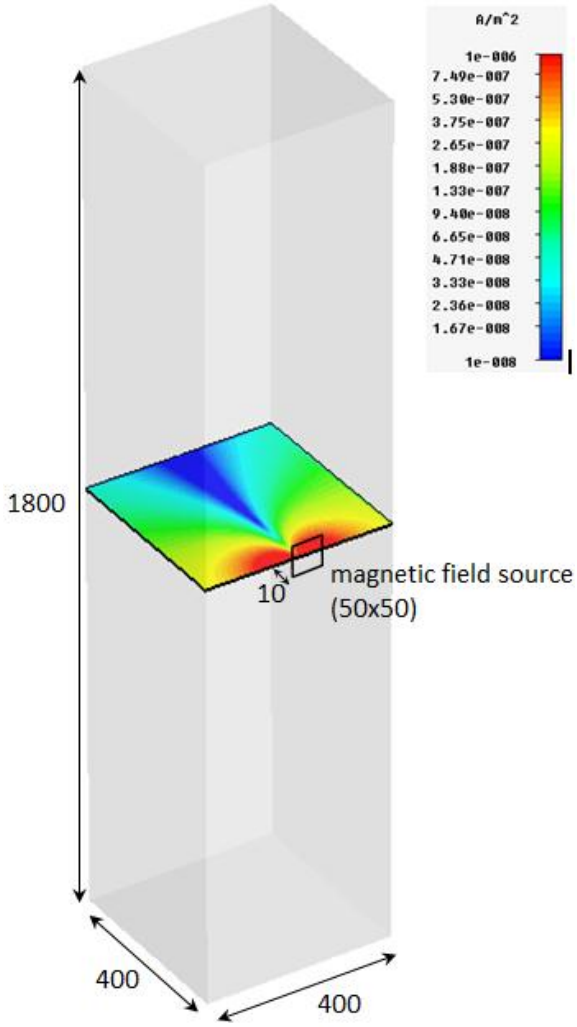

Figure 4-1: Extremely simplified human model for the validation of the FIT. All dimensions are given in millimeters. The cross section in the middle of the model shows the induced current density distribution at the height of the maximum.

The induced current density must be in the range of 6.28 μA/m² ±10 % [81].

The maximal current density obtained of 6.1 μA/m², is well within the allowed range and deviates only by 2.8%, demonstrating the validity of the FIT with regard to this standard.

4.2. Validation of the Bioheat Transfer Equation

The validation of the BHT equation is based on a simplified model first used by Christ et al. [82]. They used a one-dimensional model of the rear abdominal region to investigate the impact of layered tissues exposed to plane waves. This model was further

used by Samaras et al. [79] to compute the temperature elevation caused by RF-EMF energy. Both studies were performed with the FDTD method.

To minimize the impact of the model parameters, special care was taken to reproduce the described exposure scenario. The one-dimensionality of the model was taken into account by an adequate selection of the thermal and electromagnetic boundary conditions (see Figure 4-2). The adiabatic boundaries prevent a heat loss through this face. Furthermore, the truncation of the kidney was implemented by assuming a constant temperature of 37°C at this boundary.

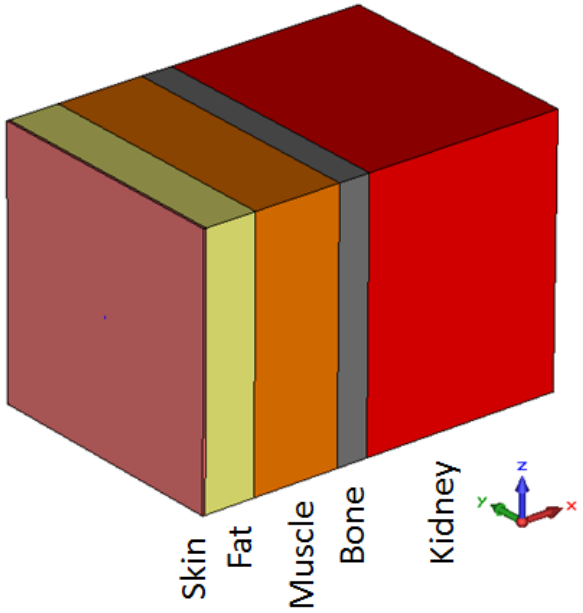

	boundary conditions	
	electromagnetic	thermal
x_{min}	open	open
x_{max}	$H_t = 0$	$T_{const} = 37°C$
y_{min}	$H_t = 0$	adiabatic
y_{max}	$H_t = 0$	adiabatic
z_{min}	$H_t = 0$	adiabatic
z_{max}	$H_t = 0$	adiabatic

Figure 4-2: Simplified model of the rear abdominal region and boundary conditions used to reproduce the original model.

Table 4-1 summarizes the electrical [82] and thermal properties used [79]. A vertically polarized electromagnetic plane wave at 2450 MHz was used. The background temperature was set at 22°C in combination with a heat transfer coefficient on the skin/air interface of 7 W/(m^2°C). The blood temperature was set at 37°C.

	thickness (mm)	**ε_r**	**σ (S/m)**	**ρ (kg/m3)**	**c (W/(Km))**	**K (kJ/(Kkg))**	**B (W/(Km^3))**	**A (W/m^3)**
Skin	0.4	38	1.46	1100	0.35	3.437	7170	1620
Fat	7.8	10.8	0.27	916	0.25	2.524	1671	300
Muscle	13.4	52.7	1.74	1041	0.53	3.546	1969	480
Bone	4.8	11.4	0.39	1990	0.4	1.289	2936	610
Kidney	30.6	52.7	2.43	1042	0.52	3.745	270000	48000

Table 4-1: Thickness of the tissue layer together with the electrical and thermal tissue properties.

First, the absorbed energy in the model was computed. The results were scaled to a SAR_{10g} of 2W/kg. The results agree very well (see Figure 4-3 upper part), although they were carried out with different computational methods. The overall divergence is about 4% percent.

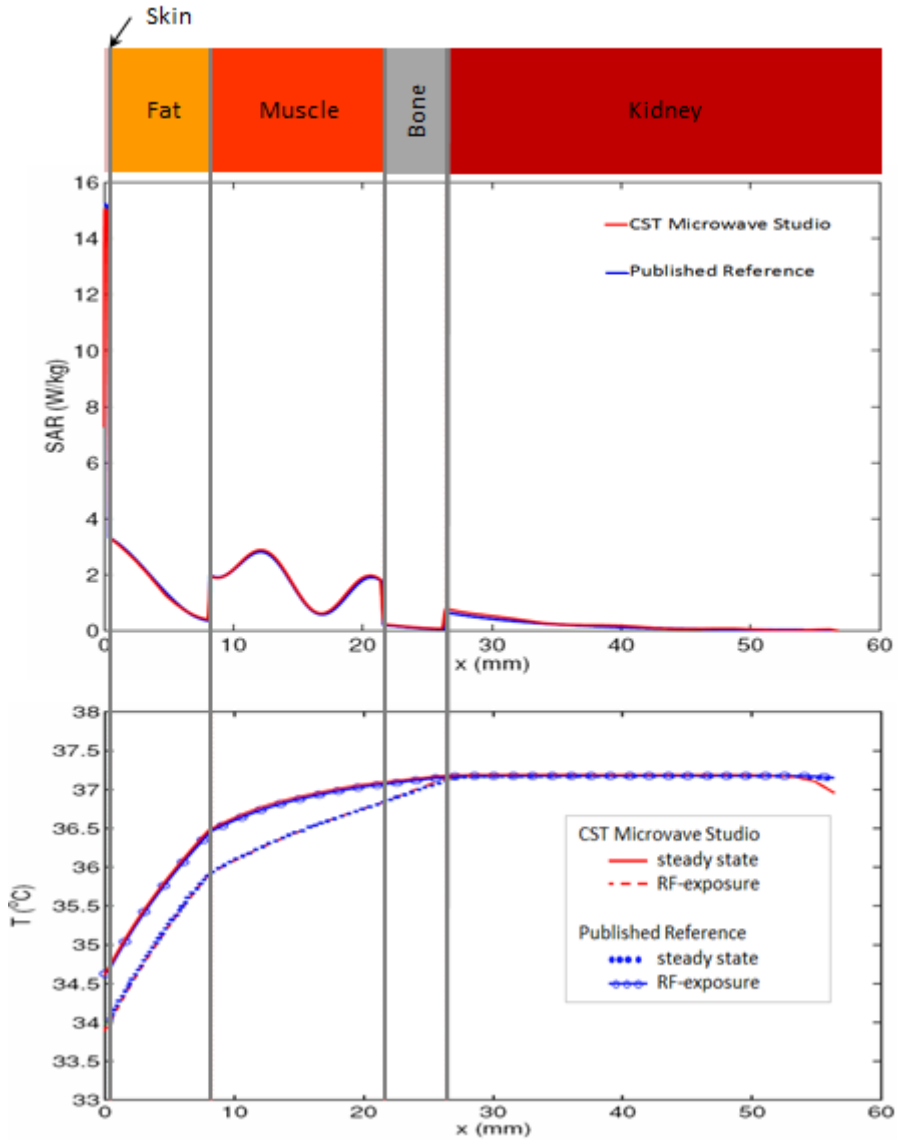

Figure 4-3: Specific absorption rate in the simplified rear abdominal area (upper chart) and the steady state temperature together with the RF-EMF energy induced temperature elevation (lower chart).

The same compliance could be shown for the steady state temperature (see Figure 4-3 lower part) with no RF-EMF energy applied. Finally, the temperature elevation caused by the RF-EMF energy was computed. Again, an almost perfect match between the results is demonstrated.

These results demonstrate the validity of the BHT equation.

4.3. Validation of the Thermoregulation Model

The validity of the thermoregulatory model developed is demonstrated by comparing the simulation data with experimental data. Only a few studies have been conducted where humans have been exposed to RF-EMF fields and the resulting temperature elevation monitored.

Adair et al. [83] investigated the thermo-physiological response on seven volunteers during a controlled whole-body exposure at 450 MHz. The sitting subjects were placed in the far field of a dipole antenna. The vertically polarized electromagnetic field propagates from anterior to posterior with an electrical field strength of 300 V/m. The temperature in the test chamber was kept constant at 31°C. The test person was first acclimatized for 30 minutes with the antenna switched off and then the subject was exposed for 45 min. During the exposure the temperature was measured continuously in six places. The temperature probes were placed on the anterior right thigh, left upper chest, left forearm, left upper back, central lower back and central forehead, However, only four of them were reported in the study results, the values for the anterior right thigh and the left forearm being excluded [85]. A mean skin temperature was derived from these temperature measurements. The body core temperature was recorded with a probe in the esophagus, at the level of the left atrium.

The NORMAN model was chosen for the simulations. Its height of 176 cm and weight of 73 kg are in good agreement with the average height (177 cm) and the average weight (76.3 kg) of the male subjects examined. It is well known that the posture of the model strongly affects the energy absorption [84] and, consequently, the temperature elevation in the body. The NORMAN model therefore had to be manipulated in Matlab© (see Figure 4-4) to reproduce the posture used in the study.

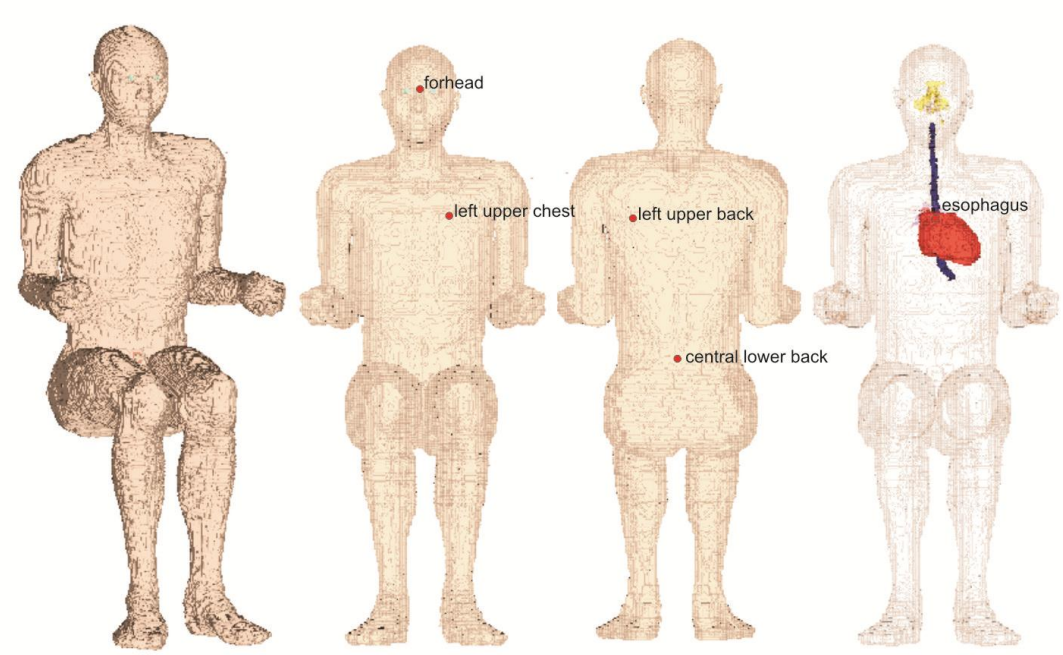

Figure 4-4: Various views of the NORMAN model in a sitting posture. The red dots highlight the positions of the temperature probes.

First, the energy absorption based on the described exposure setup was computed. The computed SAR_{WB} is 1.29 W/kg, exceeding the basic restrictions for occupational exposure by more than a factor of three.

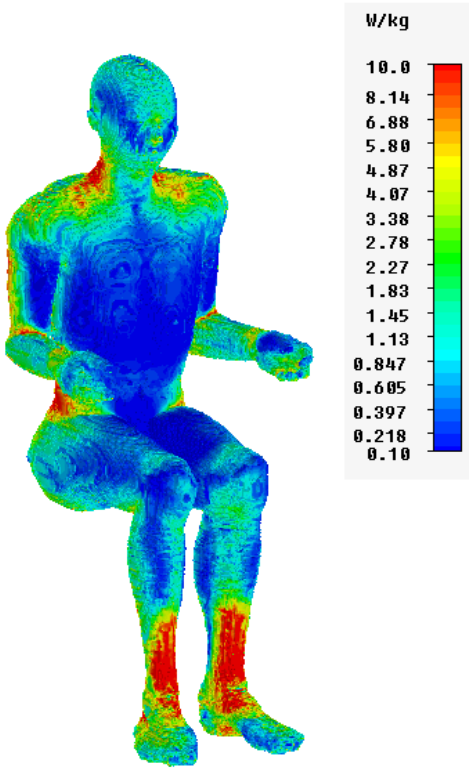

Figure 4-5: SAR on the surface of the sitting model, exposed to a vertical polarized plane wave.

Local maxima are located at the ankle, elbow joint, lower back and neck (see Figure 4-5).

Table 4-2 lists the thermal parameters used to establish a steady state temperature distribution at an ambient temperature of 31°C. The values for the internal and external insensible water loss and the heat transfer coefficient were derived based on the defined ambient temperature and the underlying assumptions of the thermal model (see chapter 2.1).

Thermal simulation parameters	
MR (W)	114.6
Pint (W)	9.05
Pext (W)	21.11
Hint (W/(m²K))	10.29
Hext (W/(m²K))	77.03
BV (ml)	5253

Table 4-2: Thermal parameters used to establish a steady state temperature distribution in the sitting NORMAN model for an ambient temperature of 31°C. The basal metabolic rate (MR), the insensible water loss in the lungs (Pint) and on the skin (Pext), the heat transfer coefficient in the lungs (H_{int}) and on the skin (H_{ext}) and the blood volume (BV) needed for the computation of the blood temperature.

This set of parameters ensures that the heat produced by the metabolic rate and the heat lost through convection, radiation and insensible water loss is in equilibrium. Figure 4-6 shows the temperature distribution on the model surface at rest.

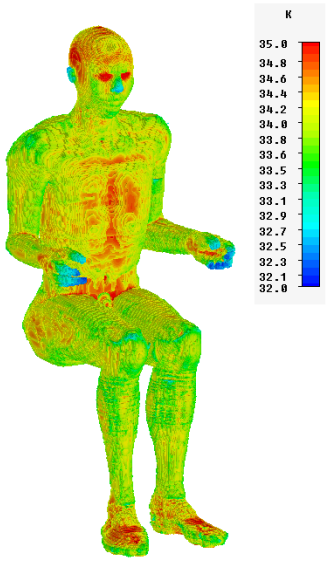

Figure 4-6: Steady state temperature distribution on the body surface of the sitting model NORMAN.

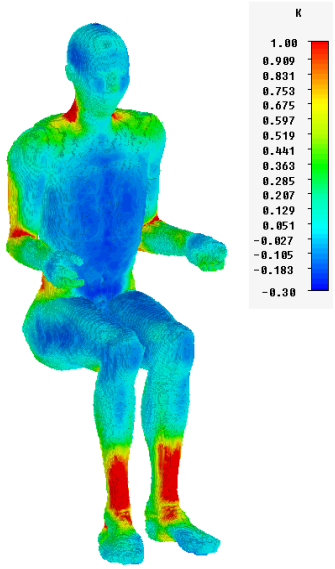

Figure 4-7: Temperature elevation on the body surface of the sitting model Norman, after an RF-EMF exposure of 45 min.

The temperature is highest in the thorax and in the head. The higher temperature in the head is attributed to the higher metabolic rate of the brain. In the extremities the temperature is lower, in particular in the body protrusions such as fingers and toes, including the nose, ears and chin. Adair et al. [83] reported an average skin temperature of 34.65°C (±0.65°C) and the developed thermal model calculates an average skin temperature of 34.63°C for the described exposure scenario after 45 min. Figure 4-7 illustrates the temperature distribution on the model surface after an RF-EMF exposure of 45 min.

A direct validation of the SAR computation results is not possible because Adair et al. [83] did not report any SAR measurement values. Figure 4-5 and Figure 4-7, however show a good agreement of the SAR distribution and the temperature elevation on the body surface.

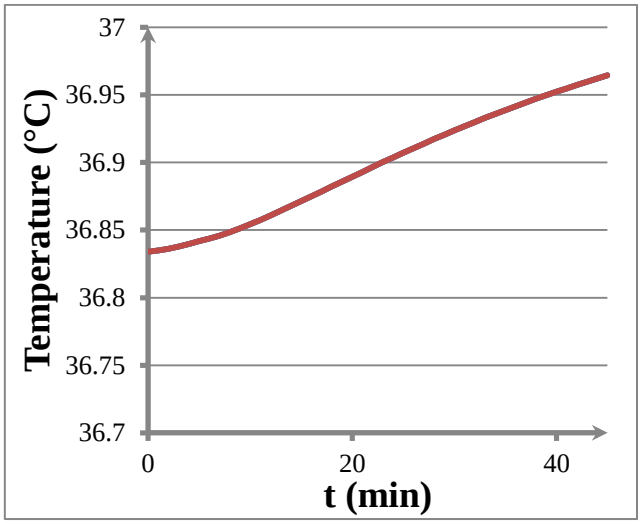

Figure 4-8: Temperature elevation in the esophagus at the level of the left atrium.

Adair et al [83] reported a mean steady state temperature of 36.85°C for the temperature measurement in the esophagus and a temperature elevation of 0.1°C during the exposure.

The model computes a steady state temperature in the esophagus of 36.84 °C (see Figure 4-8 for t=0) and an elevation of 0.12°C after 45 min. The thermoregulatory mechanisms try to keep the esophageal temperature, which is known to be a good estimation of the body core temperature, within a narrow range even in the presence of local hot spots, as revealed by the RF-EMF exposure.

Finally, Table 4-3 compares the measured group mean changes reported by Adair [83] with the simulation results obtained with the thermoregulation model implemented.

Positions	measured value ΔT(°C)	simulated results ΔT(°C)	deviation (%)
forehead	0.11	0.09	-18.2
left upper chest	-0.15	-0.12	-20.0
left upper back	0.62 (±0.25)	0.65	+4.8
central lower back	0.73 (±0.21)	0.59	-19.2
mean skin	0.23((±0.08)	0.25	+6.4

Table 4-3: Comparison of the measured group mean temperature elevation and the temperature elevation in the sitting model NORMAN.

A reduction in temperature for the left upper chest was noticed in the study. A similar pattern was found with the thermoregulation model. This fall in temperature is caused by sweating appearing all over the body and cooling down the skin, even in regions not directly exposed to the electromagnetic field (see Figure 4-5).

The simulation results for the left upper back, the central lower back and the mean skin temperature are within the reported standard deviations for the measured values. No standard deviation was reported for the forehead and the left upper chest. However, the deviation is at most 20%, due to the factors described in the previous chapter.

The simulation results discussed previously demonstrate the usefulness of the developed thermal model. The thermoregulatory model is able to accurately simulate the temperature elevation in high resolution anatomical models when exposed to RF-EMF.

5. RF-EMF induced Temperature Elevation in Children

5.1. Exposure Scenario

Recent publications using improved numerical anatomical models showed that the ICNIRP reference levels may not be conservative enough to adequately protect children [85] [86] [87] [88]. Only a few studies have been performed which computed EMF-induced temperature elevations in children [75] [89]. However, they suffered from using less realistic (downscaled adult) models [75] and/or simplified thermal algorithms which did not account for the effects of thermoregulatory mechanisms [89]. In this work, six high resolution real anatomical child models (see chapter 2.5.3) [62] have been used to compute the SAR induced by EMF exposure at reference levels to linearly polarized plane waves with the electric field vector aligned along the human body axis and propagating from anterior to posterior (Figure 5-1). The child models were isolated from the ground as this scenario was expected to lead to the highest SAR_{WB} values [20]. The investigated frequency range is from 10-1000 MHz.

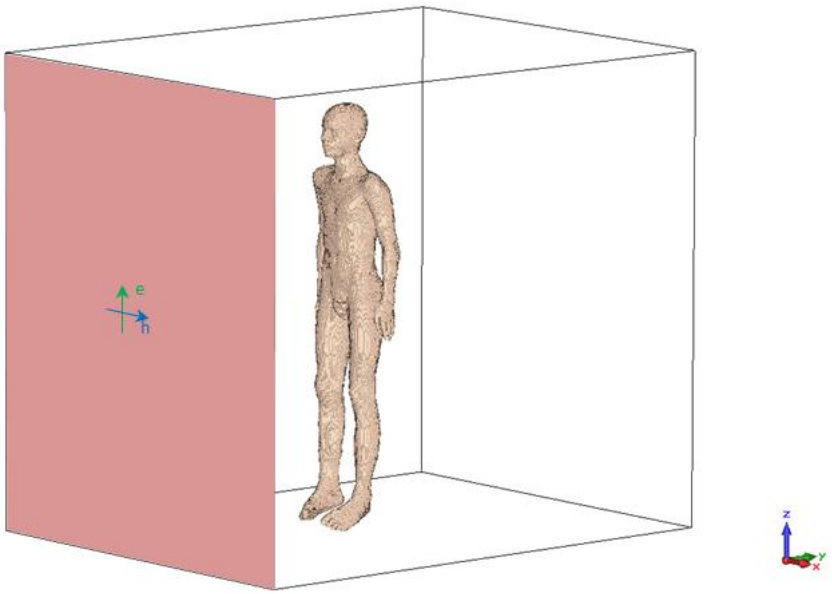

Figure 5-1: Linearly polarized plane wave with the electric field vector aligned along the human body axis, propagating from anterior to posterior.

The thermal parameters in Table 5-1 have been derived on the basis of the underlying assumptions of the thermal model (see chapter 2.1) and an ambient temperature of 28°C.

Name	MR (W)	P_{int} (W)	P_{ext} (W)	H_{ext} (W/(m²°C))	H_{int} (W/(m²°C))	S (m²)	BV (ml)
Louis	111.45	8.80	20.52	5.32	45.87	2.13	3583
Billie	83.35	6.58	15.35	5.41	38.92	1.65	2639
Dizzie	86.26	6.81	15.89	7.37	52.94	1.38	2029
Eartha	76.56	6.04	14.10	5.56	41.47	1.45	2341
Thelonius	80.44	6.35	14.82	8.69	56.66	1.09	1556
Roberta	67.84	5.36	12.50	7.99	47.93	1.00	1411

Table 5-1: Thermal properties of the child models, including the basal metabolic rate (MR), the insensible water loss in the lungs (P_{int}) and on the skin (P_{ext}), the heat transfer coefficient in the lungs (H_{int}) and on the skin (H_{ext}), the body surface (S) and the blood volume (BV).

5.2. Results

In the investigated frequency range of 10-1000 MHz the SAR_{WB} exhibits different peaks for each model. These peak values are due to the whole body resonance which, amongst others, is a function of the size and orientation of the model relative to the field vector [20]. Figure 5-2 shows the SAR_{WB} as a function of frequency. The corresponding maximum SAR_{WB} and resonance frequencies are listed in Table 5-2. Beyond the resonance frequency the SAR_{WB} declines and then increases again as a result of higher exposure due to increasing reference levels above 400MHz.

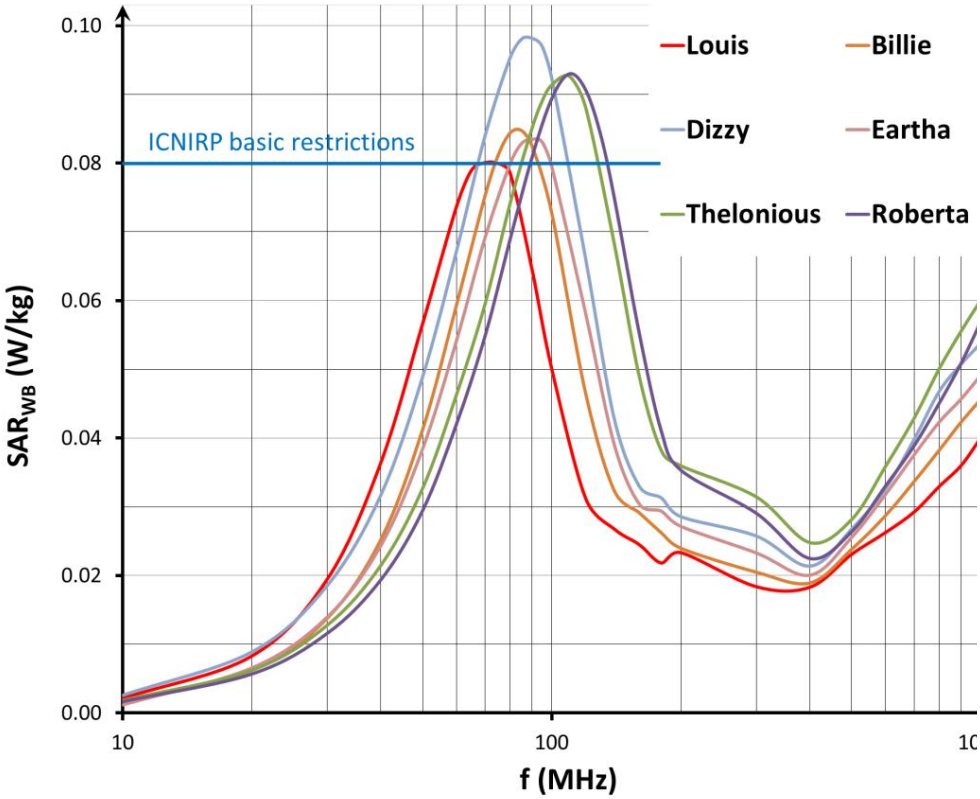

Figure 5-2: Whole body SAR of different child models in the frequency range 10-1000 MHz exposed at the ICNIRP reference levels.

The intracorporeal SAR distribution exhibits local maxima in the neck, knee and ankle (Figure 5-3).

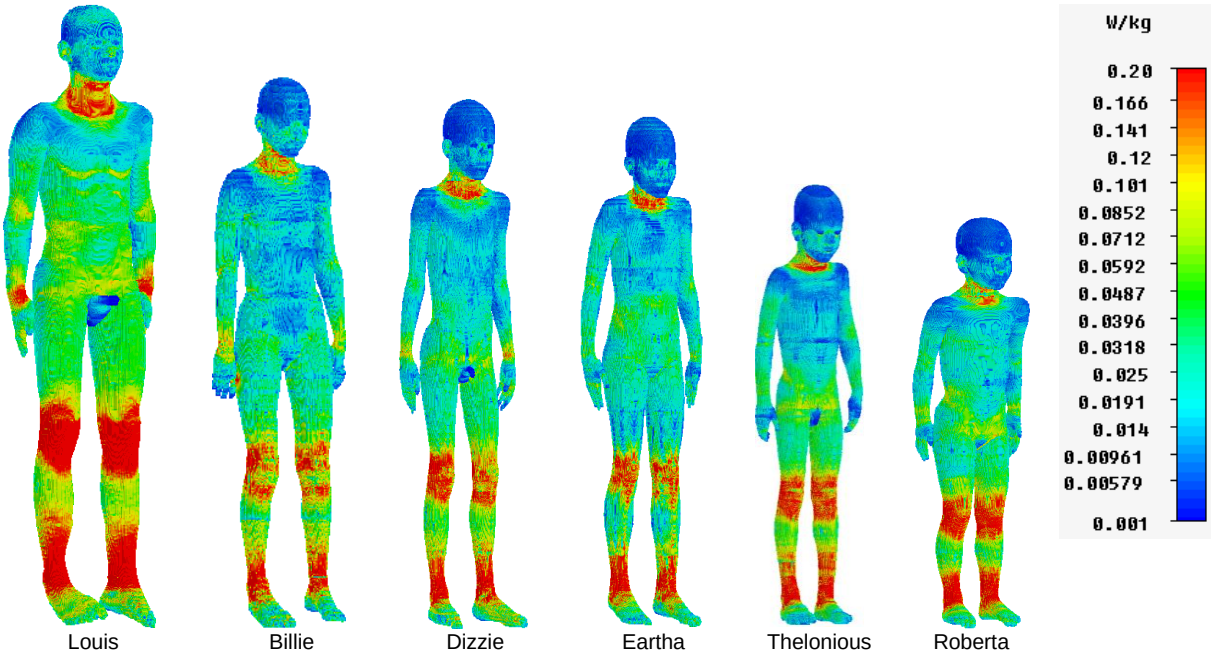

Figure 5-3: SAR distribution at the body surface due to RF-EMF exposure at ICNIRP reference levels at the model-specific resonance frequencies.

In contrast to ICNIRP's initial assumption, exposure at the reference levels resulted in an excess of ICNIRP basic restrictions in children smaller than 1.65 m. The over-exposure ranges from 4.3% (Eartha) to 22.7% (Dizzie). At the resonance frequencies the ratio between body height and the wavelength in air was 0.41±0.01. This is in good agreement with the findings of previous studies [85] [88] [90].

In contrast to SAR_{WB}, the local SAR averaged over 10g contiguous tissue did not exceed related basic restrictions in any of the child models. The maximum SAR_{10g} of all models occurs either in the left or the right knee except for the Dizzie model (left ankle) (Table 5-2).

Name	$SAR_{WB,max}$ (W/kg)	f_{res} (MHz)	SAR10g,max (W/kg)	ΔT_B (°C)	ΔT_{LOC} (°C)
Louis	0.080	70	2.19	1.32E-02	3.99E-01
Billie	0.085	85	1.44	1.38E-02	2.02E-01
Dizzie	0.098	90	1.96	1.37E-02	2.32E-01
Eartha	0.083	90	1.55	1.38E-02	2.71E-01
Thelonius	0.093	110	1.08	1.24E-02	1.46E-01
Roberta	0.093	110	1.66	1.28E-02	2.17E-01

Table 5-2 Calculated values at the ICNIRP reference levels for all models. Maximal whole body SAR ($SAR_{WB,max}$) at the resonance frequency , maximal local SAR averaged over 10g contiguous tissue ($SAR_{10g,max}$), blood temperature elevation (ΔTB) and maximal local temp (ΔT_{LOC}).

Figure 5-4 shows the temperature distribution at the body surface at the thermal steady state for the model Roberta. The temperature is highest at the thorax and in the head. The higher temperature in the head is attributed to the higher metabolic rate of the brain. The temperature is lower in the extremities, in particular in the body protrusions such as fingers and toes, including the nose, ears and chin. This is in good agreement with measurements [3].

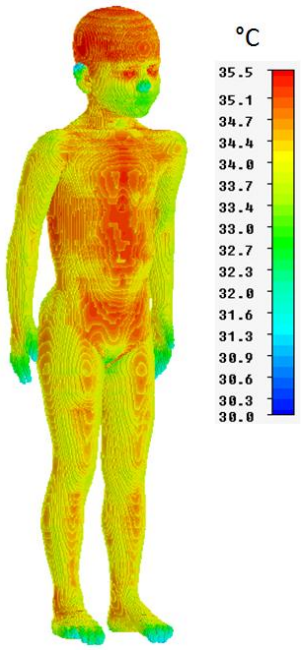

Figure 5-4: Steady state temperature distribution at the body surface of the model Roberta.

The temperature increase in child models exposed to RF-EMF at ICNIRP reference levels were computed for an exposure time of 30 min. During exposure the blood temperature elevation (which is equivalent to the core temperature elevation [27] [14]) is small (Table 5-2). The maximum temperature elevation is much higher and similar to the SAR_{10g} located in the left or right knee on the surface of the models. The average distance between the maximum SAR_{10g} and maximum temperature elevation was found to be 19 mm. Figure 5-5 shows the temperature elevation at the body surface after 30 min exposure at ICNIRP reference levels. Comparison of Figure 5-3 and Figure 5-5 demonstrates that SAR and temperature distributions are similar. Differences at body parts such as the head and chest can be explained by cooling due to sweating [27] [83]. A good agreement between SAR and temperature increase can be observed at layer-averaged values along the body axis as demonstrated at the model Dizzie (see Figure 5-6). The appreciable temperature elevation in body parts with low SAR, such as the head, is caused by heated blood.

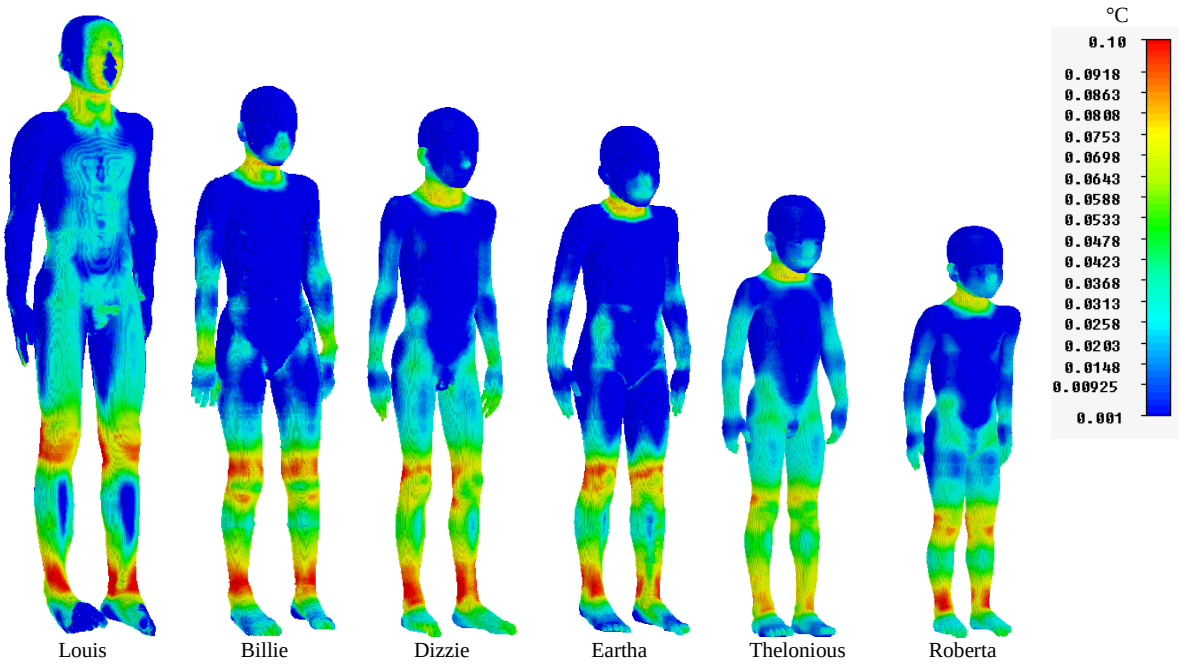

Figure 5-5: Temperature increase at the body surface after 30 min exposure at ICNIRP EMF reference levels at model-specific resonance frequencies.

The results of thermal modeling allowed the determination of RF-EMF exposures associated with a local or a whole body temperature increase of 1°C. The results show that this would require a SAR_{WB} of at least 5.78 W/kg (Louis) related to body core temperature and a SAR_{10g} of at least 5.5 W/kg (Louis) related to local temperature, respectively.

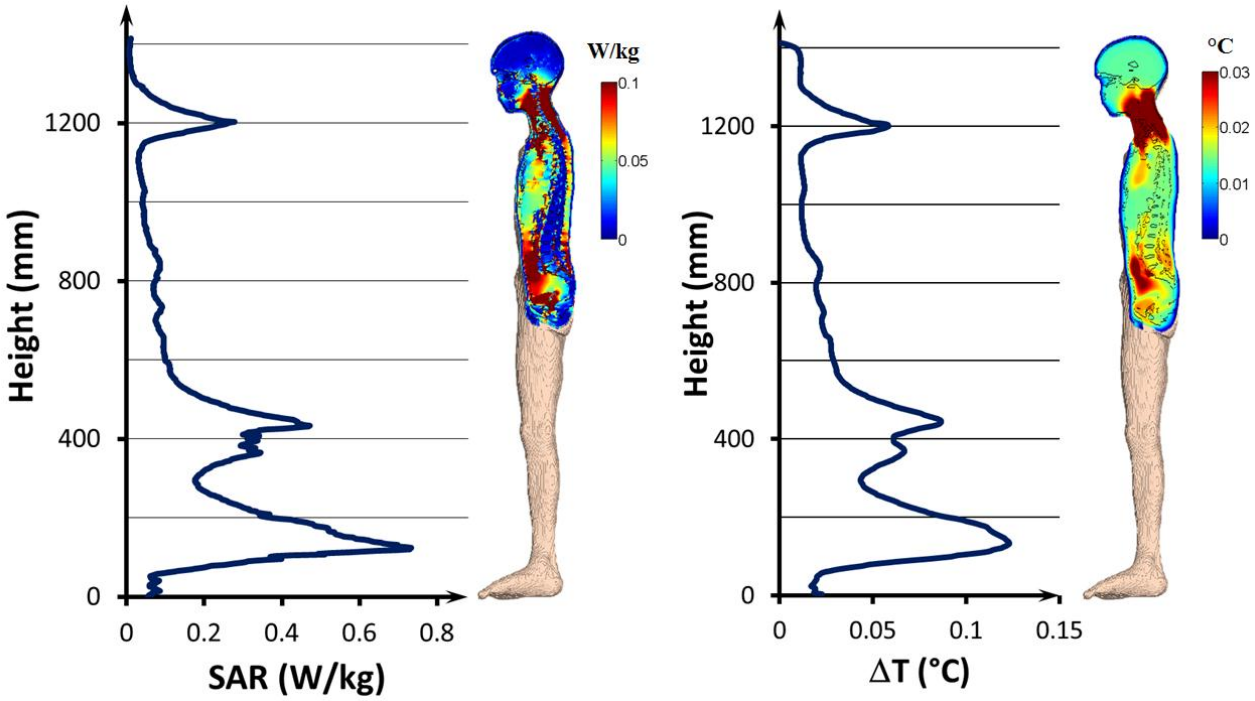

Figure 5-6: Average SAR, and temperature elevation along the body axis in the model Dizzie after 30 min exposure at ICNIRP reference levels. Moreover, the SAR and the temperature elevation inside the body are shown on a sagittal cross section.

5.3. Discussion

The numerical child models used are well accepted in the scientific community and are already used for health risk assessment of EMF exposures [87] [90] [89]. Recent publications including measurements and numerical simulations have investigated the age dependency of dielectric properties [87] [69]. These studies show that the SAR does no change systematically and only a small influence has been observed for children at different ages. Wang et al. [70] argue that the effect of the higher tissue conductivity might be compensated by the decreased EMF penetration depth due to the increased permittivity. It therefore seems justifiable to ignore age dependency, in children older than five years.

It could be shown that the SAR_{WB} basic restrictions may be exceeded in true anatomical child models exposed at ICNIRP reference levels. The basic restrictions were exceeded by up to 22.7%. The obtained values for the SAR_{WB} are in good agreement with previously published data, including scaled adult and anatomically correct child models [91] [85].

In contrast to this, no excess of the SAR_{10g} basic restrictions could be found. The maximum value of 2.2 W/kg was found in the leg of the Louis model and is well below the basic restriction (4 W/kg) for the extremities. The values are considerably higher than those reported by Bakker et al. [90]. However, they averaged SAR_{10g} over a cube as required by IEEE [56] which is up to 2.5fold less conservative than the contiguous tissue averaging [57] and explains the difference from published values.

Even when basic restrictions were exceeded, only marginal body core temperature variations were found. This is attributed to the consideration of thermoregulation which keeps the body core temperature close to 37°C. The factor to adverse body core temperature elevation (above 1°C) was 72.3 (Billie, Eartha). This finding was confirmed by thermal simulations at higher SAR_{WB}. In the child models the SAR_{WB} required to induce body core temperature elevations of 1°C is at least 44.5% higher than the initially assumed 4 W/kg [92] [26].

At reference level exposures, the temperature elevations at local hot spots are considerable higher. Depending on the model they vary between 0.15 and 0.4 °C This fits very well with the range of 0.2-0.7 °C reported in the literature [27] [14] [75]. However, this is considerably smaller than values reported elsewhere [89] where temper-

ature increases as high as 1°C were reported without, however, accounting for thermoregulatory mechanisms.

The factor of 73.2 related to a core temperature increase of 1°C is reduced to 2.5 (Louis) when related to a local temperature elevation of 1°C. This finding was also verified by thermal simulation at higher absorption rates. It could be shown that the basic restriction for the localized SAR is conservative enough to prevent thermal hot spots exceeding 1°C. A violation of the limit for the SAR_{10g} of at least 37.5% is needed to produce such a hot spot.

5.4. Conclusion

It could be confirmed that ICNIRP's basic restrictions regarding SAR_{WB} may be exceeded if children are exposed to RF-EMF at reference levels while SAR_{10g} basic restrictions are met. However, it could also be demonstrated that neglecting thermoregulation was conservative enough to prevent dangerous tissue heating. By improved thermal modeling and studying children of different ages and sizes it could be demonstrated that, even in cases were basic restrictions were exceeded, temperature elevations remained below adverse levels.

Nevertheless, there is still a lack of information regarding thermoregulation in children. Further research, including measurements, is needed to improve thermoregulatory modeling further.

6. RF-EMF induced Temperature Elevation in Fetuses

6.1. Exposure Scenario

The World Health Organization (WHO) highlighted the importance of EMF dosimetry in embryos in 2006 [93] and reinforced the scientific importance of such studies in 2010 [94]. In its latest review, the ICNIRP concluded that there is a great need for temperature simulations for pregnant women to further asses the risk of RF-EMF exposure of the fetus [15].

To date, the ICNIRP has not regulated the exposure of the fetus, mainly because the RF-EMF energy induced temperature elevation could not be linked to a specific absorption rate in the fetus [95].

In 2004, the ICNIRP published a statement with regard to MRI [96]. According to this publication no adverse health effects occur in the fetus for temperature elevations that do not exceed 0.5°C and if the core temperature of the fetus is kept below 38°C. In general, the body core temperature of the fetus is about 0.5°C higher than the core temperature of the mother because of the high level of metabolism in the fetus. Furthermore, the heat exchange from the fetus is limited by the placental barrier and this may further increase the health risk for the fetus [96].

In the past, several studies have been performed to estimate the risk during MRI. Wu et al. [97] used nine pregnant models, one for each month of pregnancy, to compute the temperature elevation at 64 and 128 MHz. Only the ordinary BHT equation was used for the thermal simulations. They concluded that the temperature elevation is generally higher during the later stages of pregnancy. Hand et al. [34] performed a similar study, using one pregnant model in the 26$^{th.}$-week of gestation and the ordinary BHT equation.

Kikuchi et al. [98] pointed out that the variation of the blood temperature is of crucial importance, since the fetus is located deep inside the body and strongly affected by this effect. Consequently, they considered thermoregulatory mechanisms in their

temperature simulations but only one pregnant model in the 26th week of gestation was used for the simulations.

Several other studies have investigated the SAR over a large frequency range. Kawai et al. [95] found no violation of the ICNIRP basic restrictions in two embryos exposed at the ICNIRP reference level. In another study Dimbylow et al. [99] used three pregnant models (13th-38th weeks gestation). They showed that the ICNIRP basic restriction of 2W/kg for the SAR_{10g} is very conservative with regard to the protection of the fetus. Nagaoka et al. [100] showed that the SAR_{WB} in a pregnant woman in the 26th week of gestation is almost the same as in a non-pregnant woman. Moreover, they were able to demonstrate that the SAR_{WB} in the fetus is generally much lower than the SAR_{WB} of the mother.

However, none of these studies has computed the RF-EMF energy induced temperature elevation. In general, there a fewer studies investigating the exposure in the early stages of pregnancy than in the second and/or third trimester of pregnancy.

In this work, 14 pregnant models covering the 9th-34.5th weeks of pregnancy (see chapter 2.5.2) were exposed to a linearly polarized plane wave at the ICNIRP reference level, propagating from anterior to posterior under isolated conditions.

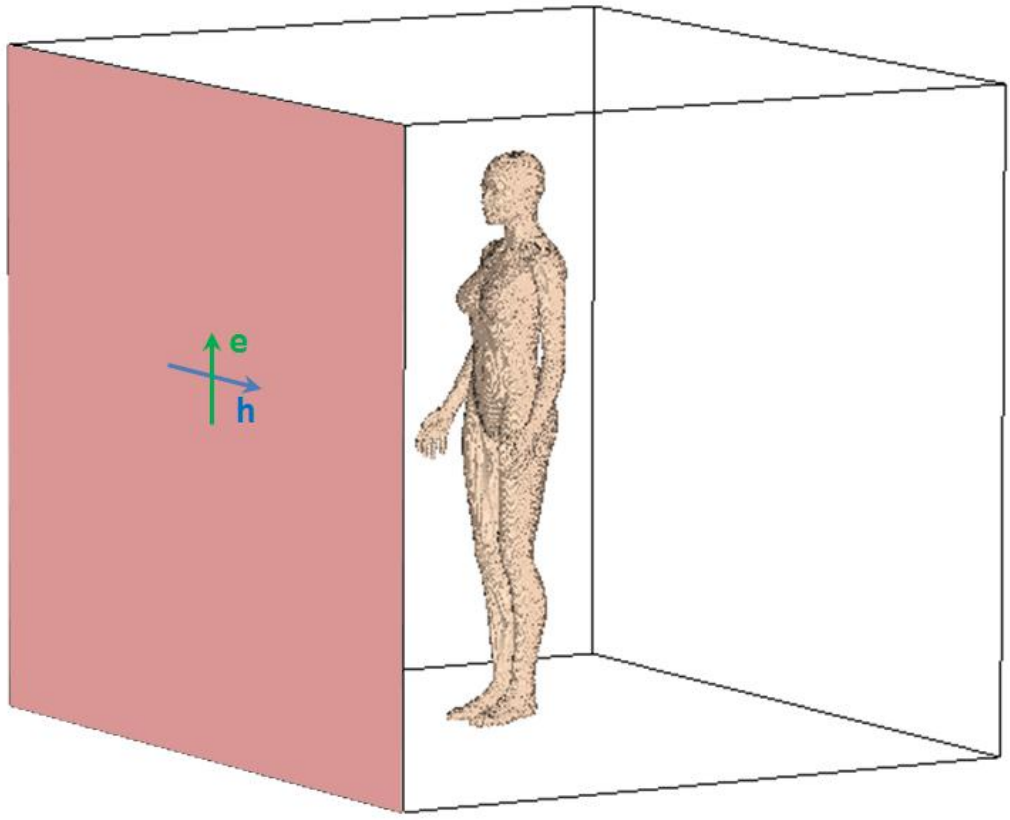

Figure 6-1: Linearly polarized plane wave with the electric field vector aligned along the human body axis, propagating from anterior to posterior.

The frequency range of 10-1000 MHz was chosen to cover the whole-body resonance where the SAR_{WB} is known to be at its maximum. Furthermore, the $SAR_{10g,max}$ was computed for each fetus and for the whole frequency range.

Thermal simulations were performed for each model at the resonance frequency. The thermal parameters in Table 6-1 have been derived on the basis of the underlying assumptions of the thermal model (see chapter 2.1) and an ambient temperature of 28 °C.

	MR (W)	P (W)	H (W/m²°C)	S (m²)	BV (ml)
US 2	80.34	31.40	2.88	2.13	3702
US4	84.14	32.88	3.01	2.13	3703
MRI 1	97.40	38.07	3.43	2.16	3836
MRI 2	97.86	38.25	3.44	2.17	3845
MRI 3	96.32	37.65	3.38	2.17	3827
MRI 4	88.40	34.55	3.13	2.15	3755
MRI 5	110.00	42.99	3.72	2.25	4155.
MRI 6	95.35	37.26	3.35	2.17	3849
MRI 7	93.51	36.55	3.28	2.17	3850
MRI 8	100.31	39.20	3.53	2.17	3830.48
MRI 9	96.53	37.73	3.40	2.16	3810.26
MRI 10	105.08	41.07	3.68	2.18	3891.56
MRI 11	109.44	42.77	3.82	2.18	3897.60
MRI 12	114.42	44.72	3.92	2.23	4115.75

Table 6-1: Thermal properties of the FEMONUM models, including the basal metabolic rate (MR), the insensible water loss (P), the heat transfer coefficient (H), the body surface (S) and the blood volume (BV).

6.2. Results

Figure 6-2 illustrates the SAR_{WB} of the mother for all 14 pregnant models as a function of the frequency. The maximum SAR_{WB} occurs in all models at 75 MHz and the corresponding values are listed in Table 6-2.

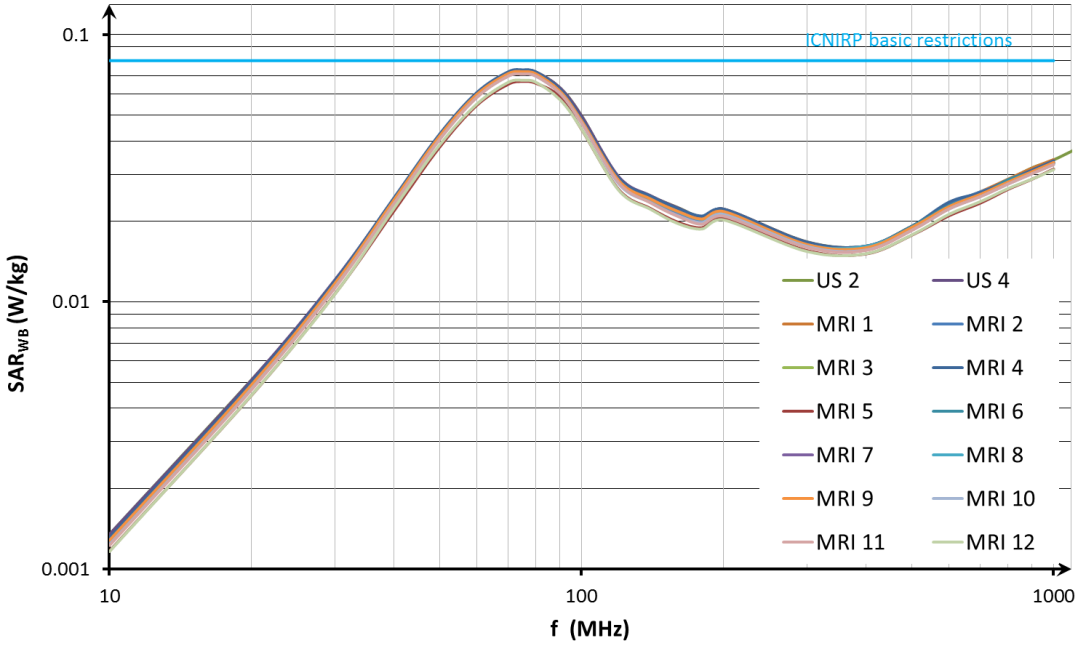

Figure 6-2: Whole body SAR in the mother for pregnant models in the frequency range 10-1000 MHz exposed at the ICNIRP reference levels.

The difference of the SAR_{WB} in the mother between all models is at most 15%, with an average of 10.8%. The SAR_{WB} in the fetus varies quite remarkably between the different models (see Figure 6-3). The frequency leading to the highest SAR_{WB} in the fetus is the same as in the mother, except for the model US 2. An increase of the SAR_{WB} in the corresponding fetus was observed as the frequency increased. This is caused by the lower penetration depth of the EMF in this frequency range and the fact that the fetus is located closer to the surface in early pregnancy. Consequently, the frequency range was increased to 3GHz, revealing a maximum at 1.2GHz. The values for all maxima are listed in Table 6-2.

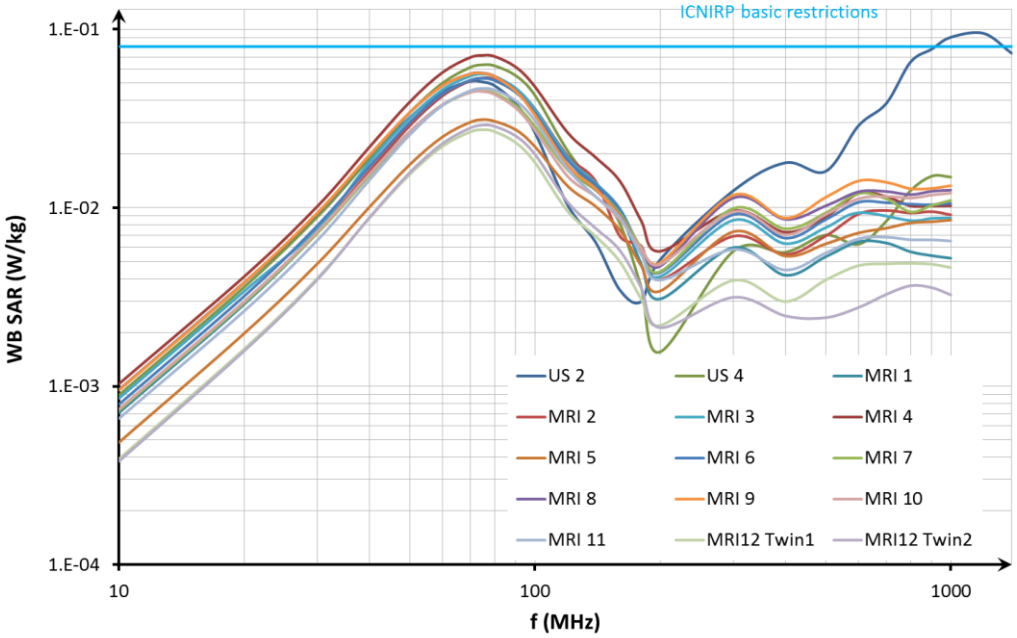

Figure 6-3: Whole body SAR in the fetus for pregnant models in the frequency range 10-1000 MHz exposed at the ICNIRP reference levels.

A similar diversity was revealed for the SAR_{10g}. Figure 6-4 shows the SAR_{10g} for the whole frequency range and all models.

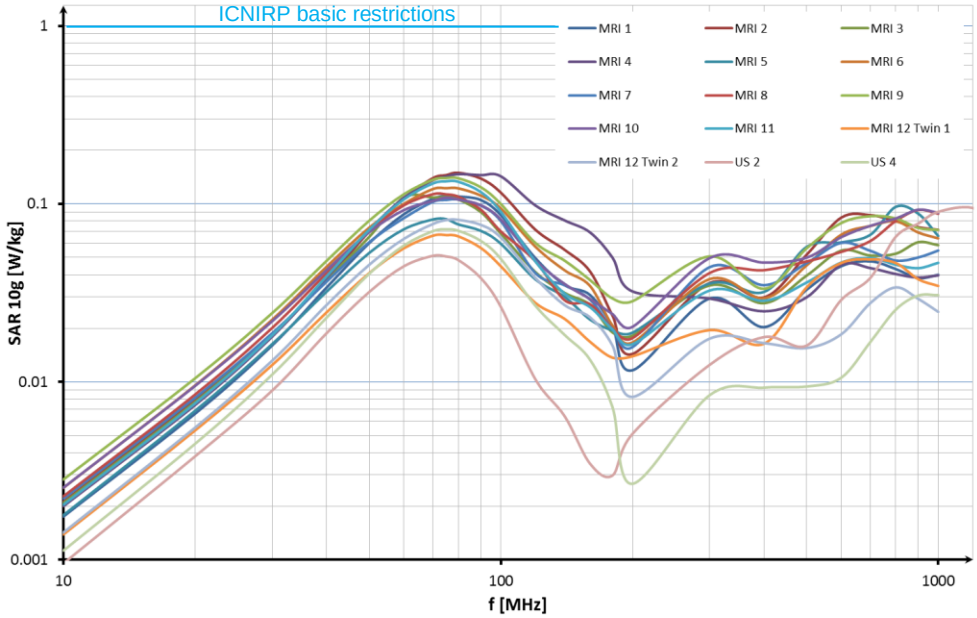

Figure 6-4: Localized SAR averaged over 10 g contiguous tissue in the fetus for all pregnant models in the frequency range 10-1000 MHz exposed at the ICNIRP reference levels.

The SAR_{10g} peaks in the frequency range of 70-80 MHz for all models except the US 2 model. The masses of the US 2 fetus (2.8 g) and the US 4 fetus (3.8 g) are less than 10g, therefore the SAR_{WB} equals the SAR_{10g}. Table 6-2 lists the maximal SAR_{10g} and the frequency where the maximum occurs. The maximum SAR_{10g} is located in the CSF for all models, except the US 2 and US 4 model with no differentiation of the fetus.

The penetration depth of the EMF is inversely proportional to the frequency. Therefore the location of SAR_{10g} might change with frequency. An example of this effect is shown for the model MRI 4 (see Figure 6-5). The maximum is located in the CSF for frequencies up to 200 MHz, then in the fetal body up to 600 MHz and finally in the brain at even higher frequencies.

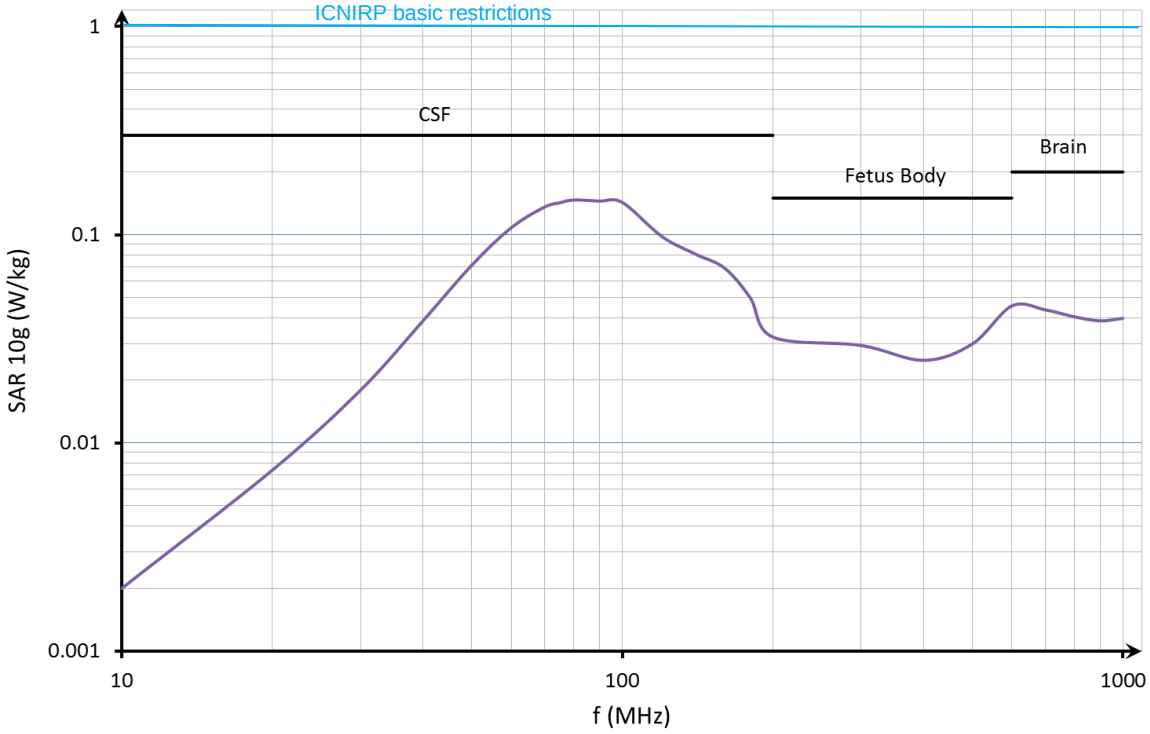

Figure 6-5: Localized SAR averaged over 10 g contiguous tissue in the fetus for the model MRI 4 and the associated tissue where the maximum occurs.

	$f_{res,WB\ Mother}$ (MHz)	$SAR_{WB\ Mother,max}$ (W/kg)	$f_{res,WB\ Fetus}$ (MHz)	$SAR_{WB\ Fetus,max}$ (W/kg)	$f_{res,10g}$ (MHz)	$SAR10g,max$ (W/kg)
US2	75	0.073	1200	0.095	1200	0.095
US4	75	0.073	75	0.063	75	0.063
MRI1	75	0.072	75	0.053	75	0.111
MRI2	75	0.072	75	0.053	80	0.150
MRI3	75	0.072	75	0.056	75	0.109
MRI4	75	0.074	75	0.071	80	0.147
MRI5	75	0.067	75	0.031	75	0.082
MRI6	75	0.072	75	0.053	75	0.123
MRI7	75	0.072	75	0.045	80	0.106
MRI8	75	0.072	75	0.057	70	0.113
MRI9	75	0.073	75	0.057	75	0.140
MRI10	75	0.071	75	0.045	75	0.108
MRI11	75	0.071	75	0.047	75	0.134
MRI12	75	0.068	75	0.027^{TWIN1} 0.029^{TWIN2}	75	0.067^{TWIN1} 0.0814^{TWIN2}

Table 6-2: Calculated SAR values at the ICNIRP reference levels for all pregnant models.

On the basis of these results, it was possible to compute the electric field values required to exceed the ICNIRP basic restrictions in the fetus. As has been mentioned before, the ICNIRP does not provide regulations for the absorption in the fetus specifically and, therefore the limits for the general public have been used. Figure 6-6 illustrates the electric field strength needed to produce a $SAR_{WB,Fetus}$ of 0.08 W/kg and Figure 6-7 the electric field strength needed to produce a $SAR_{10g,Fetus}$ of 2 W/kg.

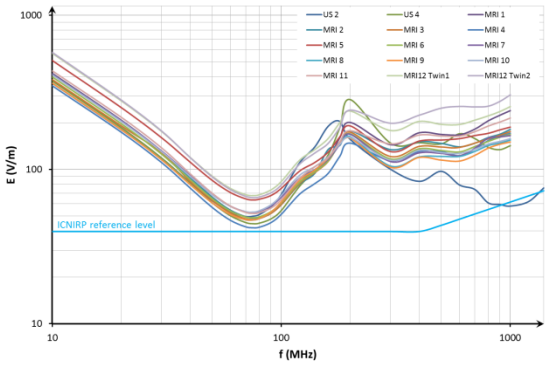

Figure 6-6: The minimal electric field strength needed to produce the ICNIRP basic restriction of 0.08 W/kg for the SAR_{WB} in the fetus. The ICNIRP reference levels are shown.

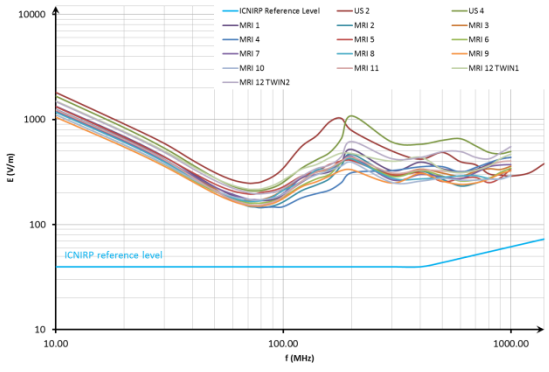

Figure 6-7: The minimal electric field strength needed to produce the ICNIRP basic restriction of 2 W/kg for the SAR_{10g} in the fetus. The ICNIRP reference levels are also shown.

Before the actual thermal simulations were performed the usefulness of the thermal parameters in Table 6-1 had to be proven. It could be shown that the parameters are suitable for the establishment of a steady thermal state in all models. Another finding in these simulations was that the computed core temperature in all fetuses is, on av-

erage, 0.4°C higher than the core temperature of the mother. This is in good agreement with the literature which reports a difference of up to 0.5°C [96].

The temperature elevation in the pregnant models exposed at the ICNIRP reference level were computed for 30 min, at all resonance frequencies of $SAR_{WB,Fetus}$. During the exposure the blood temperature elevation in the mother, which equals the body core temperature, was quite small (see Table 6-3) with an average temperature elevation of 0.016 °C. Only the body core temperature elevation in the US 2 model was considerably smaller (0.008°C) due to the limited penetration depth of RF-EMF energy at 1.2GHz.

Model	$\Delta T_{B,Mother}$ (°C)	$\Delta T_{AVG,Fetus}$ (°C)	$\Delta T_{MAX,Fetus}$ (°C)
US2	0.008	0.012	0.014
US4	0.017	0.022	0.028
MRI1	0.017	0.021	0.030
MRI2	0.017	0.021	0.028
MRI3	0.017	0.021	0.028
MRI4	0.017	0.023	0.038
MRI5	0.016	0.017	0.023
MRI6	0.017	0.021	0.028
MRI7	0.016	0.020	0.024
MRI8	0.017	0.021	0.027
MRI9	0.017	0.021	0.028
MRI10	0.017	0.019	0.023
MRI11	0.016	0.019	0.026
$MRI12^{Twin1}$	0.016	0.017	0.022
$MRI12^{Twin2}$		0.017	0.023

Table 6-3: Temperature elevation in all pregnant models after an exposure of 30 min. at the ICNIRP reference level. Blood temperature of the mother ($\Delta T_{B,Mother}$), average temperature elevation in the fetus ($\Delta T_{AVG,Fetus}$) and maximal temperature elevation in the fetus ($\Delta T_{MAX,Fetus}$).

The temperature elevation in the fetus is, on average, 23% higher than in the mother. The maximal temperature elevation in the fetus is even more pronounced and was as high as 0.038 °C in the MRI 4 model.

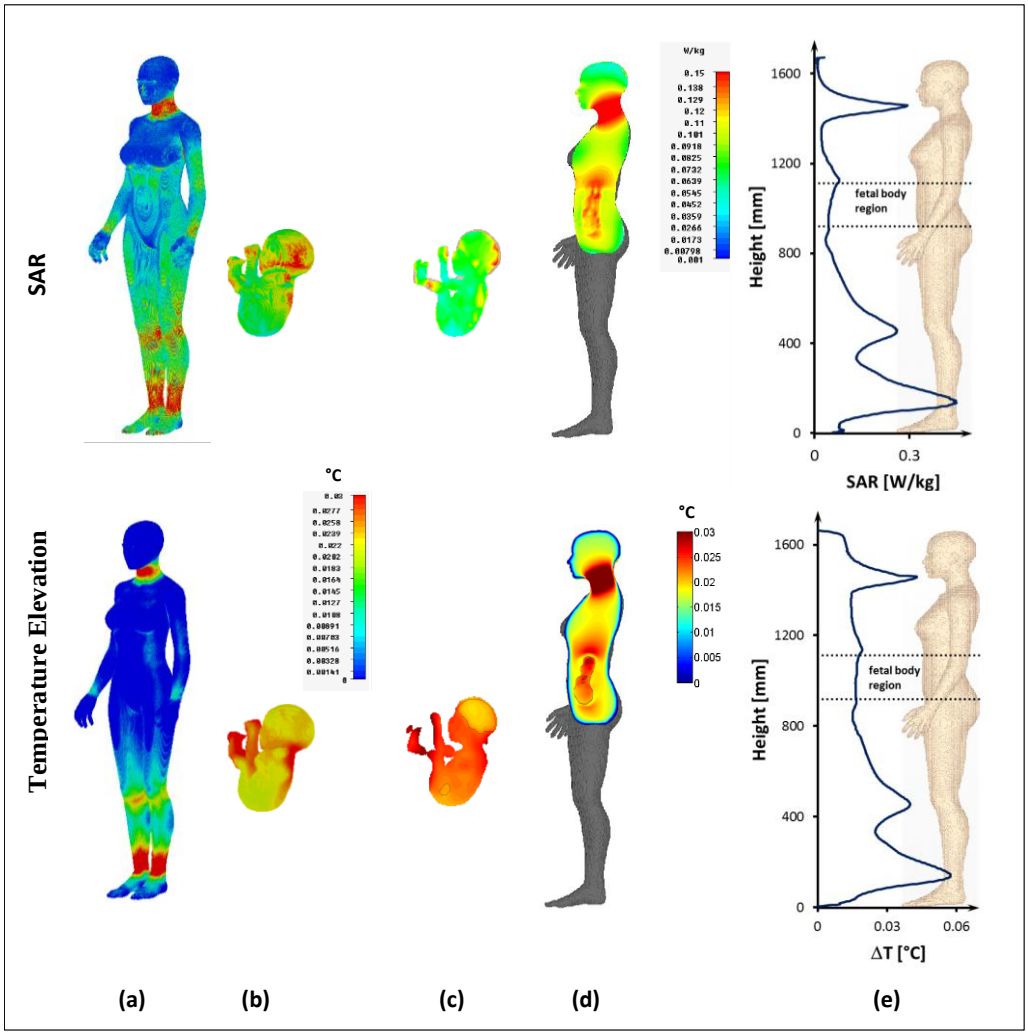

Figure 6-8: SAR and Temperature elevation in the MRI 4 model: (a) body surface mother, (b) body surface fetus, (c) sagittal plane of the fetus, (d) sagittal plane of the mother, (e) layer averaged SAR and temperature elevation along the body axis.

Figure 6-8 gives an overview of the SAR and the related temperature elevation in the MRI 4 model. Similar behavior was found for all models. The SAR exhibits local maxima in the neck, knees and ankle of the mother and, consequently, the temperature elevation is highest in these body regions. The exposure of the head of the mother and the fetal body region is quite small: the warming in these regions is primarily caused by the circulating warmed blood.

The temperature elevation in the fetus also fits pretty well with the SAR distribution in the fetus, leading to local hotspots in the neck and the toes of the fetus. The fetal body is warmed uniformly. Only the temperature elevation in the fetal brain is considerably smaller, due to the high blood perfusion of this organ.

The results of the thermal modeling allowed the determination of RF-EMF exposures associated with a core temperature elevation of 1°C in the mother, a core tempera-

ture elevation of 0.5°C in the fetus and a maximal local temperature elevation of 0.5°C in the fetus for an exposure time of 30 min. These additional simulations were performed for the MRI 4 model, where the greatest temperature elevation in the fetus was found (see Table 6-3). Table 6-4 summarizes the results for these simulations.

	$SAR_{WB\ Mother,max}$ (W/kg)	$SAR_{WB\ Fetus,max}$ (W/kg)	SAR10g,max (W/kg)	$\Delta T_{B,Mother}$ (°C)	$\Delta T_{AVG,Fetus}$ (°C)	$\Delta T_{MAX,Fetus}$ (°C)
a)	0.07	0.07	0.15	0.02	0.02	0.04
b)	0.35	0.34	0.70	0.08	0.11	0.18
c)	4.52	4.34	8.98	**1.00**	1.33	2.23
d)	1.70	1.63	3.38	0.38	**0.50**	0.85
e)	0.99	0.95	1.98	0.23	0.30	**0.50**

Table 6-4: SAR and temperature elevation in the mother and the fetus for different conditions: a) at the ICNIRP reference level for the general public, b) at the ICNIRP reference level for occupational exposure, c) at an RF-EMF exposure that provokes a body core temperature elevation of 1°C in the mother, d) at an RF-EMF exposure that provokes a body core temperature elevation of 0.5 °C in the fetus, e) at an RF-EMF exposure that provokes a maximal local temperature elevation of 0.5°C in the fetus.

6.3. Discussion

It could be shown that in none of the pregnant models is the SAR_{WB} of the mother exceeded when exposed at the ICNIRP reference level. The $SAR_{WB,Mother}$ varies only slightly between the different models, which is not surprising since the whole body SAR is, to a first approximation, a function of the height which is the same for all models. A similar compliance with the ICNIRP basic restrictions could also be demonstrated for the whole body SAR of the fetuses. In general, the $SAR_{WB,Fetus}$ is 85% lower than the $SAR_{WB,Mother}$. Nevertheless, in the model in the earliest gestational stage (US 2, $9^{th.}$ week) the $SAR_{WB,Fetus}$ was exceeded. This may pose a potential risk for women in the early stages of pregnancy when they are maybe not aware of their condition. The results also indicate a decline of the $SAR_{WB,Fetus}$ during the pregnancy.

In contrast to this, no violation of the SAR_{10g} was found. It could be shown that the ICNIRP public reference level is very conservative and that much higher electrical field values are needed to induce a SAR_{10g} of 2W/kg in the fetus. The results indicate an increase of the SAR_{10g} maximum in the fetus during pregnancy.

Only a marginal body core temperature elevation occurs in the mother and the fetus for all models. Both the average temperature level and the maximal temperature in the fetus decline during pregnancy when exposed at the ICNIRP reference levels, with the sole exception of the US 2 model. This is worthy of note, since the $SAR_{WB,Foetus}$ is highest in this model. However, the core temperature in the fetus is "clamped" to the temperature in the mother [96] because of the circulating warmed blood and thus the potential increased heating of the fetus for the worst case scenario is restricted by the rather small elevation of the body core temperature of the mother.

Additional thermal simulations showed that a $SAR_{WB,Mother}$ of at least 4.52 W/kg is needed to elevate the body core temperature of the mother by 1°C. This result is higher than the 4 W/kg reported by the ICNIRP [20]. The factor for such an adverse temperature elevation in the mother is 56.5. However, such a high RF-EMF exposure would lead to an unacceptably high temperature elevation in the fetus. A $SAR_{WB,Fetus}$ of at least 1.63 W/kg is needed to elevate the body core temperature of the fetus by 0.5°C. This equals a factor of 23 for the worst case scenario (MRI 4) when exposed at the ICNIRP reference level.

The factor is further reduced to 13.2 if a maximal local temperature elevation of 0.5°C in the fetus is considered. A $SAR_{10g,Fetus}$ of 1.98 W/kg, which basically equals the ICNIRP SAR_{10g} limit of 2 W/kg for the trunk, is needed to produce such a local hot spot.

6.4. Conclusion

The ICNIRP does not specifically limit the SAR in the fetus. It could be confirmed that the current ICNIRP's basic restrictions for the SAR_{WB} may be violated in the early stages of gestation when applied to the fetus. On the other hand, the limitation of the SAR_{10g} is a very conservative restriction in terms of the overexposure of the fetus throughout the pregnancy.

However, the thermal modeling indicates that no adverse hazardous tissue heating occurs in the fetus with a large margin of safety, neither at the ICNIRP reference levels for the general public nor at the occupational exposure level.

Further research is needed to overcome the limited knowledge of the dielectric and thermal properties of fetal tissue.

7. RF-EMF induced Temperature Elevation in Children during Magnetic Resonance Imaging

7.1. Exposure Scenario

The number of children undergoing a brain MRI examination has been increasing steadily over the years [101]. Many of the children are unable to lie motionless for the duration of the examination and often feel uncomfortable due to the noise and limited space. Sedation of the children is therefore often inevitable [102]. This imposes an additional risk to the children, since they are unable to react to a possible hazardous tissue heating by the absorbed RF-EMF energy.

The ICNIRP guidelines (see chapter 0) are not applicable for patients undergoing MRI examinations. The ICNIRP has a special statement including exposure limits on the topic [96]. Furthermore, the product standard EN 60601-2-33 [31] also limits the RF-EMF exposure.

During MRI only some parts of the body are exposed, therefore not only the SAR_{WB} has to be monitored, but also the partial body SAR of the exposed body region and the head SAR. These limits are intended to restrict the local temperature elevation in the skin and also in delicate tissues such as the lens of the eye. In addition, the body core temperature elevation should be restricted.

The SAR_{WB} is limited to 2W/kg for the normal operation mode and 4 W/kg for the first level controlled mode. The limit for the average head SAR is the same (3.2 W/kg) for both modes. The SAR_{10g} is limited to 10 W/kg for the head/trunk and 20 W/kg for the extremities for the normal operational mode as well as for the first level controlled mode. These limitations can be violated during the second level controlled mode. However, for this mode ethical approval is required since the examination poses a significant risk for the patient. The standard does not provide any special regulations for children [31]. The limits of the aforementioned documents correspond to each

other, except the limit for the head SAR is slightly smaller (3 W/kg) in the ICNIRP statement.

These limits should ensure that the temperature values in Table 7-1 are not exceeded during MRI.

Operation mode	Elevation of the body-core temperature (°C)	Spatially localized temperature limit (°C)		
		Head	Trunk	Extremities
Normal	0.5	38	39	40
First level controlled	1	38	39	40
Second level controlled	>1	>38	>39	>40

Table 7-1: Temperature values for the body core temperature elevation as well as spatially localized temperature limits that should not be exceeded during a MRI examination.

Special attention should be paid to the eye, especially if positioned in a small local transmission coil. The temperature elevation should not exceed 1°C [31].

During examination in a volumetric whole body transmission coil, as used in this work, the SAR_{WB} alongside with average head SAR has to be monitored continuously, while no monitoring of the SAR10g is needed.

In the past, several studies have investigated the temperature elevation in adult heads and bodies during MRI (e.g. [92] [103] [104]). More recent studies have focused on the SAR and temperature computation in the fetus (e.g. [76] [34] [98]). However, no studies have been done to compute the SAR and the temperature elevation in children during a head MRI examination.

In this work, the intracorporal SAR distribution and the temperature elevation during MRI was investigated in three child models representing from five to fourteen years with static magnetic fields from 1.5 – 4 T (frequencies from 64 – 170 MHz). Three birdcage coils from a previous study were used for the simulations [76].

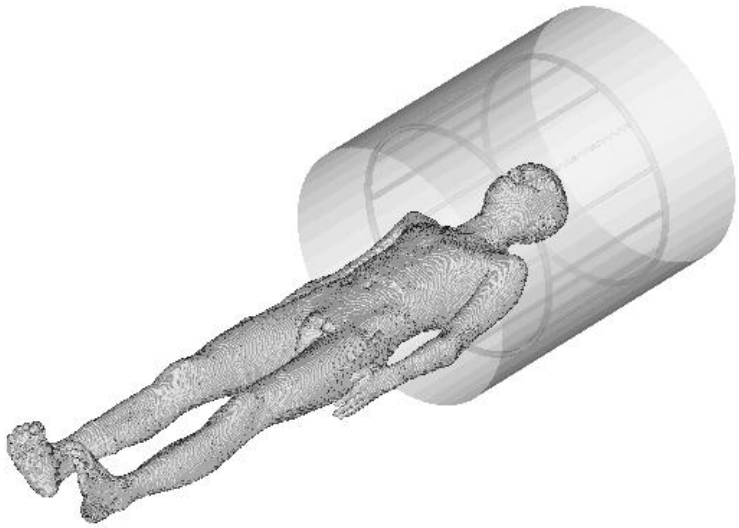

Figure 7-1: Child model Louis positioned inside the low-pass bird-cage resonator.

A low-pass resonator coil was used at 64 MHz and a band-pass resonator coil for the frequencies 127 and 170 MHz. The head of the models was placed in the isocenter of the transmission coil to simulate a brain MRI examination (see Figure 7-1)

The thermal parameters for the child models in Table 7-2 have been derived on the basis of the underlying assumptions of the thermal model (see chapter 2.1) and an ambient temperature of 24 °C (regulated by [96] [31]).

Name	MR (W)	P_{int} (W)	P_{ext} (W)	H_{ext} (W/(m²°C))	H_{int} (W/(m²°C))	S (m²)	BV (ml)
Louis	111.45	8.8	20.52	3.28	28.30	2.13	3583
Eartha	76.56	6.04	14.1	3.46	25.80	1.45	2341
Roberta	67.84	5.36	12.5	4.87	29.22	1	1411

Table 7-2: Thermal properties of the child models, including the basal metabolic rate (MR), the insensible water loss in the lungs (P_{int}) and on the skin (P_{ext}), the heat transfer coefficient in the lungs (H_{int}) and on the skin (H_{ext}), the body surface (S) and the blood volume (BV).

7.2. Results

The RF-EMFs generated inside the whole body coils are adequately homogeneous. Figure 7-2 shows the magnetic field strength along the cross axis of the whole body coil for all frequencies used.

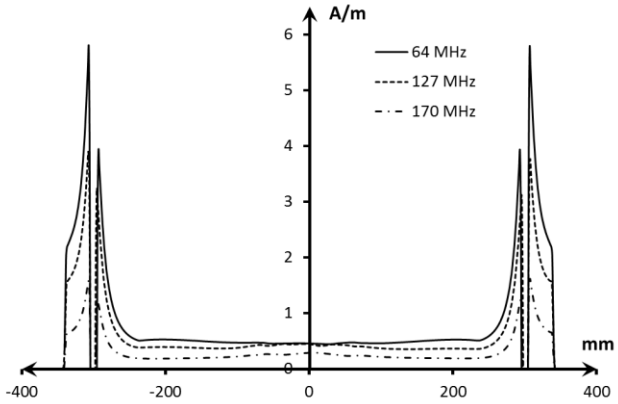

Figure 7-2: Absolute value of the magnetic field strength at the resonance frequencies along the cross axis of the whole body birdcage coils, scaled to an applied power of 1 W_{RMS}.

The SAR has been scaled to a transversal magnetic induction of 1 μT in the center of the coils. This allows the comparison of the RF-EMF exposure at different frequencies.

The scaling factor α was derived based on an equation proposed by Pediaditis et al. [76].

$$\alpha = \frac{SAR\left[B_{xy,ref}(0,0,0)\right]}{SAR\left[H_{xy}(0,0,0)\right]} = \frac{\frac{\sigma\eta^2 B_{xy,ref}^2}{\rho\mu^2}}{\frac{\sigma\eta^2 H_{xy}^2}{\rho}} = \frac{B_{xy,ref}^2}{\mu H_{xy}^2} \qquad 7.1$$

$B_{xy,ref}(0,0,0)$ is the transversal magnetic induction of 1 μT at the center of the coil, $H_{xy}(0,0,0)$ the calculated transversal magnetic field strength in this point, η the wave impedance, ρ the tissue density, σ the conductivity and μ the permeability.

Figure 7-4 shows the SAR distribution at a coronal and sagittal cross-section for the Roberta model at 64 MHz.

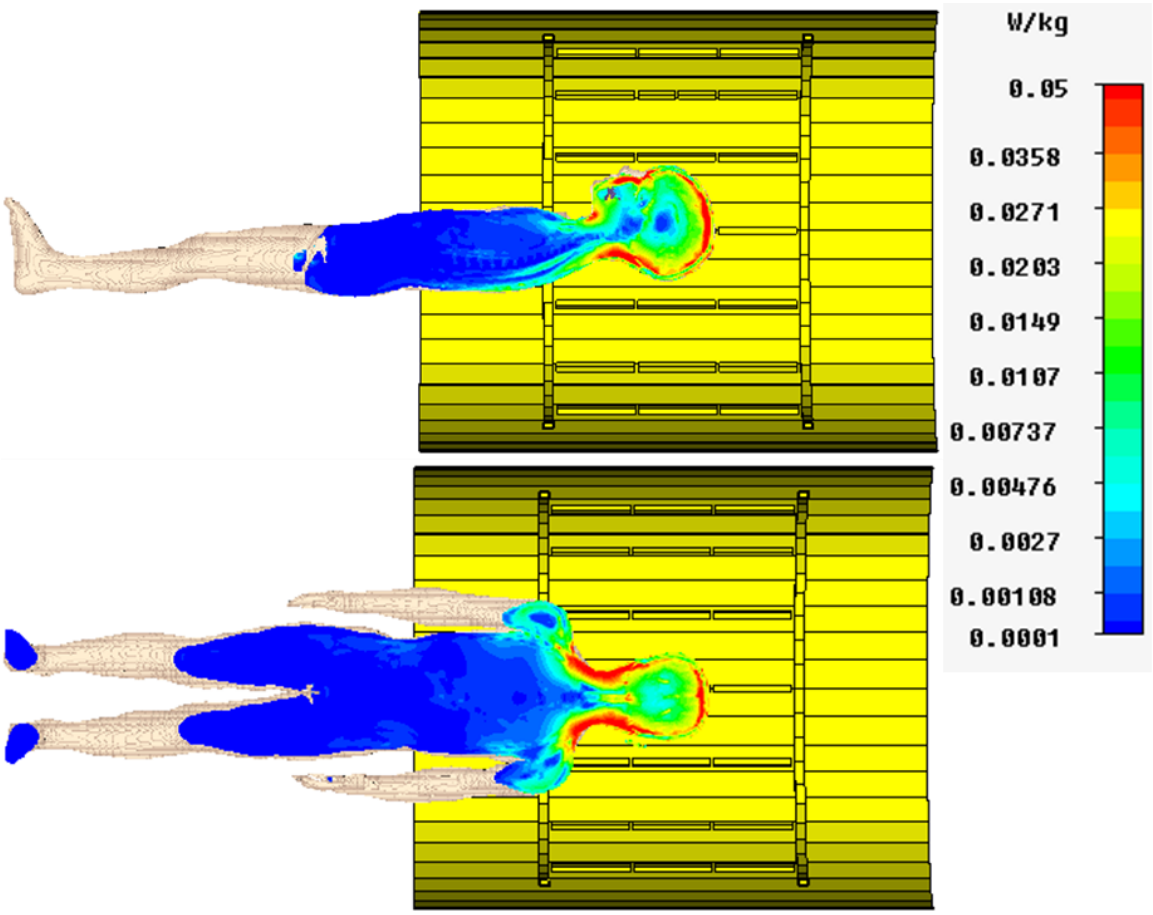

Figure 7-3: Sagittal and coronal cross section showing the SAR distribution in the Roberta model at 64 MHz. Scaled to a magnetic induction of 1 μT in the center of the birdcage coil.

Figure 7-4 shows the scaled SAR as a function of frequency for a magnetic induction of 1 μT at the center of the birdcage coil. A quadratic relation between the frequency and the SAR could be shown for all models. The quadratic regression coefficient was found to be better than 0.946. The SAR_{10g} maximum is located in the head for most frequencies and models. For three simulations (Eartha 64MHz and 170Mhz, Roberta 170MHz) the maximum SAR_{10g} was found in the thorax. The head SAR of the child models is, on average, 4.3 times smaller as than local SAR_{10g}. The same factor was found for the head SAR and whole body SAR ratio.

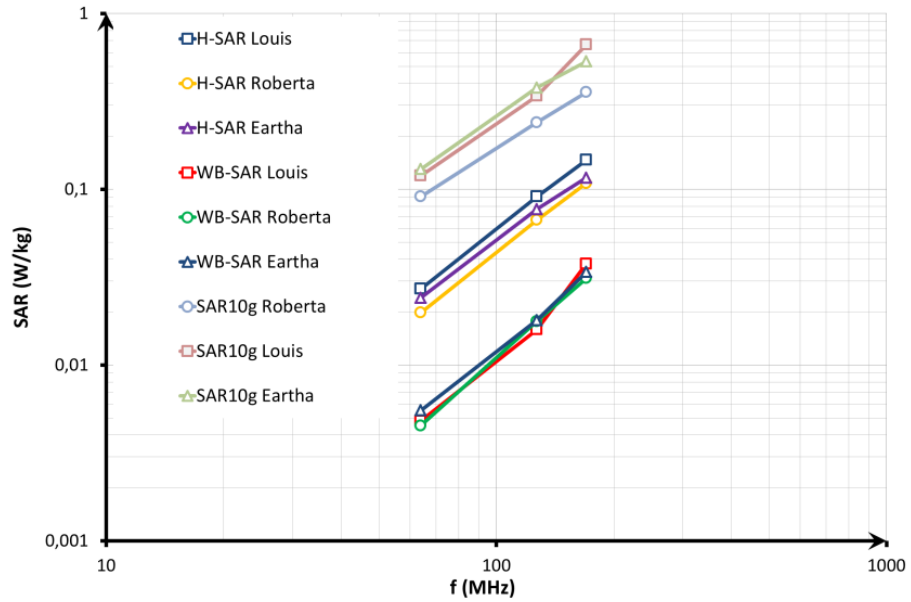

Figure 7-4: SAR values for different frequencies and a magnetic induction of 1μT at the center of the birdcage coil. H (Head), WB (Whole Body) and SAR10g (localized SAR averaged over 10 contiguous tissue).

The EN 60601-2-33 requires continuous monitoring of the whole body SAR and the head SAR for volumetric whole body birdcage coils. Therefore, thermal simulations with a scaled head SAR of 3.2 W/kg (normal and first level controlled mode), which is the worst case scenario for the chosen exposure scenario, were performed for all three models and frequencies used. In addition, thermal simulations for a SAR_{WB} of 2 W/kg (normal mode) and 4 W/kg (first level controlled mode) were performed. An exposure time of 60 min was used.

The limits of the body core temperature elevation (see Table 7-1) are not exceeded for any thermal simulation, neither during the normal operation mode nor the first level controlled mode. The maximal body core temperature is 0.22°C for a head SAR of 3.2 W/kg, 0.46°C for a SAR_{WB} of 2 W/kg and 0.9 °C for a SAR_{WB} of 4 W/kg.

Figure 7-5 shows the temperature distribution in the Roberta model after 60 min exposure at a head SAR of 3.2 W/kg. The biggest temperature rise occurs in the neck and the upper back. The temperature elevation in the brain is more moderate, despite the pronounced absorption (see Figure 7-4), due to its high blood perfusion, carrying away the heat.

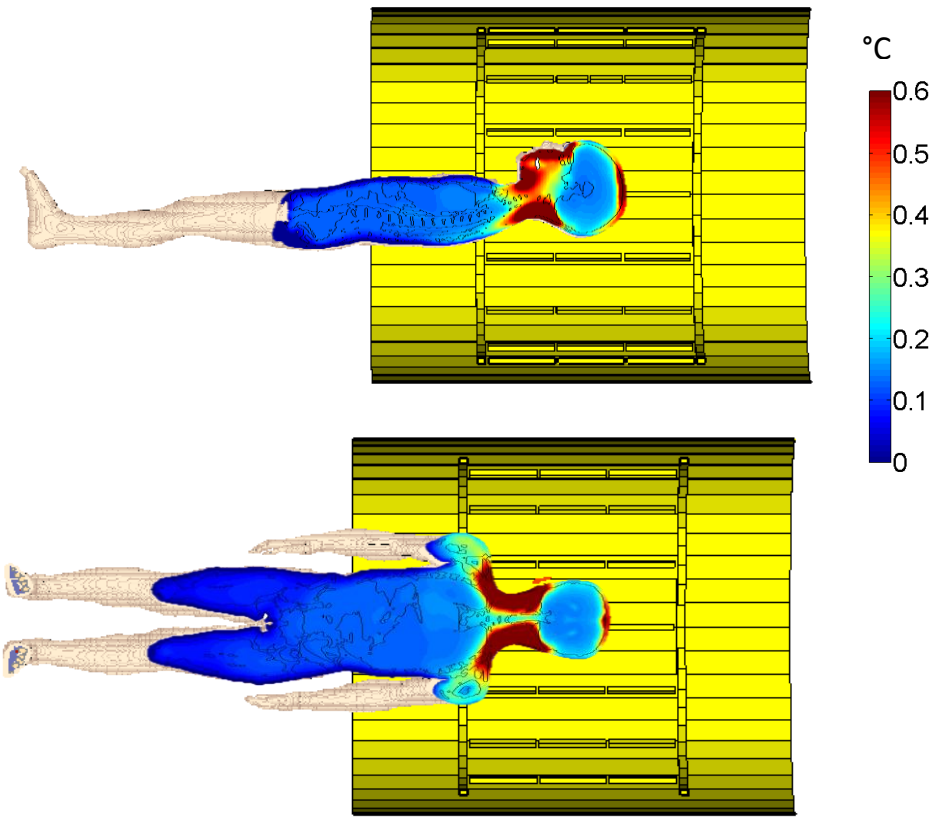

Figure 7-5: Temperature elevation in the Roberta model after 60 min exposed at a head SAR of 3.2 W/kg. After this time the local temperature limit of 38°C is exceeded in the head.

Table 7-3 summarizes the exposure times needed to exceed the local temperature limits described in Table 7-1 and the times needed to exceed the average temperature in the head by 0.5 °C, for a head SAR of 3.2 W/kg.

	Spatially localized temperature limit			**Average temperature in the head**
	Head	Trunk	Extremities	
Louis 170 MHz	42	>60 (37.94°C)	>60 (37.5°C)	>60 (0.38°C)
Louis 127 MHz	12	55	>60 (37.61°C)	33
Louis 64 MHz	11	22	>60 (38.25°C)	32
Eartha 170 MHz	11	39	>60 (38.87°C)	28
Eartha 127 MHz	12	>60 (38.94°C)	>60 (38.03°C)	20
Eartha 64 MHz	10	27	>60 (38.33°C)	28
Roberta 170 MHz	24	>60 (38°C)	>60 (37.36°C)	>60 (0.4°C)
Roberta 127 MHz	33	>60 (37.83°C)	>60 (37.43°C)	35
Roberta 64 MHz	60	>60 (37.64°C)	>60 (37.42°C)	>60 (0.4°C)

Table 7-3: Time needed (in minutes) to exceed the localized temperature limits for a head SAR of 3.2 W/kg. The limits are the same for the normal mode and the first level controlled mode: Head= 38°C, Trunk= 39°C, Extremities= 40°C. In addition, the time needed to elevate the average temperature in the head by 0.5°C was evaluated. The temperature value is added in brackets, if the limit is not exceeded after 60 min.

It was possible to show that the limitation of the local temperature elevation in the head imposes the biggest constraint with regard to the chosen exposure scenario. The time needed to exceed the temperature limits in the trunk is at least two times higher. No violation of the spatially localized temperature limit occurs in the extremities for the investigated exposure time. The temperature value after 60 min is added (in brackets) to the corresponding value in Table 7-3 if the temperature limit is not exceeded after 60 min. The temperature elevation in the eyes did not exceed 1°C and was at most 0.81°C.

The thermal steady state is not reached after 60 min. Nevertheless, the slope of the temperature elevation is small enough to allow an extrapolation of the results for even longer exposure times. Figure 7-6 shows the temperature elevation in the Roberta model at 64 MHz. Similar behavior was found in all models.

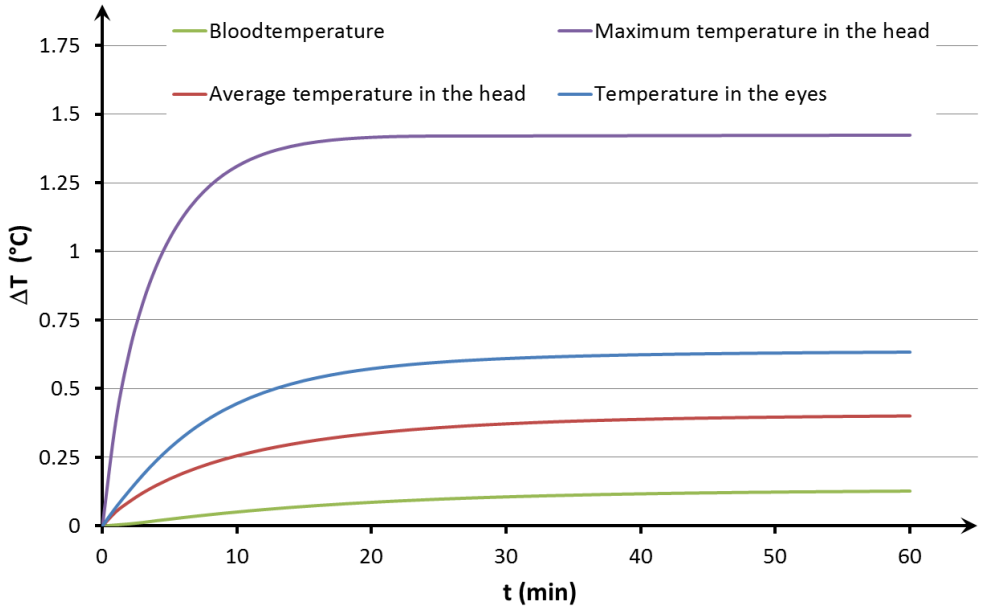

Figure 7-6: Temperature elevation in the Roberta model, exposed at 64 MHz and a head SAR of 3.2 W/kg.

The temperature elevations for the SAR_{WB} for 2 W/kg and 4 W/kg are much more pronounced. The permitted localized temperature limits are exceeded within minutes, especially in the head. Tables similar to Table 7-3 are included in the appendix (see A.4).

7.3. Discussion and conclusion

A magnetic resonance tomograph incorporates RF-EMF, switched gradient magnetic fields and static magnetic fields. However, in the context of tissue heating only the RF-EMF has to be considered and the other fields can be neglected.

The worst case scenario for a brain MRI could be reproduced by positioning the head of the child model right in the center of the birdcage coil. A quadratic increase of the SAR as a function of the resonance frequency was shown. This relation is evident from equation 7.1, but also reflects the quality of the birdcage coil and the homogeneity of the fields.

The thermal results show that the limitation of the body core temperature is conservative enough. The limits for the body core temperature elevation were not violated either for a head SAR of 3.2 W/kg, or for the much higher exposure at a SAR_{WB} of 2 W/kg and 4 W/kg. This is not surprising since only the head and the upper chest are exposed, while the rest of the body can act as heat sink, limiting the body core temperature elevation. The average temperature increase in the head exceeds 0.5°C in average after 30 min. However, the current standards [31] [96] do not regulate the average temperature in exposed regions. Another important finding of the simulations is that the temperature increase in the eyes did not exceed 1°C, when exposed at a head SAR of 3.2 W/kg.

The limiting factor with regard to the localized temperature is the temperature in the head, as is to be expected from the exposure scenario. The limit is exceeded for all frequencies and models, although the exposure time needed ranges from 10 min up to 60 min. It takes at least two times longer to violate the temperature limits in the trunk, while no violation of the localized temperature occurs.

These results raise the question as to whether the localized SAR_{10g} should be monitored during an MRI examination, especially since a brain MRI examination may last one hour or even longer [105]. At the present time only the SAR_{WB}, the partial body SAR and the head SAR have to be monitored if a whole body RF-EMF coil is used. Only the use of a local RF-EMF coil requires the continuous monitoring of the SAR_{10g}.

8. RF-EMF induced Temperature Elevation during Medical Diathermy

8.1. Exposure Scenario

Medical diathermy is a widely accepted therapeutic modality to treat muscle tissue and joints by targeted heating [106] [107]. Three frequencies have been assigned to this therapy method: 27.12 MHz (short wave), 433.92 MHz (decimeter-wave) and 2.45GHz (microwave). Short wave diathermy (SWD), in combination with different applicators, is used most.

Despite its widespread use only a few studies have evaluated the temperature in the human body during a SWD treatment. Their output is limited to in vivo measurements at a few points [108] [109]. Unintentional tissue heating outside treatment areas, especially in sensitive tissues such as the eye lens, the central nervous system (CNS) and the testicles was not addressed in these investigations. Leitgeb et al. [77] have shown that the exposure in such regions cannot be neglected. The ICNIRP guidelines (see chapter 0) are not applicable for patients undergoing SWD therapy. However, the product standard EN 60601-2-3 [30] limits the maximum output power of SWD devices to 500W.

This work presents thermal simulations for various SWD treatments. Two types of applicator, capacitive electrodes and an inductive applicator (Diplode) (see Figure 8-1), from a previous study [77] have been used. Treatment of the shoulder (capacitive electrodes), the hip (capacitive electrodes, Diplode) and the spine (capacitive electrodes, Diplode) has been investigated. The simulations were performed for a varying applicator to skin distance, ranging from direct contact to a maximal distance of 4 cm. The thermal simulations were conducted for the maximum recommended output power of 400W [110]. The male model Norman [21] was used for all simulations. The right arm of the model had to be bent for the hip treatment (see Figure 8-1).

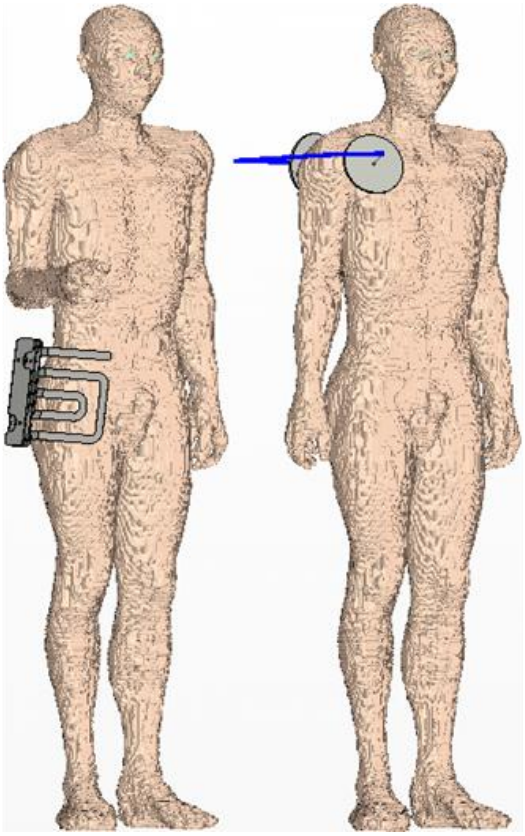

Figure 8-1: Two examples of a SWD treatment. Hip therapy, with an inductive applicator (left) and shoulder therapy, with capacitive electrodes (right). The adult male model NORMAN was used for the simulations **[77]**.

It is not possible to measure the RF-EMF energy induced temperature elevation during the treatment in the targeted tissue and the applied “dose”, as function of the output power and the exposure time, is therefore defined by the thermal perception of the patient. Schliephake defined four “dose-classes”, based on the individual thermal perception in the skin where the thermal sensors of humans are located (see Table 8-1) [111].

Dose	Sensation
I	Slightly below the thermal threshold
II	Onset of the thermal sensation
III	Pleasurable thermal sensation
IV	Strong but tolerable thermal sensation

Table 8-1: Dose-classes according to Schliephake [95].

The individual thermal perception varies considerably between body regions and patients [112] [113]. This is why it is not possible to link a “dose-class” to the subjective perception of the skin temperature.

However, it is well known that the temperature must rise to 38- 40°C in the targeted tissue with an exposure time of no longer than 20 min to achieve an optimal treatment effect [107]. Furthermore, the tissue temperature should not rise beyond 45°C as this may cause lesions by the denaturation of proteins.

Thermal simulations were therefore performed to determine the maximal temperature in the targeted tissue, joints and vulnerable regions for an exposure time of 20 min with the maximum recommended output power of 400 W. In addition, the temperature in all tissues was monitored continuously to detect any violations of the 45°C limit.

The following parameters for the thermal simulations have been derived on the basis of the underlying assumptions of the thermal model (see chapter 2.1) and an ambient temperature of 24°C. A blood temperature of 36.7 °C has been used for all simulations [3].

Thermal simulation parameters	
MR (W)	114.6
Pint (W)	9.05
Pext (W)	21.11
Hint (W/(m²K))	2.78
Hext (W/(m²K))	20.82
BV (ml)	5253

Table 8-2: Thermal simulation parameters of the NORMAN model, including the basal metabolic rate (MR), the insensible water loss (P), the heat transfer coefficient (H) and the blood volume (BV).

8.2. Results

Table 8-3 summarizes the temperature elevation for all simulations performed. The core temperature increase, represented by the blood temperature elevation, was at most 0.07°C. The maximal tolerable tissue temperature of 45°C was violated in the skin, for the capacitive electrodes in three simulations. This limit was not exceeded for any of the simulations during the exposure time when, the Diplode was used.

The optimal tissue temperature (38-40°C) is reached in the targeted tissue (muscle) for most simulations. The average temperature elevation in the muscle, however, is quite different for the two applicators used. Figure 8-2 shows the computed SAR and the temperature as functions of time for a hip treatment with a Diplode in direct contact and capacitive electrodes at a distance of 2 cm.

	Body region	ASD (cm)	ET (min)	ΔT_{Blood}	T_{Muscle}	T_{Skin}	T_{HJ}	T_{SJ}	ΔT_{Testis}	ΔT_{CNS}
Diplode	Hip	0	20	0.05	41.43	39.77	38.13		0.27	0.10
	Hip	20	20	0.02	39.71	38.20	37.45		0.14	0.06
	Hip	40	20	0.02	38.70	37.07	37.22		0.11	0.05
	Spine	0	20	0.04	38.44	38.47			0.08	0.46
	Spine	20	20	0.01	36.94	36.75			0.04	0.07
	Spine	40	20	0.02	36.92	36.75			0.003	0.02
Capacitive Electrodes	Hip	0	2	0.004	43.20	47.13	37.13		0.11	0.08
	Hip	20	5	0.01	40.84	46.07	37.16		0.08	0.06
	Hip	40	20	0.04	40.48	42.21	37.35		0.13	0.11
	Spine	0	20	0.07	42.66	43.20			0.09	0.52
	Spine	20	20	0.04	39.07	38.58			0.05	0.24
	Spine	40	20	0.02	37.89	37.45			0.04	0.17
	Shoulder	0	11	0.02	42.81	46.73		37.65	0.04	0.04
	Shoulder	20	20	0.01	38.53	38.82		37.26	0.05	0.05
	Shoulder	40	20	0.005	37.43	37.26		37.12	0.03	0.05

Table 8-3: Relative and absolute temperature elevation in the model Norman. Thermal simulations were performed for a varying applicator to skin distance (ASD) and a maximal exposure time (ET) of 20 min. All temperatures are given in °C: Blood temperature elevation (ΔT_{Blood}), maximal muscle temperature (T_{Muscle}), maximal skin temperature (T_{Skin}), maximal temperature in the hip joint (T_{HJ}), maximal temperature in the shoulder joint (T_{SJ}), maximal temperature elevation in the testis (ΔT_{Testis}) and the central nervous system (ΔT_{CNS}).

The absorption of the RF-EMF energy is considerably higher deep inside the body when the Diplode is used, with most of the energy concentrated in the muscle. The RF-EMF energy absorbed is concentrated mostly at the body surface (skin and fat) if capacitive electrodes are used.

This RF-EMF energy absorption pattern leads to a comparable temperature elevation in the targeted tissue. The temperature elevation in the muscle is almost uniform when a Diplode is used. In contrast, a mainly superficial temperature elevation in the skin and fat layer is found for the capacitive electrodes. The same behavior was found for all the simulations performed and is shown for two exemplary exposure setups in Figure 8-2.

The maximal temperature in the joints located in the irradiated body region is considerably smaller than in the muscle. The optimal temperature was only reached if a Diplode was used in direct contact to the hip.

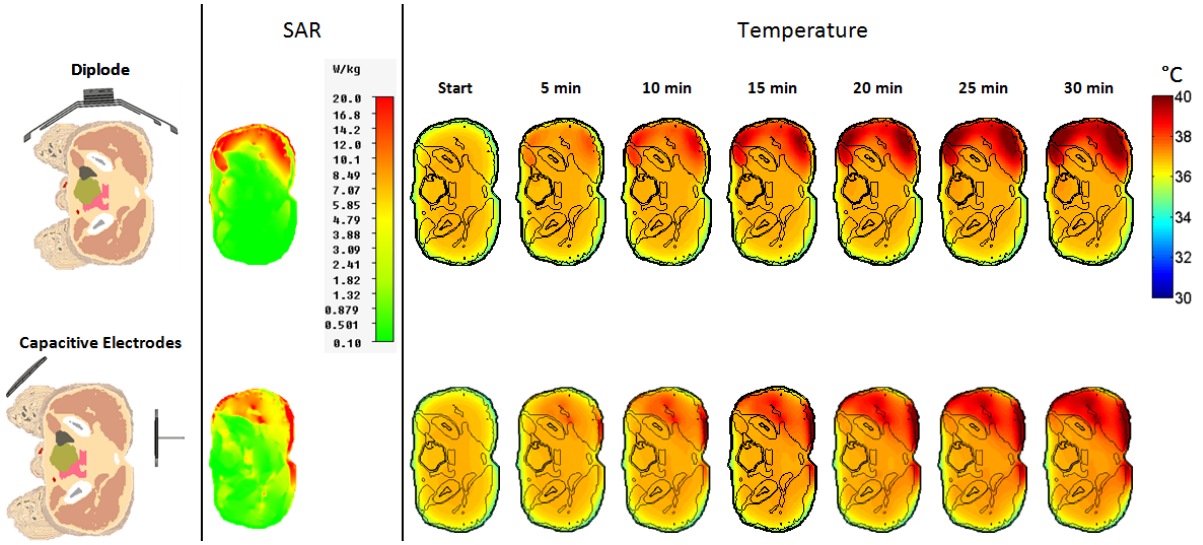

Figure 8-2: Diathermy treatment of the hip with a Diplode (direct contact) and capacitive electrodes (applicator skin distance 2cm). The SAR and the temperature as a function of time, are shown for the same transversal slice in the hip.

The temperature elevation in critical tissues such as the eye lens, the CNS and the testis was also monitored continuously for all simulations. The maximal temperature elevation in the testis ($\Delta T_{Testis,max}$=0.27°C) occurs during the hip treatment with the Diplode, while the maximum in the CNS ($\Delta T_{CNS,max}$=0.56°C) was found for the spinal treatment with the capacitive electrodes. The eye lens was not located in the exposed body region so that the maximal temperature is much lower than in the aforementioned tissues ($\Delta T_{Lens,max}$=0.09°C).

8.3. Discussion and conclusion

The pretested thermal simulations are a continuation of a previous study. Leitgeb et al. [77] used the same human model and diathermy applicators. In this study the exposed human model was limited to the irradiated body region. Whilst this is adequate for electromagnetic simulations, for thermal simulations it is important that the whole body is considered, otherwise the temperature elevation would be overestimated. This has been done in the thermal simulations presented.

Previous results have shown a considerable unintended exposure of vulnerable regions such as the CNS (the brain and the spinal cord) and the genital tract [77]. However, the thermal simulations performed demonstrate that the temperature in these tissues is not elevated beyond the known biological effect limit of 1°C [20], for a maximal exposure time of 20 min and the maximal recommended output power of 400W.

It was also possible to show that both applicators are able to elevate the temperature in the targeted tissue to an optimal temperature of at least 38°C [107]. The temperature elevation in this tissue is quite different, due to their unequal RF-EMF energy deposition. Whilst the inductive applicator was able to heat the whole irradiated muscle equally, for the capacitive electrodes a more superficial temperature elevation with a local hotspot in the skin and fat layer was found. This hotspot imposes a potential risk to the patient since the temperature is elevated within minutes beyond the 45°C which can be tolerated if capacitive electrodes are used in combination with a small applicator to skin distance. However, this risk is reduced by the fact that the local hotspot occurs in the skin, where the thermal sensors are located. The patient may therefore react in time to prevent burned tissue. The superficial heat load can also be reduced by a folded towel or cooling packs [107].

The thermal simulations presented show the potential of the implemented thermoregulatory model with respect to RF-EMF based therapeutic modalities, such as medical diathermy. The thermal model can be used to quantify the risk, especially for thermally vulnerable regions. Furthermore, the thermal model could be used to guide physicians for the efficient application of short-wave diathermy.

9. Summary

A multiphysical simulation process has been implemented in this work. The temperature elevation in arbitrary, high-resolution human models can be computed based on the absorbed RF-EMF energy.

The newly developed thermal model is based on the Pennes equation and has been extended by several thermoregulatory mechanisms. The local blood flow coefficient and metabolic rate is now adjusted on the basis of the local temperature. Moreover, the blood temperature is not kept constant but increases on the basis of the absorbed energy. Particular attention was also paid to the tissue/air interface at the skin and in the lungs. Now, not only the convection and radiation of heat is accounted for but also the insensible loss of water. Furthermore, a mathematical model describing the sweating has been incorporated into the thermal model.

The additional thermoregulatory mechanisms were implemented entirely in MATLAB® and Visual Basic©. The actual simulations, both electromagnetic as well as thermal, are performed in the software package CST Studio Suite 2011® and it was therefore necessary to develop a special software interface.

A database has been implemented providing the dielectric and thermal tissue properties for all models used, including children at different ages and pregnant women at different gestational stages, based on data from the literature.

Both the thermoregulatory model and the tissue database can easily be expanded and applied to new human models.

The accuracies of the electromagnetic solver used, of the ordinary BHT equation and of the fully implemented thermoregulatory model have been shown separately. An adequate compliance with data from the literature, standards and/or measurements has been demonstrated for each part.

The thermoregulatory model has been used for a variety of exposure scenarios. The temperature elevations in children and pregnant women, with a particular focus the fetus, exposed at the ICNIRP reference level have been evaluated. It could be shown that the temperature does not rise above the levels at which there are known effects, even if the basic restrictions are violated in children. In addition, it could be demon-

strated that the current ICNIRP limits protect the fetus adequately from a thermal point of view throughout the pregnancy, although no special limits have been defined. The thermal model has also been used to evaluate the temperature elevation during an RF-EMF based diagnostic modality. The temperatures in three children undergoing a head MRI at different resonance frequencies were computed and conclusions were drawn based on the current standards. Finally, the thermal model was applied to a therapeutic RF-EMF (medical diathermy) based modality. It was possible to compare the efficiency of different applicators with regard to the heating of the targeted tissue. In addition, the unintentional tissue heating of vulnerable regions was quantified.

The diversity of the exposure scenarios presented demonstrates the potential of the thermoregulatory model.

During the implementation process care was taken to keep the thermal model as structured and flexible as possible so that new or redefined mathematical models describing thermoregulatory mechanisms can easily be incorporated into the existing model.

Bibliography

[1] CST Studio Suite 2011, CST GmbH, Bad Nauheimer Strasse 19, D/64289, Darstadt, Deutschand, "www.cst.com," [Online].

[2] J. Hand, "Modelling the interaction of electromagnetic fields (10 MHz–10 GHz) with the human body: methods and applications," *Phys. Med. Biol.,* vol. 53, pp. 243-286.

[3] R. Schmidt, F. Lang and G. Thews, Physiologie des Menschen, Heidelberg: Springer Medizin Verlag, 2005.

[4] Gauer, Kramer and Jung, Physiologie des MEnschen, BAND 2: Energiehaushalt unf Termperturregulation, München - Berlin - Wien: Urban & Schwarzberg, 1971.

[5] S. Silbernagl and D. Agamemnon, Taschenatlas der Physiologie, Stuttgart: Georg Thieme Verlag, 2003.

[6] A. Shitzer and R. Eberhart, Heat Transfer in Medicine and Biology, New York: Plenum Press, 1985.

[7] P. Deetjen, E. Speckmann and J. Hescheler , Physiologie, München & Jena: Urban & Fischer, 2008.

[8] J. Aschoff and W. Rütger, "Kern und Schale im Wärmehaushalt des Menschen," *Die Naturwissenschaften,* vol. 45, pp. 477-485.

[9] I. Lamprecht and A. Zotin, Thermodynamics of Biological Processes, Berlin-New York: de Gruyer, 1978.

[10] A. Faller and M. Schünke, Der Körper des Menschen. Einführung in Bau und Funktion, Stuttgart: Thieme, 2004.

[11] J. Stolwijk, A MATHEMATICAL MODEL OF PHYSIOLOGICAL TEMPERATURE REGULATION IN MAN, Washington DC: NASA CR-1855 (NTIS N71-33401), 1971.

[12] W. Margaret , Johnston and L. Newburgh, "CALCULATION OF HEAT PRODUCTION FROM INSENSIBLE LOSS OF WEIGHT," *J. Clin. Invest.,* pp. 3:357-363, 1942.

[13] D. D. K. Karslake, The Stress of Hot Enviroment, London: Cambridge University Press, 1972.

[14] A. Hirata, T. Asano and O. Fujiwara, "FDTD analysis of human body-core temperature elevation due to RF far-field energy prescribed in the ICNIRP guidelines," *Phys. Med. Biol.,* pp. 52:5013-5023, 2007.

[15] ICNIRP, Exposure to High Frequency Electromagnetic Fields, Biological Effects and Health Consequences (100 kHz-300 GHz) Review of the Scientific Evidence and Health Consequences, Munich: ICRP, 2009.

[16] N. Leitgeb, Strahlen, Wellen, Felder. Ursachen und Auswirkungen auf Umwelt und Gesundheit, Wien: Springer-Verlag, 2000.

[17] ICNIRP, "ICNIRP STATEMENT ON THE “Guidelines for limiting exposure to time-varying electric, magnetic and electromagnetic fields (up to 300 GHz)"," *Health Physics,* vol. 97, pp. 257-259, 2009.

[18] H. Schwan, "Nonthermal cellular effects of electromagnetic fields AC-field induced ponderomotoric forces," *Br J Cancer Suppl,* pp. 220-224, 1982.

[19] J. C. Lin and Z. Wang, "Hearing of microwave pulses by humans and animals: effects, mechanism, and thresholds," *Health Phys,* pp. 621-628, 2007.

[20] ICNIRP, "Guidelines for limiting exposure to time-varying electric, magnetic and electromagnetic fields (up to 300 GHz)," *Health Phys.,* pp. 494-522, 1998.

[21] P. J. Dimbylow, "FDTD calculations of the whole-body averaged SAR in an anatomically realistic voxel model of the human body from 1 MHz to 1 GHz," *Phys. Med. Biol.,* vol. 42, pp. 479-490, 1997.

[22] B. Nielsen and M. Nielsen, "Influence of Passive and Active Heating on the Temperature Regulation of Man," *Acta Physiol. Scand.,* vol. 64, pp. 323-331, 1965.

[23] J. D'Andrea, E. Adair and J. de Lorge, "Behavioral and cognitive effects of microwave exposure," *Bioelectromagnetics Suppl,* vol. 6, pp. 39-62, 2003.

[24] F. Shellock and J. Crues, "Temperature, heart rate, and blood pressure changes associated with clinical imaging at 1.5 T," *Radiology,* pp. 259-262,

1987.

[25] ACGIH, "Threshold limit values for chemical substances and physical agents and biological indices," American Conference of Governmental Industrial Hygienists, Cincinnati, OH, 1996.

[26] R. L. Magin, R. P. Liburdy and B. Persson, Biological Effects and Safety Aspects of Nuclear Magnetic Resonance Imaging and Spectroscopy, New York: Ann. NY Acad. Sci 649, 1992.

[27] P. Bernardi, M. Cavagnaro, S. Pisa and E. Piuzzi, "Specific Absorption Rate and Temperature Elevation in a Subject Exposed in the Far-Field of Radio-Frequency Sources Operating in the 10–900-MHz Range," *IEEE Trans. Biomed. Eng.,* pp. 50:295-304, 2003.

[28] EN 45502-1, Active implantable medical devices - Part 1: General requirements for safety, marking and information to be provided by the manufacturer, 1997.

[29] EN 45502-2-1, Active implantable medical devices - Part 2-1: Particular requirements for active implantable medical devices intended to treat bradyarrhythmia (cardiac pacemakers), 2003.

[30] EN 60601-2-3, Medical Electrical Equipment part 2-3: Particular requirements for the safety of Short-Wave Therapy Equipment, 1993+ A1 1998.

[31] EN 60601-2-33, Medical electrical equipment - Part 2-33: Particular requirements for the basic safety and essential performance of magnetic resonance equipment for medical diagnosis, 2002 + A1 2005 + A2 2008.

[32] H. Pennes, "Analysis of Tissie and Atrial Blood Temperatures in the resting Human Foream," *J. Appl. Physiol.,* pp. 1:93-122, 1948.

[33] E. Wissle, "Pennes' 1948 paper revisited," *J Appl Physiol.,* vol. 85, pp. 35-41, 1998.

[34] J. Hand, E. Thomas, M. Rutherford and J. Hajnal, "Prediction of Specific Absorption Rate in Mother and Fetus Associated With MRI Examinations During Pregnancy," *Magn. Reson. Med.,* pp. 883-893, 2006.

[35] R. Roemer and T. Cetas, "Applications of Bioheat Transfer Simulations in Hyperthermia," *Cancer Res,* vol. 44, pp. 4788-4798, 1984.

[36] H. Arkin, L. X. Xu and K. R. Holmes, "Recent Developments in Modeling Heat Transfer in Blood Perfused Tissues," *IEEE T BIO-MED ENG,* vol. 41, pp. 97-

107, 1994.

[37] W. J. Minkowycz and E. M. Sparrow, Advances in Numerical Heat Transfer, Taylor and Francis, 2009.

[38] R. Spiegel, "A Review of Numerical Models for Predicting the Energy Deposition and Resultant Thermal Response of Humans Exposed to Electromagnetic Fields," *IEEE Transactions on Microwave Theory and Techniques,* vol. 8, pp. 730-746, 1984.

[39] D. Lee, Handbook of Physiology: Reactions to environmental agents, Bethesda: American Physiological Society, 1977.

[40] A. Chan, R. Sigelmann, A. Guy and J. Lehmann, "Calculation by the method of finite differences of the temperature distribution in layered tissues," *IEEE Trans Biomed. Eng.,* vol. 20, pp. 86-90, 1973.

[41] A. Guy, J. Lehmann and J. Stonebridge, "Therapeutic applications of electromagnetic power," *Proc. IEEE,* vol. 20, pp. 55-75, 1974.

[42] I. Chatterjee and O. Gandhi, "An Inhomogeneous Thermal Block Model of Man for the Electromagnetic Environment," *IEEE TRANSACTIONS ON BIOMEDICAL ENGINEERING,* vol. 11, pp. 707-715, 1983.

[43] M. Hoque and O. Gandhi, "Temperature distributions in the human leg for VLF-VHF exposures at the ANSI- recommended saefty levels," *IEEE Trans. Biomed. Eng.,* pp. 35:442-449.

[44] M. Hoque and O. P. Gandhi, "Temperature distributions in the human leg for VLF-VHF exposures at the ANSI- recommended saefty levels," *IEEE Trans. Biomed. Eng.,* pp. 35:442-449, 1988.

[45] A. Hirata, H. Sugiyama and M. Kojima, "Computational model for calculating body-core temperature elevation in rabbits due to whole-body exposure at 2.45 GHz," *Phys. Med. Biol.,* pp. 53:3391-3404, 2008.

[46] O. Fujiwara and A. Hirata, "Modeling time variation of blood temperature in a bioheat equation and its application to temperature analysis due to RF exposure," *Phys. Med. Biol.,* vol. 54, pp. 189-196, 2009.

[47] K. Diem, Documenta Geigy Scientific Tables, 7th ed. Basle: Ciba-Geigy, 1970.

[48] ICRP, ICRP Publication 89: Basic Anatomical and Physiological Data for Use in Radiological Protection: Reference Values, Oxford: Pergamon, 2003.

[49] W. Margaret , Johnston and L. Newburgh, "Calculation of heat production from insensible loss of weight," *J. Clin. Invest.,* pp. 21:357-363, 1942.

[50] A. Hirata, T. Asano and O. Fujiwara, "FDTD analysis of body-core temperature elevation in children and adults for whole-body exposure," *Phys. Med. Biol.,* pp. 5223-5238, 2008.

[51] CST GmbH, CST Studio Suite 2011 Advanced Topics 2011, [Online].

[52] T. Weiland, "Eine Methode zur Loesung der Maxwellschen Gleichungen fuer sechskomponentige Felder auf diskreter Basis," *AEUE,* vol. 31, pp. 116-120, 1977.

[53] T. Weiland, "A discretization method for the solution of Maxwell's equations for six-component Fields," *Electron. Commun. (AEU),* pp. 116-120, 1977.

[54] M. Clemens and T. Weiland, "DISCRETE ELECTROMAGNETISM WITH THE FINITE INTEGRATION METHOD," *PIER,* vol. 32, pp. 65-87, 2001.

[55] H. Spachmann, R. Schuhmann and T. Weiland, "Higher Order Spatial Operators for the Finite Integration Technique," *ACES Journal,* pp. 11-22, 2002.

[56] IEEE, "IEEE Standard for Safety Levels With Respect to Human Exposure to Radio Frequency Electromagnetic Fields, 3 Khz to 300 Ghz," p. STD 95.1 (New York: IEEE), 2005.

[57] R. P. Findlay and P. J. Dimbylow, "Calculated SAR distributions in a human voxel phantom due to the reflection of electromagnetic fields from a ground plane between 65 MHz and 2 GHz," *Phys. Med. Biol.,* pp. 53:2277-2289, 2008.

[58] B. Lazar, J. Pablo, T. Boubekeur, E. Angelini and I. Bloch, "Whole-Body Pregnant Woman Modeling By Digital Geometry Processing With Detailed Uterofetal Unit Based on Medical Images Unit," *IEEE T BIO-MED ENG,* no. 57, pp. 2346-2358, 2010.

[59] ICRP, "Human respiratory tract model for radiological protection ICRP," 1994.

[60] F. Goffinet, J. Carajol, S. Foidart, S. Alexander, S. Uzan, S. Subtil and G. Breart, "Is planned vaginal delivery for breech presentation at term still an option? Results of an observational prospective survey in France and Belgium," *AM J OBSTET GYNECOL,* vol. 194, pp. 1002-1011, 2006.

[61] L. Kalanithi, J. Illuzzi, V. Nossov, Y. Frisbaek, S. Abdel-Razeq, J. Copel and E. Norwitz, "Intrauterine growth restriction and placental location," *J ULTRAS*

MED, vol. 26, pp. 1481-1489, 2007.

[62] A. Christ, W. Kainz, E. Hahn and e. al., "The Virtual Family—development of surface-based anatomical models of two adults and two children for dosimetric simulations," *Phys. Med. Biol.,* pp. 55:23-38, 2010.

[63] H. P. Schwan, "Electrical propertiesof tissue and cell suspensions," *Adv in Biol Med Phys,* pp. 147-209, 1957.

[64] F. A. Duck, Physical Properties of Tissue. A comprehensive reference book, London: Academic Press Ltd., 1990 .

[65] C. Gabriel, S. Gabriel and E. Corthout, "The dielectric properties of biological tissues: I. Literature survey," *Phys. Med. Biol.,* pp. 41:2231-2249, 1996.

[66] S. Gabriel, R. Lau and C. Gabriel, "The dielectric properties of biological tissues: II. Measurements in the frequency range 10 Hz to 20 GHz," *Phys. Med. Biol.,* pp. 41:2251-2269, 1996.

[67] S. Gabriel, R. Lau and C. Gabriel, "The dielectric properties of biological tissues: III. Parametric models for the dielectric spectrum of tissues," *Phys. Med. Biol .,* pp. 41:2271-2293, 1996.

[68] A. Christ, M.-C. Gosselin and M. Christopoulou, "Age-dependent tissue-specific exposure of cell phone users," *Phys. Med. Biol.,* pp. 55:1767-1783, 2010.

[69] A. Peyman, C. Gabriel and E. H. Grant, "Variation of the dielectric properties of tissues with age: the effect on the values of SAR in children when exposed to walkie–talkie devices," *Phys. Med. Biol. ,* pp. 54:227-241, 2009.

[70] J. Wang, O. Fujiwara and S. Watanabe, "Approximation of aging effect on dielectric tissue properties for SAR assessment of mobile telephones," *IEEE Trans. Electromagn. Compat.,* pp. 48:408-413, 2006.

[71] K. Foster, J. Schepps, R. Stoy and H. Schwan, "Dielectric properties of brain tissue between 0.01 and 10 GHz," *Phys. Med. Biol.,* vol. 24, pp. 1177-1187, 1979.

[72] S. Gabriel, R. Lau and C. Gabriel, "The dielectric properties of biological tissues: III. Parametric models for the dielectric spectrum of tissues," *Phys. Med. Biol.,* pp. 41:2271-2293, 1996.

[73] "Changes in energy expenditure, anthropometry, and energy intake during the course of pregnancy and lactation in well-nourished Indian women," *Am J Clin*

Nutr, vol. 61, pp. 501-513, 1995.

[74] R. G. Gordon, R. B. Roemer and S. M. Horvath, "A Mathematical Model of the Human Temperature Regulatory System - Transient Cold Exposure Response," *IEEE Trans. Biomed. Eng.,* pp. 23: 434-444, 1976.

[75] A. Hirata, T. Asano and O. Fujiwara, "FDTD analysis of body-core temperature elevation in children and adults for whole-body exposure," *Phys. Med. Biol.,* pp. 53:5223-5238, 2008.

[76] R. Holland, "Pitfalls of Staircase Meshing," vol. 35, pp. 434-439, 1993.

[77] T. Samaras, A. Christ and N. Kuster, "Effects of geometry discretization aspects on the numerical solution of the bioheat transfer equation with the FDTD technique," *Phys. Med. Biol.,* vol. 51, pp. 221-229, 2006.

[78] R. Cech, Numerische EMF-Dosimetrie mit anatomischen Modellen, Graz: TU Graz, 2007.

[79] F. Gustrau, A. Bahr and S. Goltz, Berechnung feldinduzierter Ströme und Stromdichten in Modellen des menschlichen Körpers im Frequenzbereich 10 Hz bis 30 MHz, Germany: Wirtschaftsverlag N. W. Verlag für neue Wissenschaft, 2000.

[80] M. Pediaditis, N. Leitgeb and R. Cech, "RF-EMF exposure of fetus and mother during magnetic resonance imaging," *Phys. Med. Biol.,* vol. 53, pp. 7187-7195, 2008.

[81] N. Leitgeb, A. Omerspahic and F. Niedermayr, "Exposure 01 Non-Target Tissues in Medical Diathermy," *Bioelectromagnetics,* vol. 31, pp. 12-19, 2010.

[82] R. Findlay and P. Dimbylow, "Variations in calculated SAR with distance to the perfectly matched layer boundary for a human voxel model," *Phys. Med. Biol.,* vol. 51, pp. 411-415.

[83] EN 62311, "Assessment of electronic and electrical equipment related to human exposure restrictions for electromagnetic fields (0 Hz - 300 GHz)," 2008.

[84] A. Christ, A. Klingenböck, T. Samaras, C. Goiceanu and N. Kuster, "The dependence of electromagnetic far-field absorption on body tissue composition in the frequency range from 300 MHz to 6 GHz," *IEEE Trans. Microwave Theory Tech.,* vol. 54, pp. 2188-2195, 2006.

[85] E. Adair , S. A. Kelleher, G. W. Mack and T. S. Morocco, "Thermophysiological

responses of human volunteers during controlled whole body radio frequency exposure at 450 MHz," *Bioelectromagnetics,* pp. 19:232-245, 1998.

[86] T. Uusitupa, I. Laakso, S. Ilvonen and K. Nikoskinen, "SAR variation study from 300 to 5000 MHz for 15 voxel models including different postures," *Phys. Med. Biol.,* vol. 55, p. 1157–1176, 2010.

[87] J. Wang, O. Fujiwara, S. Kodera and S. Watanabe, "FDTD calculation of whole-body average SAR in adult and child models for frequencies from 30 MHz to 3 GHz," *Phys. Med. Biol.,* pp. 51:4119-4127, 2006.

[88] J. Wiart, A. Hadjem, M. Wong and I. Bloch, "Analysis of RF exposure in the head tissues of children and adults," *Phys. Med. Biol.,* pp. 53:3681-3695, 2008.

[89] A. Christ, M.-C. Gosselin, M. Christopoulou, S. Kühn and N. Kuster, "Age-dependent tissue-specific exposure of cell phone users," *Phys. Med. Biol.,* pp. 55:1767-1783, 2010.

[90] E. Conil, F. Hadjem, F. Lacroux, M. F. Wong and J. Wiart, "Variability analysis of SAR from 20 MHz to 2.4 GHz for different adult and child models using finite-difference time-domain," *Phys. Med. Biol.,* pp. 53:1511-1525, 2008.

[91] J. F. Bakker, M. M. Paulides, E. Neufeld, A. Christ, N. Kuster and G. C. van Rhoon, "Children and adults exposed to electromagnetic fields at the ICNIRP reference levels: theoretical assessment of the induced peak temperature increase," *Phys. Med. Biol.,* pp. 56:4967-4989, 2011.

[92] J. F. Bakker, M. M. Paulides, A. Christ, N. Kuster and G. C. van Rhoon, "Assessment of induced SAR in children exposed to electromagnetic plane waves between 10 MHz and 5.6 GHz," *Phys. Med. Biol.,* pp. 55:3115-3130, 2010.

[93] J. F. Bakker, M. M. Paulides, A. Christ, N. Kuster and G. C. van Rhoon, "Assessment of induced SAR in children exposed to electromagnetic plane waves between 10 MHz and 5.6 GHz," pp. 58:3115-3130, 2011.

[94] F. G. Shellock and J. V. Crues, "Temperature, heart rate, and blood pressure changes associated with clinical MR imaging at 1.5 T," *Radiology,* pp. 163:259-262, 1987.

[95] WHO, "http://www.who.int/peh-emf/research/rf_research_agenda_2006.pdf," 2006. [Online].

[96] WHO, 2010. [Online]. Available: http://whqlibdoc.who.int/publications/2010/9789241599948_eng.pdf.

[97] H. Kawai, T. Nagaoka, S. Watanabe, K. Saito, M. Takahashi and K. Ito, "Computational dosimetry in embryos exposed to electromagnetic plane waves over the frequency range of 10 MHz–1.5 GHz," *Phys. Med. Biol.,* vol. 55, pp. 1-11, 2010.

[98] ICNIRP, "ON MEDICAL MAGNETIC RESONANCE (MR) PROCEDURES: PROTECTION OF PATIENTS," *HEALTH PHYSICS,* no. 87, pp. 197-216, 2004.

[99] D. Wu, S. Shamsi and W. Kainz, "Evaluations of Specific Absorption Rate and Temperature Increase Within Pregnant and Temperature Increase Within Pregnant Imaging Birdcage Coils," *IEEE Trans. Microwave Theory Tech.,* vol. 54, pp. 4472-4478, 2006.

[100] S. Kikuchi, K. Saito, M. Takahashi and K. Ito, "Temperature elevation in the fetus from electromagnetic exposure during magnetic resonance imaging," *Phys. Med. Biol.,* vol. 55, pp. 2411-2426, 2010.

[101] P. Dimbylow, T. Nagaoka and G. Xu, "A comparison of foetal SAR in three sets of pregnant female models," *Phys. Med. Biol.,* vol. 54, pp. 2755-2767, 2009.

[102] T. Nagaoka, T. Togashi, K. Saito, M. Takahashi, K. Ito and S. Watanabe, "An anatomically realistic whole-body pregnant-woman model and specific absorption rates for pregnant-woman exposure to electromagnetic plane waves from 10 MHz to 2 GHz," *Phys. Med. Biol.,* vol. 52, pp. 6731-6745, 2007.

[103] G. Hedlund, "Neuroradiology of the central nervous system in childhood," *Neurol Clin,* vol. 4, pp. 965-981, 2002.

[104] Y. Bryan, T. Templeton, T. Nick, M. Szafran and A. Tung, "Brain Magnetic Resonance Imaging Increases Core Body Temperature in Sedant Children," *Anesth Analg,* vol. 102, pp. 1674-1679, 2006.

[105] C. Collins, W. Liu, J. Wang, R. Gruetter and T. Vaughan, "Temperature and SAR calculations for a human head within volume and surface coils at 64 and 300 MHz," *J. Magn. Reson. Imaging,* no. 5, pp. 650-656, 2004.

[106] C. Collins and M. Smith, "Signal-to-noise ratio and absorbed power as functions of main magnetic field strength, and definition of '90◦' RF pulse for the head in the birdcage coil," *Magn. Reson. Med.,* vol. 45, pp. 684-691, 2001.

[107] A. Machata, H. Willschke, B. Kabon, D. Prayer and P. Marhofer, "Effect of brain magnetic resonance imaging on body core temperature in sedant infants and children," *British Journal of Anasthesia,* vol. 102, pp. 385-389, 2009.

[108] J. DeLisa, B. Gans and N. Walsh, Physical medicine and rehabilitation: Principles and practice, Baltimore: Lippincott & Wilkins, 2004.

[109] K. Knight and D. Draper, Therapeutic modalities, Baltimore: Lippincott Williams and Wilkins, 2008.

[110] D. Draper, K. Knight, T. Fujiwara and J. Castke , "Temperature change in human muscle during and after pulsed short-wave diathermy," *J Orthopaed Sports Phys Ter,* vol. 29, pp. 13-22, 1999.

[111] C. Garrett, D. Draper and K. Knight, "Heat distribution in the lower leg from pulsed short-wave diathermy and ultrasound treatments," *J Athletic Training,* vol. 35, pp. 55-55, 2000.

[112] A. Omerspahic, Thermal diathermy and side-effects (in German), Graz: Graz Univ. Technol., 2007.

[113] W. Rentsch, Kurzwellen- und Mikrowellentherapie, Jena: VEB Gustav Fischer Verlag, 1985.

[114] D. Yarnitsky, E. Sprecher, R. Zaslansky and J. Hemli, "Heat pain thresholds: normative data and repeatability," *Pain,* vol. 60, pp. 329-332, 1995.

[115] V. Heldestad, J. Linder, L. Sellersjö and E. Nordh, "Reproducibility and influence of test modality order on thermal perception and thermal pain thresholds in quantitative sensory testing," *Clinical Neurophysiology,* vol. 121, pp. 1878-1886, 2010.

[116] ICRP/22/136/01, "Basic anatomical and physiological data for use in radiological protection: reference values," *REM Task Group ICRP Committee 2,* 2001.

[117] P. Van Den Berg, A. De Hoop, A. Segal and N. Praagman, "A Computational Model of the Electromagnetic Heating of Biological Tissue with Application to Hyperthermic Cancer Therapy," *IEEE Trans. Biomed. Eng.,* vol. 12, pp. 797-805, 1983.

[118] G. Van Leeuwen, J. Lagendijk, B. Van Leersum, A. Zwamborn, S. Hornsleth and A. Kotte, "Calculation of change in brain temperatures due to exposure to a

mobile phone," *Phys. Med. Biol.,* vol. 44, pp. 2367-2379, 1999.

[119] L. Williams and R. Leggett, "Reference values for resting blood flow to organs of man," *Clin. Phys. Physiol. Meas.,* vol. 10, pp. 187-217, 1989.

[120] E. Adair and D. Black, "Thermoregulatory Responses to RF Energy Absorbtion," *Bioelectromagnetics Suppl,* vol. 6, pp. 17-38, 2003.

[121] T. Uusitupa, I. Laakso, S. Ilvonen and K. Nikoskinen, "SAR variation study from 300 to 5000 MHz for 15 voxel models including different postures," *Phys. Med. Biol.,* pp. 55:1157-1176, 2010.

[122] ÖVE/ÖNORM E8850, Electric, magnetic and electromagnetic fields in the frequency range from 0 Hz to 300 GHz - Restrictions on human exposure, 2006.

[123] Council Recommendation, "On the limitation of exposure of the general public to electromagnetic fields (0 Hz to 300 GHz) 1999/519/EC," *Official Journal of the European Communities,* 1999.

[124] DIRECTIVE 2004/40/EC OF THE EUROPEAN PARLIAMENT AND OF THE Council, "On the minimum health and safety requirements regarding the exposure of workers to the risks arising from physical agents (electromagnetic fields) (18th individual Directive within the meaning of Article 16(1) of Directive 89/391/EEC)," *Official Journal of the European Union,* 2004.

Index of Figures

Index of Tables

Appendix

A.1 Matlab© Functions for the Thermal Model

thermoregulation

thermoregulation*(pfad,dateiname,pfad_frequenz,dateiname_frequenz,pfad_tissue,dateiname_tissue, Vb,BloodTemp_0,model,p_factor,sim_duration,step,efield)*

Passed values:

pfad	path of the selected project
dateiname	file name of the selected project
pfad_frequenz	path of the frequency data file
dateiname_frequenz	frequency data file used for the simulation
pfad_tissue	path of the voxel coordinate file
dateiname_tissue	file name of the voxel coordinate file
Vb	blood volume of the selected model
BloodTemp_0	blood temperature at the current time step
model	name of the chosen human model
p_factor	multiplication factor for the power distribution
sim_duration	total duration of the simulation
step	length of the used step, equals the variable *T_therm* in CST
efield	eField which is used for the thermal simulation

Table A.1-1: The GUI collects all the data needed for the thermoregulatory model.

initialization

[mps,ThermalTDSolver,ThermalSolver] = ***initalisierung****(dateiname,pfad)*

Passed values:

dateiname	file name of the selected project
pfad	project path

Returned values:

mps	handle for CST - commands
ThermalTDSolver	handle for the transient thermal solver
ThermalSolver	handle for the stationary thermal solver

Table A.1-2: Initialization of the variables and the CST- Project.

getMeshInfo

[nxyz,nxyzLines] = ***getMeshInfo****(dateiname,pfad)*

Passed values:

dateiname	file name of the selected project
pfad	Project path

Returned values:

nxyz	mesh size, read from *CST_GetHexMeshInfo*
xyzLines	grid lines, read from *CST_GetHexMesh*

Table A.1-3: Information regarding the used mesh is gathered.

getMeshDimension

[dVijk,dLxi, dLyj, dLzk] = ***getMeshDimension****(nxyz, nxyzLines)*

Passed values:

nxyz	mesh size, read from *CST_GetHexMeshInfo*
xyzLines	grid lines, read from *CST_GetHexMesh*

Returned values:

dVijk	volume of the dual grid
dLxi	length of the mesh cells in x-direction
dLyj	length of the mesh cells in y-direction
dLzk	length of the mesh cells in z-direction

Table A.1-4: The volume and the size of all mesh cells of the dual grid are gathered.

getVoxelInformation

*[Tissue_all,Tissue_0,xyz_min,xyz_max]= **getVoxelInformation**(mps, pfad, dateiname, pfad_frequenz, dateiname_frequenz,pfad_tissue,dateiname_tissue)*

Passed values:

mps	handle for CST - commands
dateiname	file name of the selected project
pfad	project path
dateiname_frequenz	frequency data file used for simulation
pfad_frequenz	path for the respective frequency data file
dateiname_tissue	file name of the voxel coordinate file
pfad_tissue	path of the voxel coordinate file

Returned values:

Tissue_all	coordinates of all tissues	
	Tissue	→ tissue name
	BloodFlow	→ perfusion coefficient of each voxel
	MetabolicRate	→ metabolic rate of all voxels
	Koordinaten	→ coordinates of the voxel
Tissue_0	coordinates of the perfused tissue	
	Tissue	→ tissue name
	BloodFlow	→ perfusion coefficient of each voxel
	MetabolicRate	→ metabolic rate of all voxels
	Koordinaten	→ coordinates of the voxel
xyz_min	minimum coordinates of the inserted voxel model	
xyz_max	maximum coordinates of the inserted voxel model	

Table A.1-5: The coordinates of all voxels are linked to the other parameters.

init_simulation

[BloodTemp_t,parameter_info,dt,repetition,p_factor,SW_gesamt] = ***init_simulation****(BloodTemp_0, sim_duration, step,p_factor)*

Passed values:

BloodTemp_0	blood temperature at the steady state
sim_duration	total duration of the simulation
step	length of the used step, equals the variable T_therm in CST
p_factor	multiplication factor for the power distribution

Returned values:

BloodTemp_t	blood temperature at the current time step
parameter_info	contains the current simulation parameters
dt	time step duration in seconds
repetition	total number of iterations
p_factor	multiplication factor for the power distribution
SW_gesamt	total heat loss by sweating

Table A.1-6: Simulation parameters are initialized.

g_voxel

[Gr_voxel] = ***G_voxel****(Tissue_all,model)*

Passed values:

Tissue_all	coordinates of all tissues	
	Tissue	→ tissue name
	BloodFlow	→ perfusion coefficient of each voxel
	MetabolicRate	→ metabolic rate of all voxels
	Koordinaten	→ coordinates of the voxel
model	name of the chosen model	

Returned values:

Gr_voxel		
	Tissue	→ tissue name
	VoxelNr	→ index of the voxels at the tissue/air interface
	AnzFlaeche	→ number of faces of the voxel bordering the air

Table A.1-7: Identification of all voxels on the air/tissue interface.

thermo_sim

thermo_sim*(ThermalTDSolver,ThermalSolver,mps,nr_sim,dateiname,pfad,*
BloodTemp_t,p_factor,dt,efield)

Passed values:

ThermalTDSolver	handle for the transient thermal Solver
ThermalSolver	handle for the stationary thermal Solver
mps	handle for CST - commands
nr_sim	Number of performed simulations
dateiname	file name
pfad	path to the project
BloodTemp_t	current blood temperature
p_factor	factor the calculated power distribution is multiplied by
dt	step size per iteration loop
efield	eField which is used for the thermal simulation

Table A.1-8: A transient thermal simulation is performed for one time step.

temperature

[Temperature_x] = ***temperature****(Tissue_0,sample_nr, Monitor, mps, dateiname,*
pfad)

Passed values:

Tissue_0	coordinates of the perfused tissue	
	Tissue	→ name of the tissue
	BloodFlow	→ coefficient of perfusion of each voxel
	MetabolicRate	→ metabolic rate of voxels
	Koordinaten	→ coordinates of voxels
sample_nr	sample number to be exported	
Monitor	monitor to be exported	
mps	handle for CST - commands	
Dateiname	file name of the project	
Pfad	path to the project	

Returned values:

Temperature_x	coordinates of the tissues supplied with blood and the temperature at that point for the selected time and monitor	
	Tissue	→ name of the tissue
	BloodFlow	→ coefficient of perfusion for each voxel
	MetabolicRate	→ metabolic rate of voxels
	Koordinaten	→ coordinates of voxels
	Temperature	→ temperature within the voxels

Table A.1-9: The temperature in the voxel center is exported to textfiles for each tissue.

blood_temperature

[BloodTemp_t] = ***blood_temperature*** *(BloodTemp_t, BloodTemp_0, Temperature_t, Temperature_0, Vb,dt)*

Passed values:

BloodTemp_t	blood temperature at the current time step
BloodTemp_0	blood temperature at the steady state
Temperature_t	output of the function *temperature(...)* for the current time step
	Tissue → tissue name
	BloodFlow → perfusion coefficient of each voxel
	MetabolicRate → metabolic rate of all voxels
	Koordinaten → coordinates of the voxel
	Temperature → temperature in the voxel center
Temperature_0	output of the function *temperature(...)* at the steady state
	Tissue → tissue name
	BloodFlow → perfusion coefficient of each voxel
	MetabolicRate → metabolic rate of all voxels
	Koordinaten → coordinates of the voxel
	Temperature → temperature in the voxel center
Vb	blood volume of the selected model
dt	time step duration in seconds

Returned values:

BloodTemp_t	calculated blood temperature

Table A.1-10: Computation of the blood temperature based on the absorbed RF-EMF energy.

data_presentation

[parameter_info] = ***data_presentation****(parameter_info,tElapsed,dt,i,repetition,BloodTemp_t, SW_gesamt)*

Passed values:

parameter_info	contains the current simulation parameters
tElapsed	duration of the last iteration
dt	step width of the last Iteration
i	Iteration counter
repetition	total number of iterations
BloodTemp_t	blood temperature at the current time step t
SW_gesamt	total heat loss by sweating

Returned values:

parameter_info	contains the current simulation parameters

Table A.1-11: Current simulation parameters are presented on the GUI, so that the user has an feed-back on the actual status of the simulation.

skin_perfusion

[Temperature_t] = ***skin_perfusion****(Temperature_t,Temperature_0,Gr_voxel)*

Passed values:

Temperature_0	output of the function *temperature(...)* at the steady state	
	Tissue	→ tissue name
	BloodFlow	→ perfusion coefficient of each voxel
	MetabolicRate	→ metabolic rate of all voxels
	Koordinaten	→ coordinates of the voxel
	Temperature	→ temperature in the voxel center
Temperature_t	output of the function *temperature(...)* for the current time step	
	Tissue	→ tissue name
	BloodFlow	→ perfusion coefficient of each voxel
	MetabolicRate	→ metabolic rate of all voxels
	Koordinaten	→ coordinates of the voxel
	Temperature	→ temperature in the voxel center
Gr_voxel		
	Tissue	→ tissue name
	VoxelNr	→ index in Temperature_t of the voxel, that border the air
	AnzFlaeche	→ number of faces of the voxel bordering the air

Returned values:

Temperature_t	output of the function *temperature(...)* for the current time	
	Tissue	→ tissue name
	BloodFlow	→ perfusion coefficient of each voxel
	MetabolicRate	→ metabolic rate of all voxels
	Koordinaten	→ coordinates of the voxel
	Temperature	→ temperature in the voxel center

Table A.1-12: The blood perfusion in voxels on the air/tissue interface is recomputed based on the temperature elevation in those voxels.

tissue_perfusion

[Temperature_t] = ***tissue_perfusion****(Temperature_t,Temperature_0)*

Passed values:

Temperature_0	output of the function *temperature(...)* at the steady state	
	Tissue	→ name of the tissue
	BloodFlow	→ coefficient of perfusion of each voxel
	MetabolicRate	→ metabolic rate of voxels
	Koordinaten	→ coordinates of voxel
	Temperature	→ temperature within the voxel center
Temperature_t	output of the function *temperature(...)* for the current time step	
	Tissue	→ name of the tissue
	BloodFlow	→ coefficient of perfusion of each voxel
	MetabolicRate	→ metabolic rate of voxel
	Koordinaten	→ coordinates of voxels
	Temperature	→ temperature within the voxel center

Returned values:

Temperature_t	output of the function *temperature(...)* for the current time step	
	Tissue	→ name of the tissue
	BloodFlow	→ coefficient of perfusion of each voxel
	MetabolicRate	→ metabolic rate of voxels
	Koordinaten	→ coordinates of voxels
	Temperature	→ temperature within the voxel center

Table A.113: The blood perfusion in all tissues, except for the skin, is recomputed based on the temperature elevation in the voxel.

metabolicRate_new

[Temperature_t] = ***metabolicRate_new****(Temperature_t,Temperature_0)*

Passed values:

Temperature_t	output of the function *temperature(...)* for the current time step	
	Tissue	→ tissue name
	BloodFlow	→ perfusion coefficient of each voxel
	MetabolicRate	→ metabolic rate of all voxels
	Koordinaten	→ coordinates of the voxel
	Temperature	→ temperature in the voxel center
Temperature_0	output of the function *temperature(...)* at the steady state and for the	
	Tissue	→ tissue name
	BloodFlow	→ perfusion coefficient of each voxel
	MetabolicRate	→ metabolic rate of all voxels
	Koordinaten	→ coordinates of the voxel
	Temperature	→ temperature in the voxel center

Returned values:

Temperature_t	output of the function *temperature(...)* for the current time step	
	Tissue	→ tissue name
	BloodFlow	→ perfusion coefficient of each voxel
	MetabolicRate	→ metabolic rate of all voxels
	Koordinaten	→ coordinates of the voxel
	Temperature	→ temperature in the voxel center

Table A.1-14: The metabolic rate of each voxel is computed based on the temperature elevation in the voxel.

sweat

*[Temperature_t,SW_gesamt]=**sweat**(Temperature_t,Temperature_0,Gr_voxel)*

Passed values:

Temperature_0	output of the function *temperature(...)* at the steady state	
	Tissue	→ tissue name
	BloodFlow	→ perfusion coefficient of each voxel
	MetabolicRate	→ metabolic rate of all voxels
	Koordinaten	→ coordinates of the voxel
	Temperature	→ temperature in the voxel center
Temperature_t	output of the function *temperature(...)* for the current time step	
	Tissue	→ tissue name
	BloodFlow	→ perfusion coefficient of each voxel
	MetabolicRate	→ metabolic rate of all voxels
	Koordinaten	→ coordinates of the voxel
	Temperature	→ temperature in the voxel center
Gr_voxel		
	Tissue	→ tissue name
	VoxelNr	→ index in Temperature_t of the voxel, that border the air
	AnzFlaeche	→ number of faces of the voxel bordering the air

Returned values:

Temperature_t	output of the function *temperature(...)* for the current time step	
	Tissue	→ tissue name
	BloodFlow	→ perfusion coefficient of each voxel
	MetabolicRate	→ metabolic rate of all voxels
	Koordinaten	→ coordinates of the voxel
	Temperature	→ temperature in the voxel center
SW_gesamt	total heat loss by sweating	

Table A.1-15: The sweating is computed for each voxel on the tissue/air interface.

saveMaterial

saveMaterial*(dLx,dLy,dLz, nxyz, nxyzLines, Temperature_t, Material, xyz_max, xyz_min, dateiname, pfad)*

Passed values:

dLxi	Length of the mesh cells in x-direction
dLyj	Length of the mesh cells in y-direction
dLzk	Length of the mesh cells in z-direction
nxyz	mesh size, read from *CST_GetHexMeshInfo*
xyzLines	grid lines, read from *CST_GetHexMesh*
Temperature_t	output of the function *temperature(...)* for the current time step
	Tissue → tissue name
	BloodFlow → perfusion coefficient of each voxel
	MetabolicRate → metabolic rate of all voxels
	Koordinaten → coordinates of the voxel
	Temperature → temperature in the voxel center
Material	selects the material properties to be written, works for *BloodFlow* and *MetabolicRate*
xyz_max	maximum coordinates of the inserted voxel model
xyz_min	minimum coordinates of the inserted voxel model
dateiname	file name of the selected project
pfad	Project path

Table A.1-16: The newly computed blood perfusion and metabolic rate is saved to the corresponding material file.

temperatur_monitor

temperatur_monitor*(ThermalTDSolver,ThermalSolver,pfad,dateiname,repetition)*

Passed values:

ThermalTDSolver	handle for the transient thermal Solver
ThermalSolver	handle for the stationary thermal Solver
pfad	path of the selected project
dateiname	file name of the selected project
repetition	total number of iterations

Table A.1-17: The temperature distribution in the simulation domain for each timestep is added to the CST project folder.

save_parameter_info

save_parameter_info*(parameter_info,pfad,dateiname)*

Passed values:

parameter_info	contains the current simulation
pfad	project path
dateiname	file name of the selected project

Table A.1-18: The blood temperature and the sweating rate are saved to a text file and included to the CST project folder.

A.2 Composition of the Human Models

Norman	Number of Voxels	Volume [dm^3]	Mass [kg]	Volume Fraction [%]
Adrenals	1786	1.43E-02	1.46E-02	2.16E-04
Bile	3432	2.75E-02	2.77E-02	4.16E-04
Bladder	5849	4.68E-02	4.87E-02	7.09E-04
Blood	109406	8.75E-01	9.28E-01	1.33E-02
Bone	742714	5.94E+00	1.18E+01	9.00E-02
Brain	165439	1.32E+00	1.37E+00	2.00E-02
Breast	3103	2.48E-02	2.53E-02	3.76E-04
CSF	39408	3.15E-01	3.18E-01	4.77E-03
Duodenum	11434	9.15E-02	9.55E-02	1.39E-03
Fat	1961432	1.57E+01	1.44E+01	2.38E-01
Gall Bladder	1243	9.94E-03	1.02E-02	1.51E-04
Heart Muscle	40441	3.24E-01	3.43E-01	4.90E-03
Humour	1377	1.10E-02	1.11E-02	1.67E-04
Hypothalamus	40	3.20E-04	3.36E-04	4.85E-06
Kidney	37191	2.98E-01	3.12E-01	4.51E-03
Lens	41	3.28E-04	3.53E-04	4.97E-06
Liver	208228	1.67E+00	1.75E+00	2.52E-02
Lower LI	34694	2.78E-01	2.90E-01	4.20E-03
Lunch	35802	2.86E-01	2.99E-01	4.34E-03
Lung	465638	3.73E+00	3.91E+00	5.64E-02
Muscle	3363332	2.69E+01	2.80E+01	4.08E-01
Esophagus	4962	3.97E-02	4.13E-02	6.01E-04
Pancreas	12147	9.72E-02	1.02E-01	1.47E-03
Prostate	1930	1.54E-02	1.61E-02	2.34E-04
Sclera	767	6.14E-03	6.60E-03	9.29E-05
Skin	525820	4.21E+00	4.63E+00	6.37E-02
Small Intestine	115947	9.28E-01	9.68E-01	1.40E-02
Spinal Cord	9449	7.56E-02	7.85E-02	1.14E-03
Spleen	19622	1.57E-01	1.65E-01	2.38E-03
Stomach	24752	1.98E-01	2.08E-01	3.00E-03
Tendon	156562	1.25E+00	1.46E+00	1.90E-02
Testis	4250	3.40E-02	3.55E-02	5.15E-04
Thymus	2340	1.87E-02	1.92E-02	2.84E-04
Thyroid	2334	1.87E-02	1.96E-02	2.83E-04
Trabec Bone	76781	6.14E-01	1.18E+00	9.30E-03
Upper LI	51666	4.13E-01	4.32E-01	6.26E-03
Urine	12067	9.65E-02	9.89E-02	1.46E-03

Table A.2-1: Number of voxels, volume, mass and relative fraction for each tissue of the model NORMAN.

Louis	Number of Voxels	Volume [dm3]	Mass [kg]	Volume Fraction [%]
Adrenal Gland	278	2.22E-03	2.28E-03	4.70E-05
Artery	28661	2.29E-01	2.43E-01	4.85E-03
Bladder	23811	1.90E-01	1.98E-01	4.03E-03
Blood Vessel	1702	1.36E-02	1.44E-02	2.88E-04
Bone	89568	7.17E-01	1.43E+00	1.52E-02
Brain Grey Matter	95488	7.64E-01	7.94E-01	1.62E-02
Brain White Matter	62319	4.99E-01	5.20E-01	1.05E-02
Bronchi	1082	8.66E-03	9.20E-03	1.83E-04
Bronchi Lumen	50	3.98E-04	5.17E-07	8.42E-06
Calcaneus Left	3129	2.50E-02	4.98E-02	5.29E-04
Calcaneus Marrow Left	4156	3.32E-02	3.41E-02	7.03E-04
Calcaneus Marrow Right	4831	3.86E-02	3.97E-02	8.17E-04
Calcaneus Right	3153	2.52E-02	5.02E-02	5.33E-04
Capitatum Left	239	1.91E-03	3.80E-03	4.04E-05
Capitatum Marrow Right	30	2.41E-04	2.48E-04	5.10E-06
Capitatum Marrow Right	33	2.66E-04	2.73E-04	5.63E-06
Capitatum Right	258	2.06E-03	4.11E-03	4.36E-05
Cartilage	9759	7.81E-02	8.59E-02	1.65E-03
Cerebellum	20018	1.60E-01	1.67E-01	3.39E-03
Cerebrospinal Fluid	27260	2.18E-01	2.20E-01	4.61E-03
Commissura Anterior	6	4.60E-05	4.80E-05	9.73E-07
Commissura Posterior	2	1.80E-05	1.88E-05	3.81E-07
Connective Tissue	165598	1.32E+00	1.34E+00	2.80E-02
Cornea	73	5.84E-04	6.28E-04	1.24E-05
Diaphragm	35557	2.84E-01	2.96E-01	6.02E-03
Distalis I Left	49	3.95E-04	7.86E-04	8.35E-06
Distalis I Right	66	5.30E-04	1.05E-03	1.12E-05
Distalis II Left	14	1.13E-04	2.25E-04	2.39E-06
Distalis II Right	17	1.35E-04	2.69E-04	2.86E-06
Distalis III Left	24	1.89E-04	3.76E-04	4.00E-06
Distalis III Right	28	2.22E-04	4.42E-04	4.70E-06
Distalis IV Left	18	1.45E-04	2.89E-04	3.07E-06
Distalis IV Right	30	2.43E-04	4.84E-04	5.14E-06
Distalis V Left	9	7.10E-05	1.41E-04	1.50E-06
Distalis V Right	12	9.90E-05	1.97E-04	2.09E-06
Ear Cartilage	1428	1.14E-02	1.26E-02	2.42E-04
Ear Skin	1364	1.09E-02	1.20E-02	2.31E-04
Epididymis	271	2.17E-03	2.28E-03	4.59E-05
Esophagus	2142	1.71E-02	1.78E-02	3.62E-04
Esophagus Lumen	478	3.82E-03	4.01E-03	8.09E-05
Eye Lens	32	2.58E-04	2.81E-04	5.46E-06
Eye Sclera	461	3.69E-03	3.81E-03	7.80E-05
Eye Vitreous Humor	1260	1.01E-02	1.02E-02	2.13E-04
Fat	795783	6.37E+00	5.83E+00	1.35E-01
Femur Left	17712	1.42E-01	2.82E-01	3.00E-03
Femur Marrow Left	37972	3.04E-01	3.12E-01	6.42E-03
Femur Marrow Right	37508	3.00E-01	3.08E-01	6.35E-03
Femur Right	17716	1.42E-01	2.82E-01	3.00E-03

Louis (continuation)	Number of Voxels	Volume [dm3]	Mass [kg]	Volume Fraction [%]
Fibula Left	3931	3.14E-02	6.26E-02	6.65E-04
Fibula Marrow Left	2293	1.83E-02	1.88E-02	3.88E-04
Fibula Marrow Right	2351	1.88E-02	1.93E-02	3.98E-04
Fibula Right	4025	3.22E-02	6.41E-02	6.81E-04
Gallbladder	2535	2.03E-02	2.08E-02	4.29E-04
Hamatum Left	231	1.85E-03	3.68E-03	3.91E-05
Hamatum Marrow Left	3	2.70E-05	2.77E-05	5.71E-07
Hamatum Marrow Right	1	4.00E-06	4.11E-06	8.46E-08
Hamatum Right	234	1.87E-03	3.73E-03	3.96E-05
Heart Lumen	23434	1.87E-01	1.99E-01	3.96E-03
Heart muscle	51378	4.11E-01	4.36E-01	8.69E-03
Hippocampus	392	3.14E-03	3.26E-03	6.63E-05
Humerus Left	6200	4.96E-02	9.87E-02	1.05E-03
Humerus Marrow Left	5678	4.54E-02	4.67E-02	9.61E-04
Humerus Marrow Right	6376	5.10E-02	5.24E-02	1.08E-03
Humerus Right	6431	5.15E-02	1.02E-01	1.09E-03
Hypophysis	84	6.71E-04	7.15E-04	1.42E-05
Hypothalamus	60	4.76E-04	5.00E-04	1.01E-05
Intervertebral disc	15778	1.26E-01	1.39E-01	2.67E-03
Kidney cortex	16443	1.32E-01	1.38E-01	2.78E-03
Kidney medulla	15800	1.26E-01	1.32E-01	2.67E-03
Large intestine	41963	3.36E-01	3.50E-01	7.10E-03
Large intestine Lumen	18953	1.52E-01	1.58E-01	3.21E-03
Larynx	649	5.20E-03	5.62E-03	1.10E-04
Liver	150302	1.20E+00	1.26E+00	2.54E-02
Lunatum Left	161	1.29E-03	2.57E-03	2.73E-05
Lunatum Marrow Left	0	0.00E+00	0.00E+00	0.00E+00
Lunatum Marrow Right	0	1.00E-06	1.03E-06	2.11E-08
Lunatum Right	148	1.19E-03	2.36E-03	2.51E-05
Lung	228970	1.83E+00	1.20E+00	3.87E-02
Mandible	2683	2.15E-02	4.27E-02	4.54E-04
Marrow red	38510	3.08E-01	3.16E-01	6.52E-03
Media II Left	35	2.80E-04	5.57E-04	5.92E-06
Media II Right	43	3.43E-04	6.83E-04	7.25E-06
Media III Left	48	3.81E-04	7.58E-04	8.06E-06
Media III Right	82	6.57E-04	1.31E-03	1.39E-05
Media IV Left	33	2.61E-04	5.19E-04	5.52E-06
Media IV Right	78	6.26E-04	1.25E-03	1.32E-05
Media V Left	17	1.35E-04	2.69E-04	2.86E-06
Media V Right	25	1.96E-04	3.90E-04	4.15E-06
Medulla oblongata	613	4.90E-03	5.09E-03	1.04E-04
Meniscus	3089	2.47E-02	2.71E-02	5.23E-04
Metacarpus I Left	363	2.90E-03	5.77E-03	6.13E-05
Metacarpus I Marrow Left	4	2.90E-05	2.98E-05	6.13E-07
Metacarpus I Marrow Right	23	1.84E-04	1.89E-04	3.89E-06
Metacarpus I Right	382	3.06E-03	6.08E-03	6.47E-05
Metacarpus II Left	426	3.41E-03	6.78E-03	7.21E-05
Metacarpus II Marrow Left	30	2.40E-04	2.46E-04	5.08E-06

Louis (continuation)	Number of Voxels	Volume [dm3]	Mass [kg]	Volume Fraction [%]
Metacarpus II Marrow Right	45	3.60E-04	3.70E-04	7.61E-06
Metacarpus II Right	447	3.57E-03	7.11E-03	7.55E-05
Metacarpus III Left	380	3.04E-03	6.05E-03	6.43E-05
Metacarpus III Marrow Left	24	1.89E-04	1.94E-04	4.00E-06
Metacarpus III Marrow Right	23	1.81E-04	1.86E-04	3.83E-06
Metacarpus III Right	372	2.98E-03	5.93E-03	6.30E-05
Metacarpus IV Left	281	2.25E-03	4.48E-03	4.76E-05
Metacarpus IV Marrow Left	7	5.60E-05	5.75E-05	1.18E-06
Metacarpus IV Marrow Right	1	1.10E-05	1.13E-05	2.33E-07
Metacarpus IV Right	288	2.30E-03	4.58E-03	4.86E-05
Metacarpus V Left	216	1.73E-03	3.44E-03	3.66E-05
Metacarpus V Right	230	1.84E-03	3.67E-03	3.90E-05
Midbrain	1809	1.45E-02	1.50E-02	3.06E-04
Mucosa	2314	1.85E-02	1.94E-02	3.91E-04
Muscle	2387364	1.91E+01	1.99E+01	4.04E-01
Nerve	3653	2.92E-02	3.03E-02	6.18E-04
Pancreas	3144	2.52E-02	2.63E-02	5.32E-04
Patella	4288	3.43E-02	6.83E-02	7.26E-04
Penis	4479	3.58E-02	3.80E-02	7.58E-04
Pharynx	618	4.95E-03	6.43E-06	1.05E-04
Pinealbody	35	2.80E-04	2.94E-04	5.92E-06
Pisiforme Left	47	3.72E-04	7.40E-04	7.87E-06
Pisiforme Right	42	3.38E-04	6.73E-04	7.15E-06
Pons	1605	1.28E-02	1.33E-02	2.72E-04
Prostate	1376	1.10E-02	1.15E-02	2.33E-04
Proximalis I Left	126	1.01E-03	2.01E-03	2.14E-05
Proximalis I Right	148	1.19E-03	2.36E-03	2.51E-05
Proximalis II Left	135	1.08E-03	2.15E-03	2.29E-05
Proximalis II Right	181	1.45E-03	2.88E-03	3.06E-05
Proximalis III Left	133	1.07E-03	2.12E-03	2.25E-05
Proximalis III Right	175	1.40E-03	2.79E-03	2.96E-05
Proximalis IV Left	116	9.30E-04	1.85E-03	1.97E-05
Proximalis IV Right	162	1.29E-03	2.58E-03	2.74E-05
Proximalis V Left	75	5.99E-04	1.19E-03	1.27E-05
Proximalis V Right	101	8.07E-04	1.61E-03	1.71E-05
Radius Left	2700	2.16E-02	4.30E-02	4.57E-04
Radius Marrow Left	1161	9.29E-03	9.54E-03	1.96E-04
Radius Marrow Right	881	7.05E-03	7.24E-03	1.49E-04
Radius Right	2512	2.01E-02	4.00E-02	4.25E-04
SAT	449361	3.59E+00	3.29E+00	7.60E-02
Scaphoideum Left	193	1.54E-03	3.07E-03	3.26E-05
Scaphoideum Right	194	1.56E-03	3.09E-03	3.29E-05
Skin	460625	3.69E+00	4.05E+00	7.79E-02
Skull	43488	3.48E-01	6.92E-01	7.36E-03
Small intestine	37553	3.00E-01	3.14E-01	6.35E-03
Small intestine Lumen	10400	8.32E-02	8.69E-02	1.76E-03
Spinal Cord	2620	2.10E-02	2.18E-02	4.43E-04

Louis (continuation)	Number of Voxels	Volume [dm3]	Mass [kg]	Volume Fraction [%]
Spleen	38812	3.10E-01	3.27E-01	6.57E-03
Stomach	15374	1.23E-01	1.29E-01	2.60E-03
Stomach Lumen	18314	1.47E-01	1.54E-01	3.10E-03
Talus Left	2027	1.62E-02	3.23E-02	3.43E-04
Talus Marrow Left	1939	1.55E-02	1.59E-02	3.28E-04
Talus Marrow Right	1999	1.60E-02	1.64E-02	3.38E-04
Talus Right	2128	1.70E-02	3.39E-02	3.60E-04
Teeth	1083	8.66E-03	1.87E-02	1.83E-04
Tendon Ligament	25536	2.04E-01	2.27E-01	4.32E-03
Testis	2076	1.66E-02	1.73E-02	3.51E-04
Thalamus	1386	1.11E-02	1.15E-02	2.35E-04
Thymus	2955	2.36E-02	2.43E-02	5.00E-04
Thyroid Gland	890	7.12E-03	7.47E-03	1.51E-04
Tibia Left	13957	1.12E-01	2.22E-01	2.36E-03
Tibia Marrow Left	26006	2.08E-01	2.14E-01	4.40E-03
Tibia Marrow Right	27372	2.19E-01	2.25E-01	4.63E-03
Tibia Right	13360	1.07E-01	2.13E-01	2.26E-03
Tongue	8720	6.98E-02	7.26E-02	1.48E-03
Trachea	1478	1.18E-02	1.30E-02	2.50E-04
Trachea Lumen	856	6.85E-03	8.90E-06	1.45E-04
Trapezium Left	166	1.33E-03	2.64E-03	2.81E-05
Trapezium Marrow Left	0	3.00E-06	3.08E-06	6.34E-08
Trapezium Right	162	1.30E-03	2.58E-03	2.74E-05
Trapezoideum Left	85	6.79E-04	1.35E-03	1.44E-05
Trapezoideum Right	90	7.23E-04	1.44E-03	1.53E-05
Triquetrum Left	131	1.05E-03	2.09E-03	2.22E-05
Triquetrum Right	122	9.73E-04	1.94E-03	2.06E-05
Ulna Left	2571	2.06E-02	4.09E-02	4.35E-04
Ulna Marrow Left	1176	9.41E-03	9.66E-03	1.99E-04
Ulna Marrow Right	1460	1.17E-02	1.20E-02	2.47E-04
Ulna Right	2930	2.34E-02	4.66E-02	4.96E-04
Ureter Urethra	1157	9.26E-03	9.77E-03	1.96E-04
Vein	42275	3.38E-01	3.58E-01	7.15E-03
Vertebrae	74491	5.96E-01	1.19E+00	1.26E-02

Table A.2-2: Number of voxels, volume, mass and relative fraction for each tissue of the model Louis.

Roberta	Number of Voxels	Volume [dm3]	Mass [kg]	Volume Fraction [%]
Artery	5381	4.30E-02	4.56E-02	2.57E-03
Bladder	3283	2.63E-02	2.73E-02	1.57E-03
Bone	52862	4.23E-01	8.42E-01	2.53E-02
Brain Grey Matter	81112	6.49E-01	6.74E-01	3.88E-02
Brain White Matter	38976	3.12E-01	3.25E-01	1.86E-02
Cartilage	1776	1.42E-02	1.56E-02	8.49E-04
Cerebellum	15164	1.21E-01	1.26E-01	7.25E-03
Cerebrospinal Fluid	22455	1.80E-01	1.81E-01	1.07E-02
Connective Tissue	67052	5.36E-01	5.43E-01	3.20E-02
Cornea	10	8.10E-05	8.72E-05	4.84E-06
Ear Cartilage	561	4.49E-03	4.94E-03	2.68E-04
Ear Skin	865	6.92E-03	7.61E-03	4.13E-04
Esophagus	317	2.54E-03	2.64E-03	1.51E-04
Esophagus Lumen	120	9.57E-04	1.00E-03	5.72E-05
Eye Lens	23	1.82E-04	1.98E-04	1.09E-05
Eye Sclera	166	1.33E-03	1.37E-03	7.93E-05
Eye Vitreous Humor	1159	9.27E-03	9.35E-03	5.54E-04
Fat	319390	2.56E+00	2.34E+00	1.53E-01
Gallbladder	777	6.22E-03	6.38E-03	3.72E-04
Heart Lumen	16409	1.31E-01	1.39E-01	7.84E-03
Heart Muscle	6505	5.20E-02	5.52E-02	3.11E-03
Hippocampus	324	2.59E-03	2.69E-03	1.55E-04
Hypophysis	27	2.18E-04	2.32E-04	1.30E-05
Hypothalamus	79	6.29E-04	6.60E-04	3.76E-05
Intervertebral Disc	2827	2.26E-02	2.49E-02	1.35E-03
Kidney Cortex	8078	6.46E-02	6.78E-02	3.86E-03
Kidney Medulla	4602	3.68E-02	3.84E-02	2.20E-03
Large Intestine	15790	1.26E-01	1.32E-01	7.55E-03
Large Intestine Lumen	14111	1.13E-01	1.18E-01	6.74E-03
Liver	58778	4.70E-01	4.94E-01	2.81E-02
Lung	101615	8.13E-01	5.32E-01	4.86E-02
Mandible	2128	1.70E-02	3.39E-02	1.02E-03
Marrow Red	10249	8.20E-02	8.42E-02	4.90E-03
Medulla Oblongata	573	4.59E-03	4.76E-03	2.74E-04
Meniscus	438	3.50E-03	3.85E-03	2.09E-04
Midbrain	2475	1.98E-02	2.06E-02	1.18E-03
Mucosa	267	2.14E-03	2.24E-03	1.28E-04
Muscle	689161	5.51E+00	5.74E+00	3.29E-01
Nerve	5534	4.43E-02	4.60E-02	2.64E-03
Ovary	168	1.35E-03	1.41E-03	8.04E-05
Pancreas	1024	8.19E-03	8.56E-03	4.89E-04
Patella	328	2.62E-03	5.22E-03	1.57E-04
Pharynx	62	4.99E-04	6.49E-07	2.98E-05
Pinealbody	15	1.22E-04	1.28E-04	7.29E-06
SAT	209009	1.67E+00	1.53E+00	9.99E-02
Skin	165614	1.32E+00	1.46E+00	7.91E-02
Skull	42397	3.39E-01	6.75E-01	2.03E-02
Small Intestine	17682	1.41E-01	1.48E-01	8.45E-03

Roberta (continuation)	Number of Voxels	Volume [dm3]	Mass [kg]	Volume Fraction [%]
Small Intestine Lumen	26338	2.11E-01	2.20E-01	1.26E-02
Spinal Cord	1830	1.46E-02	1.52E-02	8.74E-04
Spleen	10693	8.55E-02	9.02E-02	5.11E-03
Stomach	8098	6.48E-02	6.80E-02	3.87E-03
Stomach Lumen	3107	2.49E-02	2.61E-02	1.48E-03
Teeth	150	1.20E-03	2.60E-03	7.19E-05
Tendon Ligament	4857	3.89E-02	4.31E-02	2.32E-03
Thalamus	1554	1.24E-02	1.29E-02	7.43E-04
Thymus	2525	2.02E-02	2.07E-02	1.21E-03
Tongue	3677	2.94E-02	3.06E-02	1.76E-03
Trachea	268	2.14E-03	2.36E-03	1.28E-04
Trachea Lumen	176	1.41E-03	1.83E-06	8.39E-05
Ureter Urethra	40	3.18E-04	3.36E-04	1.90E-05
Uterus	679	5.43E-03	5.71E-03	3.24E-04
Vagina	458	3.66E-03	3.82E-03	2.19E-04
Vein	4919	3.94E-02	4.17E-02	2.35E-03
Vertebrae	33401	2.67E-01	5.32E-01	1.60E-02

Table A.2-3: Number of voxels, volume, mass and relative fraction for each tissue of the model Roberta.

Thelonious	Number of Voxels	Volume [dm3]	Mass [kg]	Volume Fraction [%]
Adrenal Gland	353	2.83E-03	2.90E-03	1.54E-04
Artery	8798	7.04E-02	7.46E-02	3.84E-03
Bladder	3706	2.96E-02	3.08E-02	1.62E-03
Blood Vessel	1062	8.50E-03	9.01E-03	4.64E-04
Bone	89914	7.19E-01	1.43E+00	3.93E-02
Brain Grey Matter	87018	6.96E-01	7.23E-01	3.80E-02
Brain White Matter	45970	3.68E-01	3.84E-01	2.01E-02
Bronchi	110	8.81E-04	9.37E-04	4.81E-05
Bronchi Lumen	92	7.35E-04	9.56E-07	4.01E-05
Cartilage	5403	4.32E-02	4.75E-02	2.36E-03
Cerebellum	18973	1.52E-01	1.58E-01	8.28E-03
Cerebrospinal Fluid	25295	2.02E-01	2.04E-01	1.10E-02
Commissura Anterior	5	4.00E-05	4.17E-05	2.18E-06
Commissura Posterior	1	6.00E-06	6.26E-06	3.27E-07
Connective Tissue	35475	2.84E-01	2.87E-01	1.55E-02
Cornea	37	2.95E-04	3.17E-04	1.61E-05
Diaphragm	13850	1.11E-01	1.15E-01	6.05E-03
Ear Cartilage	473	3.78E-03	4.16E-03	2.07E-04
Ear Skin	1436	1.15E-02	1.26E-02	6.27E-04
Epididymis	92	7.37E-04	7.74E-04	4.02E-05
Esophagus	852	6.82E-03	7.09E-03	3.72E-04
Esophagus Lumen	452	3.61E-03	3.79E-03	1.97E-04
Eye Lens	37	2.92E-04	3.18E-04	1.59E-05
Eye Sclera	488	3.91E-03	4.03E-03	2.13E-04
Eye Vitreous Humor	1153	9.22E-03	9.30E-03	5.03E-04
Fat	256936	2.06E+00	1.88E+00	1.12E-01
Gallbladder	949	7.59E-03	7.79E-03	4.14E-04
Heart Lumen	945	7.56E-03	8.02E-03	4.13E-04
Heart Muscle	29323	2.35E-01	2.49E-01	1.28E-02
Hippocampus	248	1.98E-03	2.06E-03	1.08E-04
Hypophysis	35	2.79E-04	2.97E-04	1.52E-05
Hypothalamus	80	6.43E-04	6.75E-04	3.51E-05
Intervertebral_disc	9112	7.29E-02	8.02E-02	3.98E-03
Kidney Cortex	10031	8.02E-02	8.42E-02	4.38E-03
Kidney Medulla	6294	5.03E-02	5.26E-02	2.75E-03
Large Intestine	26925	2.15E-01	2.25E-01	1.18E-02
Large Intestine Lumen	60021	4.80E-01	5.01E-01	2.62E-02
Larynx	11	9.10E-05	9.85E-05	4.97E-06
Liver	69766	5.58E-01	5.86E-01	3.05E-02
Lung	113467	9.08E-01	5.95E-01	4.95E-02
Mandible	2081	1.66E-02	3.31E-02	9.08E-04
Marrow Red	13566	1.09E-01	1.11E-01	5.92E-03
Medulla Oblongata	659	5.27E-03	5.48E-03	2.88E-04
Meniscus	1098	8.78E-03	9.64E-03	4.79E-04
Midbrain	947	7.58E-03	7.87E-03	4.13E-04
Mucosa	386	3.09E-03	3.24E-03	1.68E-04
Muscle	755175	6.04E+00	6.29E+00	3.30E-01
Nerve	7297	5.84E-02	6.06E-02	3.19E-03

Thelonious (continuation)	Number of Voxels	Volume [dm3]	Mass [kg]	Volume Fraction [%]
Pancreas	1326	1.06E-02	1.11E-02	5.79E-04
Patella	386	3.09E-03	6.14E-03	1.68E-04
Penis	1141	9.13E-03	9.67E-03	4.98E-04
Pharynx	179	1.43E-03	1.86E-06	7.82E-05
Pinealbody	35	2.76E-04	2.90E-04	1.51E-05
Pons	1532	1.23E-02	1.27E-02	6.69E-04
Prostate	436	3.49E-03	3.64E-03	1.90E-04
SAT	235032	1.88E+00	1.72E+00	1.03E-01
Skin	167825	1.34E+00	1.48E+00	7.33E-02
Skull	32824	2.63E-01	5.23E-01	1.43E-02
Small Intestine	7101	5.68E-02	5.93E-02	3.10E-03
Small Intestine Lumen	2759	2.21E-02	2.30E-02	1.20E-03
Spinal Cord	3232	2.59E-02	2.68E-02	1.41E-03
Spleen	15345	1.23E-01	1.29E-01	6.70E-03
Stomach	16967	1.36E-01	1.43E-01	7.41E-03
Stomach Lumen	16334	1.31E-01	1.37E-01	7.13E-03
Teeth	711	5.69E-03	1.23E-02	3.10E-04
Tendon Ligament	25683	2.05E-01	2.28E-01	1.12E-02
Testis	384	3.07E-03	3.20E-03	1.67E-04
Thalamus	2351	1.88E-02	1.95E-02	1.03E-03
Thymus	3616	2.89E-02	2.97E-02	1.58E-03
Tongue	4692	3.75E-02	3.91E-02	2.05E-03
Trachea	507	4.05E-03	4.46E-03	2.21E-04
Trachea Lumen	762	6.10E-03	7.92E-06	3.33E-04
Ureter Urethra	106	8.46E-04	8.93E-04	4.62E-05
Vein	7846	6.28E-02	6.65E-02	3.43E-03
Vertebrae	28988	2.32E-01	4.61E-01	1.27E-02

Table A.2-4: Number of voxels, volume, mass and relative fraction for each tissue of the model Thelonious.

Eartha	Number of Voxels	Volume [dm3]	Mass [kg]	Volume Fraction [%]
Adrenal Gland	288	2.30E-03	2.36E-03	8.02E-05
Artery	12028	9.62E-02	1.02E-01	3.36E-03
Bladder	17235	1.38E-01	1.43E-01	4.81E-03
Blood Vessel	745	5.96E-03	6.32E-03	2.08E-04
Bone	135819	1.09E+00	2.16E+00	3.79E-02
Brain Grey Matter	92284	7.38E-01	7.67E-01	2.57E-02
Brain White Matter	42150	3.37E-01	3.52E-01	1.18E-02
Bronchi	903	7.22E-03	7.67E-03	2.52E-04
Bronchi Lumen	90	7.16E-04	9.31E-07	2.50E-05
Cartilage	16041	1.28E-01	1.41E-01	4.48E-03
Cerebellum	17625	1.41E-01	1.47E-01	4.92E-03
Cerebrospinal Fluid	35047	2.80E-01	2.82E-01	9.78E-03
Commissura Anterior	7	5.50E-05	5.74E-05	1.92E-06
Commissura Posterior	2	1.50E-05	1.56E-05	5.23E-07
Connective Tissue	137439	1.10E+00	1.11E+00	3.83E-02
Cornea	39	3.11E-04	3.35E-04	1.08E-05
Diaphragm	11725	9.38E-02	9.76E-02	3.27E-03
Ear Cartilage	1145	9.16E-03	1.01E-02	3.20E-04
Ear Skin	1261	1.01E-02	1.11E-02	3.52E-04
Esophagus	1265	1.01E-02	1.05E-02	3.53E-04
Esophagus Lumen	392	3.14E-03	3.29E-03	1.09E-04
Eye Lens	72	5.79E-04	6.31E-04	2.02E-05
Eye Sclera	151	1.21E-03	1.25E-03	4.21E-05
Eye Vitreous Humor	1286	1.03E-02	1.04E-02	3.59E-04
Fat	556618	4.45E+00	4.08E+00	1.55E-01
Gallbladder	617	4.94E-03	5.07E-03	1.72E-04
Heart Lumen	25635	2.05E-01	2.17E-01	7.15E-03
Heart Muscle	18334	1.47E-01	1.55E-01	5.11E-03
Hippocampus	390	3.12E-03	3.24E-03	1.09E-04
Hypophysis	15	1.21E-04	1.29E-04	4.22E-06
Hypothalamus	105	8.40E-04	8.82E-04	2.93E-05
Intervertebral Disc	8355	6.68E-02	7.35E-02	2.33E-03
Kidney Cortex	11871	9.50E-02	9.96E-02	3.31E-03
Kidney Medulla	8017	6.41E-02	6.70E-02	2.24E-03
Large Intestine	30630	2.45E-01	2.56E-01	8.55E-03
Large Intestine Lumen	5593	4.47E-02	4.67E-02	1.56E-03
Larynx	84	6.70E-04	7.25E-04	2.34E-05
Liver	85575	6.85E-01	7.19E-01	2.39E-02
Lung	146209	1.17E+00	7.66E-01	4.08E-02
Mandible	4919	3.93E-02	7.83E-02	1.37E-03
Marrow Red	51375	4.11E-01	4.22E-01	1.43E-02
Medulla Oblongata	688	5.50E-03	5.71E-03	1.92E-04
Meniscus	1593	1.27E-02	1.40E-02	4.44E-04
Midbrain	990	7.92E-03	8.23E-03	2.76E-04
Mucosa	2040	1.63E-02	1.71E-02	5.69E-04
Muscle	1248909	9.99E+00	1.04E+01	3.48E-01
Nerve	996	7.97E-03	8.27E-03	2.78E-04
Ovary	464	3.71E-03	3.89E-03	1.29E-04

Eartha (continuation)	Number of Voxels	Volume [dm3]	Mass [kg]	Volume Fraction [%]
Pancreas	2418	1.93E-02	2.02E-02	6.75E-04
Patella	916	7.33E-03	1.46E-02	2.56E-04
Pharynx	614	4.91E-03	6.39E-06	1.71E-04
Pinealbody	29	2.35E-04	2.47E-04	8.20E-06
Pons	1740	1.39E-02	1.45E-02	4.86E-04
SAT	430562	3.44E+00	3.16E+00	1.20E-01
Skin	197885	1.58E+00	1.74E+00	5.52E-02
Skull	51749	4.14E-01	8.24E-01	1.44E-02
Small Intestine	32005	2.56E-01	2.67E-01	8.93E-03
Small Intestine Lumen	3898	3.12E-02	3.26E-02	1.09E-03
Spinal cord	1802	1.44E-02	1.50E-02	5.03E-04
Spleen	17857	1.43E-01	1.51E-01	4.98E-03
Stomach	14489	1.16E-01	1.22E-01	4.04E-03
Stomach Lumen	9392	7.51E-02	7.89E-02	2.62E-03
Teeth	1184	9.47E-03	2.05E-02	3.30E-04
Tendon Ligament	8191	6.55E-02	7.27E-02	2.29E-03
Thalamus	4040	3.23E-02	3.36E-02	1.13E-03
Thymus	1087	8.70E-03	8.92E-03	3.03E-04
Tongue	7912	6.33E-02	6.59E-02	2.21E-03
Trachea	871	6.97E-03	7.67E-03	2.43E-04
Trachea Lumen	393	3.15E-03	4.09E-06	1.10E-04
Ureter Urethra	315	2.52E-03	2.66E-03	8.77E-05
Uterus	2545	2.04E-02	2.14E-02	7.10E-04
Vagina	1397	1.12E-02	1.17E-02	3.90E-04
Vein	13573	1.09E-01	1.15E-01	3.79E-03
Vertebrae	36882	2.95E-01	5.87E-01	1.03E-02

Table A.2-5: Number of voxels, volume, mass and relative fraction for each tissue of the model Eartha.

Dizzie	Number of Voxels	Volume [dm3]	Mass [kg]	Volume Fraction [%]
Artery	7619	6.10E-02	6.46E-02	2.46E-03
Blood Vessel	72	5.75E-04	6.10E-04	2.32E-05
Brain Grey Matter	80813	6.47E-01	6.72E-01	2.61E-02
Brain White Matter	43381	3.47E-01	3.62E-01	1.40E-02
Cartilage	3822	3.06E-02	3.36E-02	1.24E-03
Cerebellum	16852	1.35E-01	1.40E-01	5.45E-03
Cerebrospinal Fluid	52320	4.19E-01	4.21E-01	1.69E-02
Connective Tissue	26584	2.13E-01	2.15E-01	8.60E-03
Ear Cartilage	341	2.73E-03	3.00E-03	1.10E-04
Ear skin	1380	1.10E-02	1.21E-02	4.46E-04
Esophagus	1556	1.24E-02	1.29E-02	5.03E-04
Eye Vitreous Humor	1424	1.14E-02	1.15E-02	4.60E-04
Eye Lens	26	2.06E-04	2.25E-04	8.33E-06
Fat	272579	2.18E+00	2.00E+00	8.81E-02
Hippocampus	157	1.26E-03	1.30E-03	5.07E-05
Hypothalamus	51	4.08E-04	4.28E-04	1.65E-05
Intervertebral Disc	7325	5.86E-02	6.45E-02	2.37E-03
Mandible	3225	2.58E-02	5.13E-02	1.04E-03
Marrow Red	49780	3.98E-01	4.09E-01	1.61E-02
Midbrain	945	7.56E-03	7.86E-03	3.06E-04
Muscle	1158969	9.27E+00	9.65E+00	3.75E-01
Nerve	5410	4.33E-02	4.49E-02	1.75E-03
Pharynx	62	4.95E-04	6.44E-07	2.00E-05
Skin	200093	1.60E+00	1.76E+00	6.47E-02
Skull	35072	2.81E-01	5.58E-01	1.13E-02
Spinal Cord	2415	1.93E-02	2.01E-02	7.81E-04
SAT	385422	3.08E+00	2.82E+00	1.25E-01
Teeth	648	5.19E-03	1.12E-02	2.10E-04
Thalamus	2013	1.61E-02	1.67E-02	6.51E-04
Tongue	5160	4.13E-02	4.30E-02	1.67E-03
Trachea	1018	8.14E-03	8.96E-03	3.29E-04
Vein	7571	6.06E-02	6.42E-02	2.45E-03
Vertebrae	54999	4.40E-01	8.76E-01	1.78E-02
Pinealbody	38	3.05E-04	3.20E-04	1.23E-05
Pons	1724	1.38E-02	1.43E-02	5.57E-04
Medulla Oblongata	677	5.41E-03	5.62E-03	2.19E-04
Bone	103122	8.25E-01	1.64E+00	3.33E-02
Bronchi	346	2.77E-03	2.94E-03	1.12E-04
Bronchi Lumen	205	1.64E-03	2.13E-06	6.62E-05
Esophagus Lumen	497	3.98E-03	4.18E-03	1.61E-04
Gallbladder	1435	1.15E-02	1.18E-02	4.64E-04
Heart Lumen	6619	5.30E-02	5.61E-02	2.14E-03
Heart Muscle	30439	2.44E-01	2.58E-01	9.84E-03
Kidney Medulla	19227	1.54E-01	1.61E-01	6.22E-03
Large Intestine	26652	2.13E-01	2.23E-01	8.62E-03
Large Intestine Lumen	72404	5.79E-01	6.05E-01	2.34E-02
Liver	104489	8.36E-01	8.78E-01	3.38E-02
Lung	166336	1.33E+00	8.72E-01	5.38E-02

Dizzie (continuation)	Number of Voxels	Volume [dm3]	Mass [kg]	Volume Fraction [%]
Pancreas	1089	8.71E-03	9.10E-03	3.52E-04
Small Intestine	5853	4.68E-02	4.89E-02	1.89E-03
Small Intestine Lumen	13746	1.10E-01	1.15E-01	4.44E-03
Spleen	34259	2.74E-01	2.89E-01	1.11E-02
Stomach	13396	1.07E-01	1.13E-01	4.33E-03
Stomach Lumen	9063	7.25E-02	7.61E-02	2.93E-03
Tendon Ligament	34356	2.75E-01	3.05E-01	1.11E-02
Thymus	3610	2.89E-02	2.96E-02	1.17E-03
Trachea Lumen	377	3.02E-03	3.92E-06	1.22E-04
Bladder	6452	5.16E-02	5.37E-02	2.09E-03
Epididymis	75	5.98E-04	6.28E-04	2.42E-05
Patella	589	4.71E-03	9.38E-03	1.90E-04
Penis	788	6.30E-03	6.68E-03	2.55E-04
Prostate	521	4.17E-03	4.35E-03	1.68E-04
Testis	153	1.22E-03	1.28E-03	4.95E-05
Ureter Urethra	176	1.41E-03	1.49E-03	5.69E-05
Meniscus	3189	2.55E-02	2.80E-02	1.03E-03

Table A.2-6: Number of voxels, volume, mass and relative fraction for each tissue of the model Dizzie.

Billie	Number of Voxels	Volume [dm3]	Mass [kg]	Volume Fraction [%]
Adrenal gland	1043	8.34E-03	8.55E-03	2.53E-04
Artery	20195	1.62E-01	1.71E-01	4.90E-03
Bladder	4144	3.32E-02	3.45E-02	1.01E-03
Bone	205159	1.64E+00	3.27E+00	4.98E-02
Brain Grey Matter	82321	6.59E-01	6.84E-01	2.00E-02
Brain white Matter	45641	3.65E-01	3.81E-01	1.11E-02
Bronchi	266	2.13E-03	2.27E-03	6.46E-05
Bronchi Lumen	778	6.23E-03	8.09E-06	1.89E-04
Cartilage	14394	1.15E-01	1.27E-01	3.49E-03
Cerebellum	16731	1.34E-01	1.39E-01	4.06E-03
Cerebrospinal Fluid	35015	2.80E-01	2.82E-01	8.50E-03
Commissura Anterior	8	6.50E-05	6.78E-05	1.97E-06
Commissura Posterior	3	2.00E-05	2.09E-05	6.07E-07
Connective Tissue	103209	8.26E-01	8.36E-01	2.50E-02
cornea	21	1.71E-04	1.84E-04	5.19E-06
Diaphragm	13729	1.10E-01	1.14E-01	3.33E-03
Ear Cartilage	435	3.48E-03	3.83E-03	1.06E-04
Ear Skin	1341	1.07E-02	1.18E-02	3.25E-04
Esophagus	515	4.12E-03	4.28E-03	1.25E-04
Esophagus Lumen	539	4.31E-03	4.52E-03	1.31E-04
Eye Lens	30	2.42E-04	2.64E-04	7.34E-06
Eye Sclera	426	3.41E-03	3.51E-03	1.03E-04
Eye Vitreous Humor	1056	8.45E-03	8.52E-03	2.56E-04
Fat	278656	2.23E+00	2.04E+00	6.76E-02
Gallbladder	2472	1.98E-02	2.03E-02	6.00E-04
Heart Lumen	14954	1.20E-01	1.27E-01	3.63E-03
Heart Muscle	17815	1.43E-01	1.51E-01	4.32E-03
Hippocampus	131	1.05E-03	1.09E-03	3.17E-05
Hypophysis	25	1.97E-04	2.10E-04	5.98E-06
Hypothalamus	179	1.43E-03	1.50E-03	4.34E-05
Intervertebral Disc	14615	1.17E-01	1.29E-01	3.55E-03
Kidney Cortex	14295	1.14E-01	1.20E-01	3.47E-03
Kidney Medulla	5384	4.31E-02	4.50E-02	1.31E-03
Large Intestine	32951	2.64E-01	2.75E-01	8.00E-03
Large Intestine Lumen	11114	8.89E-02	9.28E-02	2.70E-03
Larynx	249	1.99E-03	2.15E-03	6.03E-05
Liver	103723	8.30E-01	8.71E-01	2.52E-02
Lung	171735	1.37E+00	9.00E-01	4.17E-02
Mandible	2704	2.16E-02	4.30E-02	6.56E-04
Marrow Red	40561	3.24E-01	3.33E-01	9.84E-03
Medulla Oblongata	796	6.37E-03	6.62E-03	1.93E-04
Meniscus	1445	1.16E-02	1.27E-02	3.51E-04
Midbrain	888	7.11E-03	7.38E-03	2.16E-04
Mucosa	189	1.51E-03	1.58E-03	4.57E-05
Muscle	1714932	1.37E+01	1.43E+01	4.16E-01
Nerve	6692	5.35E-02	5.56E-02	1.62E-03
Ovary	589	4.71E-03	4.93E-03	1.43E-04
Pancreas	2949	2.36E-02	2.46E-02	7.15E-04

Billie (continuation)	Number of Voxels	Volume [dm3]	Mass [kg]	Volume Fraction [%]
Patella	2172	1.74E-02	3.46E-02	5.27E-04
Pharynx	401	3.21E-03	4.17E-06	9.74E-05
Pinealbody	11	8.80E-05	9.24E-05	2.67E-06
Pons	1608	1.29E-02	1.34E-02	3.90E-04
SAT	453233	3.63E+00	3.32E+00	1.10E-01
Skin	312119	2.50E+00	2.75E+00	7.57E-02
Skull	37110	2.97E-01	5.91E-01	9.00E-03
Small Intestine	48432	3.87E-01	4.05E-01	1.18E-02
Small Intestine Lumen	30683	2.45E-01	2.56E-01	7.45E-03
Spinal Cord	2750	2.20E-02	2.28E-02	6.67E-04
Spleen	17513	1.40E-01	1.48E-01	4.25E-03
Stomach	50003	4.00E-01	4.20E-01	1.21E-02
Stomach Lumen	31631	2.53E-01	2.66E-01	7.68E-03
Teeth	1866	1.49E-02	3.22E-02	4.53E-04
Tendon Ligament	27594	2.21E-01	2.45E-01	6.70E-03
Thalamus	1612	1.29E-02	1.34E-02	3.91E-04
Thymus	3698	2.96E-02	3.04E-02	8.97E-04
Thyroid Gland	1256	1.00E-02	1.05E-02	3.05E-04
Tongue	6261	5.01E-02	5.21E-02	1.52E-03
Trachea	262	2.10E-03	2.30E-03	6.35E-05
Trachea Lumen	813	6.50E-03	8.45E-06	1.97E-04
Ureter Urethra	27	2.19E-04	2.31E-04	6.64E-06
Uterus	2333	1.87E-02	1.96E-02	5.66E-04
Vagina	451	3.61E-03	3.76E-03	1.09E-04
Vein	23638	1.89E-01	2.00E-01	5.74E-03
Vertebrae	68820	5.51E-01	1.10E+00	1.67E-02

Table A.2-7: Number of voxels, volume, mass and relative fraction for each tissue of the model Billie.

US 2	Number of Voxels	Volume [dm3]	Mass [kg]	Volume Fraction [%]
Amniotic Fluid	1329	1.06E-02	1.06E-02	2.21E-04
Fetus	345	2.76E-03	2.87E-03	5.74E-05
Hypothalamus	93	7.44E-04	7.81E-04	1.55E-05
Mother	6005169	4.80E+01	5.28E+01	9.99E-01
Umbilical Cord	51	4.08E-04	4.06E-04	8.49E-06
Placenta	3348	2.68E-02	2.67E-02	5.57E-04

Table A.2-8: Number of voxels, volume, mass and relative fraction for each tissue of the model FEMONUM US 2.

US 4	Number of Voxels	Volume [dm^3]	Mass [kg]	Volume Fraction [%]
Amniotic Fluid	9285	7.43E-02	7.43E-02	1.54E-03
Fetus	4591	3.67E-02	3.82E-02	7.63E-04
Hypothalamus	93	7.44E-04	7.81E-04	1.55E-05
Mother	5975929	4.78E+01	5.26E+01	9.93E-01
Umbilical Cord	527	4.22E-03	4.19E-03	8.76E-05
Placenta	25607	2.05E-01	2.04E-01	4.26E-03

Table A.2-9: Number of voxels, volume, mass and relative fraction for each tissue of the model FEMONUM US 4.

MRI 1	Number of Voxels	Volume [dm3]	Mass [kg]	Volume Fraction [%]
Amniotic Fluid	90334	7.23E-01	7.23E-01	1.44E-02
Bladder	430	3.44E-03	3.58E-03	6.87E-05
Brain	12682	1.01E-01	1.04E-01	2.03E-03
CSF	10437	8.35E-02	8.60E-02	1.67E-03
Eyes	353	2.82E-03	2.85E-03	5.64E-05
Fetus	91608	7.33E-01	7.62E-01	1.46E-02
Heart	2575	2.06E-02	2.18E-02	4.12E-04
Hypothalamus	93	7.44E-04	7.81E-04	1.49E-05
Lungs	5782	4.63E-02	4.86E-02	9.24E-04
Mother	5830228	4.66E+01	5.13E+01	9.32E-01
Stomach	784	6.27E-03	6.59E-03	1.25E-04
Umbilical Cord	7708	6.17E-02	6.14E-02	1.23E-03
UterusWall/Placenta	203939	1.63E+00	1.68E+00	3.26E-02

Table A.2-10: Number of voxels, volume, mass and relative fraction for each tissue of the model FEMONUM MRI 1.

MRI 2	Number of Voxels	Volume [dm3]	Mass [kg]	Volume Fraction [%]
Amniotic Fluid	89549	7.16E-01	7.16E-01	1.43E-02
Bladder	1200	9.60E-03	9.98E-03	1.91E-04
Brain	29918	2.39E-01	2.47E-01	4.77E-03
CSF	12278	9.82E-02	1.01E-01	1.96E-03
Eyes	606	4.85E-03	4.89E-03	9.66E-05
Fetus	170066	1.36E+00	1.41E+00	2.71E-02
Heart	2118	1.69E-02	1.80E-02	3.37E-04
Hypothalamus	93	7.44E-04	7.81E-04	1.48E-05
Lungs	9072	7.26E-02	7.62E-02	1.45E-03
Mother	5776492	4.62E+01	5.08E+01	9.20E-01
Stomach	944	7.55E-03	7.93E-03	1.50E-04
Umbilical Cord	7914	6.33E-02	6.30E-02	1.26E-03
UterusWall/Placenta	175562	1.40E+00	1.45E+00	2.80E-02

Table A.2-11: Number of voxels, volume, mass and relative fraction for each tissue of the model FEMONUM MRI 2.

MRI 3	Number of Voxels	Volume [dm3]	Mass [kg]	Volume Fraction [%]
Amniotic Fluid	33896	2.71E-01	2.71E-01	5.43E-03
Bladder	332	2.66E-03	2.76E-03	5.32E-05
Brain	29247	2.34E-01	2.41E-01	4.69E-03
CSF	13160	1.05E-01	1.08E-01	2.11E-03
Eyes	622	4.98E-03	5.02E-03	9.97E-05
Fetus	165252	1.32E+00	1.37E+00	2.65E-02
Heart	2390	1.91E-02	2.03E-02	3.83E-04
Hypothalamus	93	7.44E-04	7.81E-04	1.49E-05
Lungs	11220	8.98E-02	9.42E-02	1.80E-03
Mother	5825308	4.66E+01	5.13E+01	9.34E-01
Stomach	314	2.51E-03	2.64E-03	5.03E-05
Umbilical Cord	4170	3.34E-02	3.32E-02	6.68E-04
UterusWall/Placenta	152317	1.22E+00	1.26E+00	2.44E-02

Table A.2-12: Number of voxels, volume, mass and relative fraction for each tissue of the model FEMONUM MRI 3.

MRI 4	Number of Voxels	Volume [dm3]	Mass [kg]	Volume Fraction [%]
Amniotic Fluid	66691	5.34E-01	5.34E-01	1.09E-02
Bladder	611	4.89E-03	5.08E-03	9.99E-05
Brain	25664	2.05E-01	2.11E-01	4.20E-03
CSF	5632	4.51E-02	4.64E-02	9.21E-04
Eyes	390	3.12E-03	3.15E-03	6.38E-05
Fetus	76395	6.11E-01	6.36E-01	1.25E-02
Heart	620	4.96E-03	5.26E-03	1.01E-04
Hypothalamus	93	7.44E-04	7.81E-04	1.52E-05
Lungs	2044	1.64E-02	1.72E-02	3.34E-04
Mother	5845319	4.68E+01	5.14E+01	9.56E-01
Stomach	271	2.17E-03	2.28E-03	4.43E-05
Umbilical Cord	3269	2.62E-02	2.60E-02	5.35E-04
UterusWall/Placenta	87215	6.98E-01	7.19E-01	1.43E-02

Table A.2-13: Number of voxels, volume, mass and relative fraction for each tissue of the model FEMONUM MRI 4.

MRI 5	Number of Voxels	Volume [dm3]	Mass [kg]	Volume Fraction [%]
Amniotic Fluid	80720	6.46E-01	6.46E-01	1.19E-02
Bladder	1465	1.17E-02	1.22E-02	2.16E-04
Brain	32328	2.59E-01	2.66E-01	4.77E-03
CSF	14907	1.19E-01	1.23E-01	2.20E-03
Eyes	609	4.87E-03	4.92E-03	8.98E-05
Fetus	180634	1.45E+00	1.50E+00	2.66E-02
Heart	1262	1.01E-02	1.07E-02	1.86E-04
Hypothalamus	93	7.44E-04	7.81E-04	1.37E-05
Lungs	12149	9.72E-02	1.02E-01	1.79E-03
Mother	6205656	4.96E+01	5.46E+01	9.15E-01
Stomach	1213	9.70E-03	1.02E-02	1.79E-04
Umbilical Cord	10904	8.72E-02	8.68E-02	1.61E-03
UterusWall/Placenta	242085	1.94E+00	1.99E+00	3.57E-02

Table A.2-14: Number of voxels, volume, mass and relative fraction for each tissue of the model FEMONUM MRI 5.

MRI 6	Number of Voxels	Volume [dm3]	Mass [kg]	Volume Fraction [%]
Amniotic Fluid	76076	6.09E-01	6.09E-01	1.21E-02
Bladder	846	6.77E-03	7.04E-03	1.35E-04
Brain	27860	2.23E-01	2.30E-01	4.44E-03
CSF	12818	1.03E-01	1.06E-01	2.04E-03
Eyes	596	4.77E-03	4.81E-03	9.49E-05
Fetus	172928	1.38E+00	1.44E+00	2.75E-02
Heart	1478	1.18E-02	1.25E-02	2.35E-04
Hypothalamus	93	7.44E-04	7.81E-04	1.48E-05
Lungs	7394	5.92E-02	6.21E-02	1.18E-03
Mother	5830021	4.66E+01	5.13E+01	9.29E-01
Stomach	1509	1.21E-02	1.27E-02	2.40E-04
Umbilical Cord	9714	7.77E-02	7.73E-02	1.55E-03
UterusWall/Placenta	136727	1.09E+00	1.13E+00	2.18E-02

Table A.2-15: Number of voxels, volume, mass and relative fraction for each tissue of the model FEMONUM MRI 6.

MRI 7	Number of Voxels	Volume [dm3]	Mass [kg]	Volume Fraction [%]
Amniotic Fluid	101959	8.16E-01	8.16E-01	1.62E-02
Bladder	1945	1.56E-02	1.62E-02	3.10E-04
Brain	22204	1.78E-01	1.83E-01	3.54E-03
CSF	7982	6.39E-02	6.58E-02	1.27E-03
Eyes	349	2.79E-03	2.82E-03	5.56E-05
Fetus	109745	8.78E-01	9.13E-01	1.75E-02
Hypothalamus	93	7.44E-04	7.81E-04	1.48E-05
Mother	5899543	4.72E+01	5.19E+01	9.40E-01
Stomach	879	7.03E-03	7.38E-03	1.40E-04
Umbilical Cord	4038	3.23E-02	3.21E-02	6.43E-04
UterusWall/Placenta	128517	1.03E+00	1.06E+00	2.05E-02

Table A.2-16: Number of voxels, volume, mass and relative fraction for each tissue of the model FEMONUM MRI 6.

MRI 8	Number of Voxels	Volume [dm^3]	Mass [kg]	Volume Fraction [%]
Amniotic Fluid	28861	2.31E-01	2.31E-01	4.62E-03
Bladder	1622	1.30E-02	1.35E-02	2.60E-04
Brain	28704	2.30E-01	2.37E-01	4.60E-03
CSF	14591	1.17E-01	1.20E-01	2.34E-03
Eyes	564	4.51E-03	4.55E-03	9.03E-05
Fetus	127113	1.02E+00	1.06E+00	2.04E-02
Heart	1840	1.47E-02	1.56E-02	2.95E-04
Hypothalamus	93	7.44E-04	7.81E-04	1.49E-05
Lungs	6922	5.54E-02	5.81E-02	1.11E-03
Mother	5818533	4.65E+01	5.12E+01	9.32E-01
Stomach	424	3.39E-03	3.56E-03	6.79E-05
Umbilical Cord	6948	5.56E-02	5.53E-02	1.11E-03
UterusWall/Placenta	208904	1.67E+00	1.72E+00	3.35E-02

Table A.2-17: Number of voxels, volume, mass and relative fraction for each tissue of the model FEMONUM MRI 8.

MRI 9	Number of Voxels	Volume [dm3]	Mass [kg]	Volume Fraction [%]
Amniotic Fluid	65631	5.25E-01	5.25E-01	1.06E-02
Bladder	291	2.33E-03	2.42E-03	4.69E-05
Brain	23599	1.89E-01	1.94E-01	3.80E-03
CSF	9098	7.28E-02	7.50E-02	1.46E-03
Eyes	394	3.15E-03	3.18E-03	6.34E-05
Fetus	97560	7.80E-01	8.12E-01	1.57E-02
Heart	946	7.57E-03	8.02E-03	1.52E-04
Hypothalamus	93	7.44E-04	7.81E-04	1.50E-05
Lungs	5436	4.35E-02	4.57E-02	8.75E-04
Mother	5822226	4.66E+01	5.12E+01	9.37E-01
Stomach	444	3.55E-03	3.73E-03	7.15E-05
Umbilical Cord	7767	6.21E-02	6.18E-02	1.25E-03
UterusWall/Placenta	177773	1.42E+00	1.46E+00	2.86E-02

Table A.2-18: Number of voxels, volume, mass and relative fraction for each tissue of the model FEMONUM MRI 9.

MRI 10	Number of Voxels	Volume [dm3]	Mass [kg]	Volume Fraction [%]
Amniotic Fluid	53420	4.27E-01	4.27E-01	8.41E-03
Bladder	489	3.91E-03	4.07E-03	7.69E-05
Brain	39348	3.15E-01	3.24E-01	6.19E-03
CSF	17194	1.38E-01	1.42E-01	2.71E-03
Eyes	644	5.15E-03	5.20E-03	1.01E-04
Fetus	198024	1.58E+00	1.65E+00	3.12E-02
Heart	3709	2.97E-02	3.15E-02	5.84E-04
Hypothalamus	93	7.44E-04	7.81E-04	1.46E-05
Lungs	8466	6.77E-02	7.11E-02	1.33E-03
Mother	5762630	4.61E+01	5.07E+01	9.07E-01
Stomach	1110	8.88E-03	9.32E-03	1.75E-04
Umbilical Cord	25230	2.02E-01	2.01E-01	3.97E-03
UterusWall/Placenta	245022	1.96E+00	2.02E+00	3.86E-02

Table A.2-19: Number of voxels, volume, mass and relative fraction for each tissue of the model FEMONUM MRI 10.

MRI 11	Number of Voxels	Volume [dm3]	Mass [kg]	Volume Fraction [%]
Amniotic Fluid	62569	5.01E-01	5.01E-01	9.82E-03
Bladder	2979	2.38E-02	2.48E-02	4.68E-04
Brain	32870	2.63E-01	2.71E-01	5.16E-03
CSF	21275	1.70E-01	1.75E-01	3.34E-03
Eyes	774	6.19E-03	6.25E-03	1.21E-04
Fetus	253530	2.03E+00	2.11E+00	3.98E-02
Heart	2280	1.82E-02	1.93E-02	3.58E-04
Hypothalamus	93	7.44E-04	7.81E-04	1.46E-05
Lungs	14504	1.16E-01	1.22E-01	2.28E-03
Mother	5673423	4.54E+01	4.99E+01	8.91E-01
Stomach	2226	1.78E-02	1.87E-02	3.49E-04
Umbilical Cord	7930	6.34E-02	6.31E-02	1.24E-03
UterusWall/Placenta	296478	2.37E+00	2.44E+00	4.65E-02

Table A.2-20: Number of voxels, volume, mass and relative fraction for each tissue of the model FEMONUM MRI 11.

MRI 12	Number of Voxels	Volume [dm3]	Mass [kg]	Volume Fraction [%]
Amniotic Fluid	167556	1.34E+00	1.34E+00	2.49E-02
Bladder	2036	1.63E-02	1.69E-02	3.02E-04
Brain	24305	1.94E-01	2.00E-01	3.61E-03
CSF	10821	8.66E-02	8.92E-02	1.61E-03
Eyes	527	4.22E-03	4.25E-03	7.82E-05
Fetus	140304	1.12E+00	1.17E+00	2.08E-02
Heart	516	4.13E-03	4.38E-03	7.66E-05
Hypothalamus	93	7.44E-04	7.81E-04	1.38E-05
Lungs	6174	4.94E-02	5.19E-02	9.16E-04
Mother	5844597	4.68E+01	5.14E+01	8.67E-01
Stomach	723	5.78E-03	6.07E-03	1.07E-04
Umbilical Cord	10805	8.64E-02	8.60E-02	1.60E-03
UterusWall/Placenta	303019	2.42E+00	2.50E+00	4.50E-02
Bladder 2	896	7.17E-03	7.45E-03	1.33E-04
Brain 2	28882	2.31E-01	2.38E-01	4.28E-03
CSF 2	10866	8.69E-02	8.95E-02	1.61E-03
Eyes 2	534	4.27E-03	4.31E-03	7.92E-05
Fetus 2	163903	1.31E+00	1.36E+00	2.43E-02
Heart 2	1317	1.05E-02	1.12E-02	1.95E-04
Lungs 2	9408	7.53E-02	7.90E-02	1.40E-03
Stomach 2	1595	1.28E-02	1.34E-02	2.37E-04
Umbilical Cord 2	11686	9.35E-02	9.30E-02	1.73E-03

Table A.2-21: Number of voxels, volume, mass and relative fraction for each tissue of the model FEMONUM MRI 12.

A.3 Thermal Properties of Human Tissue

Norman	Density [kg/m³]	Heat conductivity [W/(mK)]	Heat capacity [kJ/(K kg)]	Blood flow [W/(K m³)]	Metabolic rate [W/m³]
Source: [114] [103] [115] [27] [116] [117] [64] [98]					
Adrenals	1024	0,42	3,3	270000	48000
Bile	1010	0,55	4,1	0	0
Bladder	1040	0,43	3,2	9000	160
Blood	1060	0,56	3,9	0	0
Bone	1990	0,37	3,1	3400	610
Brain	1035	0,57	3,8	40000	7100
Breast	1020	0,22	3	1500	300
Csf	1007	0,62	4	0	0
Duodenum	1044	0,57	4	71000	13000
Fat	916	0,22	3	1500	300
Gall_bladder	1026	0,43	3,2	9000	160
Heart_muscle	1060	0,54	3,9	54000	9600
Humour	1009	0,58	4	0	0
Hypothalamus	1050	0,53	3,761	360000	64000
Kidney	1050	0,54	4	270000	48000
Lens	1077	0,4	3,6	0	0
Liver	1050	0,51	3,7	68000	12000
Lower_LI	1044	0,56	3,7	53000	9500
Lunch	1044	0,56	3,9	0	0
Lung	1050	0,14	3,8	9500	1700
Muscle	1041	0,4	3,8	2000	480
Oesophagus	1040	0,53	3,5	29000	5200
Pancreas	1045	0,52	4	41000	7300
Prostate	1045	0,53	3,761	360000	64000
Sclera	1076	0,58	3,8	75000	22000
Skin	1100	0,27	3,6	1700	1620
Small_intestine	1044	0,57	4	71000	13000
Spinal_cord	1038	0,46	3,4	40000	7100
Spleen	1054	0,54	3,9	82000	15000
Stomach	1050	0,53	4	29000	5200
Tendon	1165	0,41	3,3	9000	1600
Testis	1044	0,56	3,9	360000	64000
Thymus	1026	0,52	3,96	360000	64000
Thyroid	1050	0,53	3,553	360000	64000
Trabec_bone	1920	0,41	3,2	3300	590
Upper_LI	1044	0,56	3,7	53000	9500
Urine	1025	0,56	3,9	0	0

Table A.3-1: Thermal properties including the heat conductivity, the heat capacity, the blood flow and the metabolic rate of the model NORMAN.

Billie	**Density [kg/m³]**	**Heat conductivity [W/(mK)]**	**Heat capacity [kJ/(K kg)]**	**Blood flow [W/(K m³)]**	**Metabolic rate [W/m³]**
Source: [114] [103] [115] [27] [116] [117] [64] [98]					
Adrenal_gland	1025	0,39	3,128	363771	64670,4
Artery	1060	0,51	3,824	0	0
Bladder	1040	0,56	3,9	12125,7	215,568
Bone	1990	0,4	1,289	4580,82	821,853
Brain_grey_matter	1039	1,13	3,675	53892	9565,83
Brain_white_matter	1043	0,5	3,621	53892	9565,83
Bronchi	1063	0,46	3,456	12799,35	2290,41
Bronchi_lumen	1,3	0,03	1,006	0	0
Cartilage	1100	0,47	3,664	12125,7	2155,68
Cerebellum	1040	0,53	3,64	53892	9565,83
Cerebrospinal_fluid	1007	0,6	4,191	0	0
Commissura_anterior	1043	0,5	3,621	53892	9565,83
Commissura_posterior	1043	0,5	3,621	53892	9565,83
Connective_tissue	1013	0,37	3,035	7073,325	1279,935
cornea	1076	0,52	3,793	0	0
Diaphragm	1041	0,53	3,546	2694,6	646,704
Ear_cartilage	1100	0,47	3,664	12125,7	2155,68
Ear_skin	1100	0,35	3,437	2290,41	2182,626
Esophagus	1040	0,53	3,5	39071,7	7005,96
Esophagus_lumen	1050	0,03	1,006	0	0
Eye_lens	1090	0,4	3,664	0	0
Eye_Sclera	1032	0,4	3	101047,5	29640,6
Eye_vitreous_humor	1009	0,59	3,932	0	0
Fat	916	0,25	2,524	2290,41	404,19
Gallbladder	1026	0,47	3,496	12125,7	2155,68
Heart_lumen	1060	0,51	3,824	0	0
Heart_muscle	1060	0,54	3,72	2694,6	646,704
Hippocampus	1039	1,13	3,675	53892	9565,83
Hypophysis	1066	0,53	3,761	485028	86227,2
Hypothalamus	1050	0,53	3,761	485028	86227,2
Intervertebral_disc	1100	0,47	3,664	12125,7	2155,68
Kidney_cortex	1049	0,52	3,745	363771	64670,4
Kidney_medulla	1044	0,52	3,745	363771	64670,4
Large_intestine	1044	0,56	3,653	71406,9	12799,35
Large_intestine_lumen	1044	0,56	3,9	0	0
Larynx	1082	0,47	3,664	12125,7	2155,68
Liver	1050	0,51	3,6	91616,4	16167,6
Lung	1050	0,44	3,625	12799,35	2290,41
Mandible	1990	0,4	1,289	4580,82	821,853
Marrow_red	1027	0,52	3,96	43113,6	7679,61
Medulla_oblongata	1039	1,13	3,675	53892	9565,83
Meniscus	1098	0,47	3,664	12125,7	2155,68
Midbrain	1039	1,13	3,675	53892	9565,83

Billie (continuation)	Density [kg/m³]	Heat conductivity [W/(mK)]	Heat capacity [kJ/(K kg)]	Blood flow [W/(K m³)]	Metabolic rate [W/m³]
Mucosa	1050	0,34	3,15	12125,7	2155,68
Muscle	1041	0,53	3,546	2694,6	646,704
Nerve	1038	0,46	3,664	53892	9565,83
Ovary	1048	0,53	3,6	485028	86227,2
Pancreas	1045	0,49	3,452	55239,3	9835,29
Patella	1990	0,4	1,289	4580,82	821,853
Pharynx	1,3	0,03	1,006	0	0
Pinealbody	1050	0,53	3,6	485028	86227,2
Pons	1039	1,13	3,675	53892	9565,83
SAT	916	0,24	2,524	2020,95	404,19
Skin	1100	0,35	3,437	2290,41	2182,626
Skull	1990	0,4	1,289	4580,82	821,853
Small_intestine	1044	0,56	3,653	95658,3	17514,9
Small_intestine_lumen	1044	0,56	3,9	0	0
Spinal_cord	1038	0,46	3,664	53892	9565,83
Spleen	1054	0,54	3,603	110478,6	20209,5
Stomach	1050	0,53	3,553	39071,7	7005,96
Stomach_lumen	1050	0,56	3,9	0	0
Teeth	2160	0,4	1,34	4580,82	821,853
Tendon_Ligament	1110	0,5	3,5	12125,7	2155,68
Thalamus	1039	1,13	3,675	53892	9565,83
Thymus	1026	0,52	3,96	485028	86227,2
Thyroid_gland	1050	0,53	3,553	485028	86227,2
Tongue	1041	0,53	3,546	2694,6	646,704
Trachea	1100	0,47	3,664	12125,7	2155,68
Trachea_lumen	1,3	0,03	1,006	0	0
Ureter_Urethra	1056	0,46	3,456	12125,7	2155,68
Uterus	1052	0,5	3,58	24251,4	4850,28
Vagina	1044	0,56	3,653	71406,9	12799,35
Vein	1060	0,51	3,824	0	0
Vertebrae	1990	0,4	1,289	4580,82	821,853

Table A.3-2: Thermal properties including the heat conductivity, the heat capacity, the blood flow and the metabolic rate of the model Billie.

Dizzie	Density [kg/m³]	Heat conductivity [W/(mK)]	Heat capacity [kJ/(K kg)]	Blood flow [W/(K m³)]	Metabolic rate [W/m³]
Source: [114] [103] [115] [27] [116] [117] [64]					
Artery	1060	0,51	3,824	0	0
Bladder	1040	0,56	3,9	15209,1	270,384
Blood_vessel	1060	0,51	3,824	0	0
Bone	1990	0,4	1,289	5745,66	1030,839
Brain_grey_matter	1039	1,13	3,675	67596	11998,29
Brain_white_matter	1043	0,5	3,621	67596	11998,29
Bronchi	1063	0,46	3,456	16054,05	2872,83
Bronchi_lumen	1,3	0,03	1,006	0	0
Cartilage	1100	0,47	3,664	15209,1	2703,84
Cerebellum	1040	0,53	3,64	67596	11998,29
Cerebrospinal_fluid	1007	0,6	4,191	0	0
Connective_tissue	1013	0,37	3,035	8871,975	1605,405
Ear_cartilage	1100	0,47	3,664	15209,1	2703,84
Ear_skin	1100	0,35	3,437	2872,83	2737,638
Epididymis	1050	0,53	3,761	608364	108153,6
Esophagus	1040	0,53	3,5	49007,1	8787,48
Esophagus_lumen	1050	0,03	1,006	0	0
Eye_lens	1090	0,4	3,664	0	0
Eye_vitreous_humor	1009	0,59	3,932	0	0
Fat	916	0,25	2,524	2872,83	506,97
Gallbladder	1026	0,47	3,496	15209,1	2703,84
Heart_lumen	1060	0,51	3,824	0	0
Heart_muscle	1060	0,54	3,72	3379,8	811,152
Hippocampus	1039	1,13	3,675	67596	11998,29
Hypothalamus	1050	0,53	3,761	608364	108153,6
Intervertebral_disc	1100	0,47	3,664	15209,1	2703,84
Kidney_medulla	1044	0,52	3,745	456273	81115,2
Large_intestine	1044	0,56	3,653	89564,7	16054,05
Large_intestine_lumen	1044	0,56	3,9	0	0
Liver	1050	0,51	3,6	114913,2	20278,8
Lung	1050	0,44	3,625	16054,05	2872,83
Mandible	1990	0,4	1,289	5745,66	1030,839
Marrow_red	1027	0,52	3,96	54076,8	9632,43
Medulla_oblongata	1039	1,13	3,675	67596	11998,29
Meniscus	1098	0,47	3,664	15209,1	2703,84
Midbrain	1039	1,13	3,675	67596	11998,29
Muscle	1041	0,53	3,546	3379,8	811,152
Nerve	1038	0,46	3,664	67596	11998,29
Pancreas	1045	0,49	3,452	69285,9	12336,27
Patella	1990	0,4	1,289	5745,66	1030,839
Penis	1060	0,46	3,456	3379,8	811,152
Pharynx	1,3	0,03	1,006	0	0
Pinealbody	1050	0,53	3,6	608364	108153,6

Dizzie (continuation)	Density [kg/m³]	Heat conductivity [W/(mK)]	Heat capacity [kJ/(K kg)]	Blood flow [W/(K m³)]	Metabolic rate [W/m³]
Pons	1039	1,13	3,675	67596	11998,29
Prostate	1045	0,53	3,761	608364	108153,6
SAT	916	0,24	2,524	2534,85	506,97
Skin	1100	0,35	3,437	2872,83	2737,638
Skull	1990	0,4	1,289	5745,66	1030,839
Small_intestine	1044	0,56	3,653	119982,9	21968,7
Small_intestine_lumen	1044	0,56	3,9	0	0
Spinal_cord	1038	0,46	3,664	67596	11998,29
Spleen	1054	0,54	3,603	138571,8	25348,5
Stomach	1050	0,53	3,553	49007,1	8787,48
Stomach_lumen	1050	0,56	3,9	0	0
Teeth	2160	0,4	1,34	5745,66	1030,839
Tendon_Ligament	1110	0,5	3,5	15209,1	2703,84
Testis	1044	0,53	3,746	608364	108153,6
Thalamus	1039	1,13	3,675	67596	11998,29
Thymus	1026	0,52	3,96	608364	108153,6
Tongue	1041	0,53	3,546	3379,8	811,152
Trachea	1100	0,47	3,664	15209,1	2703,84
Trachea_lumen	1,3	0,03	1,006	0	0
Ureter_Urethra	1056	0,46	3,456	15209,1	2703,84
Vein	1060	0,51	3,824	0	0
Vertebrae	1990	0,4	1,289	5745,66	1030,839

Table A.3-3: Thermal properties including the heat conductivity, the heat capacity, the blood flow and the metabolic rate of the model Dizzie.

Eartha	Density [kg/m³]	Heat conductivity [W/(mK)]	Heat capacity [kJ/(K kg)]	Blood flow [W/(K m³)]	Metabolic rate [W/m³]
Source: [114] [103] [115] [27] [116] [117] [64] [98]					
Adrenal_gland	1025	0,39	3,128	398992,5	70932
Air_internal	1,3	0,03	1,006	0	0
Artery	1060	0,51	3,824	0	0
Bladder	1040	0,56	3,9	13299,75	236,44
Blood_vessel	1060	0,51	3,824	0	0
Bone	1990	0,4	1,289	5024,35	901,4275
Brain_grey_matter	1039	1,13	3,675	59110	10492,03
Brain_white_matter	1043	0,5	3,621	59110	10492,03
Bronchi	1063	0,46	3,456	14038,63	2512,175
Bronchi_lumen	1,3	0,03	1,006	0	0
Cartilage	1100	0,47	3,664	13299,75	2364,4
Cerebellum	1040	0,53	3,64	59110	10492,03
Cerebrospinal_fluid	1007	0,6	4,191	0	0
Commissura_anterior	1043	0,5	3,621	59110	10492,03
Commissura_posterior	1043	0,5	3,621	59110	10492,03
Connective_tissue	1013	0,37	3,035	7758,188	1403,863
Cornea	1076	0,52	3,793	0	0
Diaphragm	1041	0,53	3,546	2955,5	709,32
Ear_cartilage	1100	0,47	3,664	13299,75	2364,4
Ear_skin	1100	0,35	3,437	2512,175	2393,955
Esophagus	1040	0,53	3,5	42854,75	7684,3
Esophagus_lumen	1050	0,03	1,006	0	0
Eye_lens	1090	0,4	3,664	0	0
Eye_Sclera	1032	0,4	3	110831,3	32510,5
Eye_vitreous_humor	1009	0,59	3,932	0	0
Fat	916	0,25	2,524	2512,175	443,325
Gallbladder	1026	0,47	3,496	13299,75	2364,4
Heart_lumen	1060	0,51	3,824	0	0
Heart_muscle	1060	0,54	3,72	2955,5	709,32
Hippocampus	1039	1,13	3,675	59110	10492,03
Hypophysis	1066	0,53	3,761	531990	94576
Hypothalamus	1050	0,53	3,761	531990	94576
Intervertebral_disc	1100	0,47	3,664	13299,75	2364,4
Kidney_cortex	1049	0,52	3,745	398992,5	70932
Kidney_medulla	1044	0,52	3,745	398992,5	70932
Large_intestine	1044	0,56	3,653	78320,75	14038,63
Large_intestine_lumen	1044	0,56	3,9	0	0
Larynx	1082	0,47	3,664	13299,75	2364,4
Liver	1050	0,51	3,6	100487	17733
Lung	1050	0,44	3,625	14038,63	2512,175
Mandible	1990	0,4	1,289	5024,35	901,4275
Marrow_red	1027	0,52	3,96	47288	8423,175
Medulla_oblongata	1039	1,13	3,675	59110	10492,03

Eartha (continuation)	Density [kg/m³]	Heat conductivity [W/(mK)]	Heat capacity [kJ/(K kg)]	Blood flow [W/(K m³)]	Metabolic rate [W/m³]
Meniscus	1098	0,47	3,664	13299,75	2364,4
Midbrain	1039	1,13	3,675	59110	10492,03
Mucosa	1050	0,34	3,15	13299,75	2364,4
Muscle	1041	0,53	3,546	2955,5	709,32
Nerve	1038	0,46	3,664	59110	10492,03
Ovary	1048	0,53	3,6	531990	94576
Pancreas	1045	0,49	3,452	60587,75	10787,58
Patella	1990	0,4	1,289	5024,35	901,4275
Pharynx	1,3	0,03	1,006	0	0
Pinealbody	1050	0,53	3,6	531990	94576
Pons	1039	1,13	3,675	59110	10492,03
SAT	916	0,24	2,524	2216,625	443,325
Skin	1100	0,35	3,437	2512,175	2393,955
Skull	1990	0,4	1,289	5024,35	901,4275
Small_intestine	1044	0,56	3,653	104920,3	19210,75
Small_intestine_lumen	1044	0,56	3,9	0	0
Spinal_cord	1038	0,46	3,664	59110	10492,03
Spleen	1054	0,54	3,603	121175,5	22166,25
Stomach	1050	0,53	3,553	42854,75	7684,3
Stomach_lumen	1050	0,56	3,9	0	0
Teeth	2160	0,4	1,34	5024,35	901,4275
Tendon_Ligament	1110	0,5	3,5	13299,75	2364,4
Thalamus	1039	1,13	3,675	59110	10492,03
Thymus	1026	0,52	3,96	531990	94576
Tongue	1041	0,53	3,546	2955,5	709,32
Trachea	1100	0,47	3,664	13299,75	2364,4
Trachea_lumen	1,3	0,03	1,006	0	0
Ureter_Urethra	1056	0,46	3,456	13299,75	2364,4
Uterus	1052	0,5	3,58	26599,5	5319,9
Vagina	1044	0,56	3,653	78320,75	14038,63
Vein	1060	0,51	3,824	0	0
Vertebrae	1990	0,4	1,289	5024,35	901,4275

Table A.3-4: Thermal properties including the heat conductivity, the heat capacity, the blood flow and the metabolic rate of the model Eartha.

Thelonious	**Density [kg/m³]**	**Heat conductivity [W/(mK)]**	**Heat capacity [kJ/(K kg)]**	**Blood flow [W/(K m³)]**	**Metabolic rate [W/m³]**
Source: [114] [103] [115] [27] [116] [117] [64]					
Adrenal_gland	1025	0,39	3,128	532332	94636,8
Air_internal	1,3	0,03	1,006	0	0
Artery	1060	0,51	3,824	0	0
Bladder	1040	0,56	3,9	17744,4	315,456
Blood_vessel	1060	0,51	3,824	0	0
Bone	1990	0,4	1,289	6703,44	1202,676
Brain_grey_matter	1039	1,13	3,675	78864	13998,36
Brain_white_matter	1043	0,5	3,621	78864	13998,36
Bronchi	1063	0,46	3,456	18730,2	3351,72
Bronchi_lumen	1,3	0,03	1,006	0	0
Cartilage	1100	0,47	3,664	17744,4	3154,56
Cerebellum	1040	0,53	3,64	78864	13998,36
Cerebrospinal_fluid	1007	0,6	4,191	0	0
commissura_anterior	1043	0,5	3,621	78864	13998,36
commissura_posterior	1043	0,5	3,621	78864	13998,36
Connective_tissue	1013	0,37	3,035	10350,9	1873,02
Cornea	1076	0,52	3,793	0	0
Diaphragm	1041	0,53	3,546	3943,2	946,368
Ear_cartilage	1100	0,47	3,664	17744,4	3154,56
Ear_skin	1100	0,35	3,437	3351,72	3193,992
Epididymis	1050	0,53	3,761	709776	126182,4
Esophagus	1040	0,53	3,5	57176,4	10252,32
Esophagus_lumen	1050	0,03	1,006	0	0
Eye_lens	1090	0,4	3,664	0	0
Eye_Sclera	1032	0,4	3	147870	43375,2
Eye_vitreous_humor	1009	0,59	3,932	0	0
Fat	916	0,25	2,524	3351,72	591,48
Gallbladder	1026	0,47	3,496	17744,4	3154,56
Heart_lumen	1060	0,51	3,824	0	0
Heart_muscle	1060	0,54	3,72	3943,2	946,368
Hippocampus	1039	1,13	3,675	78864	13998,36
Hypophysis	1066	0,53	3,761	709776	126182,4
Hypothalamus	1050	0,53	3,761	709776	126182,4
Intervertebral_disc	1100	0,47	3,664	17744,4	3154,56
Kidney_cortex	1049	0,52	3,745	532332	94636,8
Kidney_medulla	1044	0,52	3,745	532332	94636,8
Large_intestine	1044	0,56	3,653	104494,8	18730,2
Large_intestine_lumen	1044	0,56	3,9	0	0
Larynx	1082	0,47	3,664	17744,4	3154,56
Liver	1050	0,51	3,6	134068,8	23659,2
Lung	1050	0,44	3,625	18730,2	3351,72
Mandible	1990	0,4	1,289	6703,44	1202,676
Marrow_red	1027	0,52	3,96	63091,2	11238,12

Thelonious (continuation)	Density [kg/m³]	Heat conductivity [W/(mK)]	Heat capacity [kJ/(K kg)]	Blood flow [W/(K m³)]	Metabolic rate [W/m³]
Medulla_oblongata	1039	1,13	3,675	78864	13998,36
Meniscus	1098	0,47	3,664	17744,4	3154,56
Midbrain	1039	1,13	3,675	78864	13998,36
Mucosa	1050	0,34	3,15	17744,4	3154,56
Muscle	1041	0,53	3,546	3943,2	946,368
Nerve	1038	0,46	3,664	78864	13998,36
Pancreas	1045	0,49	3,452	80835,6	14392,68
Patella	1990	0,4	1,289	6703,44	1202,676
Penis	1060	0,46	3,456	3943,2	946,368
Pharynx	1,3	0,03	1,006	0	0
Pinealbody	1050	0,53	3,6	709776	126182,4
Pons	1039	1,13	3,675	78864	13998,36
Prostate	1045	0,53	3,761	709776	126182,4
SAT	916	0,24	2,524	2957,4	591,48
Skin	1100	0,35	3,437	3351,72	3193,992
Skull	1990	0,4	1,289	6703,44	1202,676
Small_intestine	1044	0,56	3,653	139983,6	25630,8
Small_intestine_lumen	1044	0,56	3,9	0	0
Spinal_cord	1038	0,46	3,664	78864	13998,36
Spleen	1054	0,54	3,603	161671,2	29574
Stomach	1050	0,53	3,553	57176,4	10252,32
Stomach_lumen	1050	0,56	3,9	0	0
Teeth	2160	0,4	1,34	6703,44	1202,676
Tendon_Ligament	1110	0,5	3,5	17744,4	3154,56
Testis	1044	0,53	3,746	709776	126182,4
Thalamus	1039	1,13	3,675	78864	13998,36
Thymus	1026	0,52	3,96	709776	126182,4
Tongue	1041	0,53	3,546	3943,2	946,368
Trachea	1100	0,47	3,664	17744,4	3154,56
Trachea_lumen	1,3	0,03	1,006	0	0
Ureter_Urethra	1056	0,46	3,456	17744,4	3154,56
Vein	1060	0,51	3,824	0	0
Vertebrae	1990	0,4	1,289	6703,44	1202,676

Table A.3-5: Thermal properties including the heat conductivity, the heat capacity, the blood flow and the metabolic rate of the model Thelonious.

Roberta	Density [kg/m³]	Heat conductivity [W/(mK)]	Heat capacity [kJ/(K kg)]	Blood flow [W/(K m³)]	Metabolic rate [W/m³]
Source: [114] [103] [115] [27] [116] [117] [64] [98]					
Air_internal	1,3	0,03	1,006	0	0
Artery	1060	0,51	3,824	0	0
Bladder	1040	0,56	3,9	17741,7	315,408
Bone	1990	0,4	1,289	6702,42	1202,493
Brain_grey_matter	1039	1,13	3,675	78852	13996,23
Brain_white_matter	1043	0,5	3,621	78852	13996,23
Cartilage	1100	0,47	3,664	17741,7	3154,08
Cerebellum	1040	0,53	3,64	78852	13996,23
Cerebrospinal_fluid	1007	0,6	4,191	0	0
Connective_tissue	1013	0,37	3,035	10349,33	1872,735
Cornea	1076	0,52	3,793	0	0
Ear_cartilage	1100	0,47	3,664	17741,7	3154,08
Ear_skin	1100	0,35	3,437	3351,21	3193,506
Esophagus	1040	0,53	3,5	57167,7	10250,76
Esophagus_lumen	1050	0,03	1,006	0	0
Eye_lens	1090	0,4	3,664	0	0
Eye_Sclera	1032	0,4	3	147847,5	43368,6
Eye_vitreous_humor	1009	0,59	3,932	0	0
Fat	916	0,25	2,524	3351,21	591,39
Gallbladder	1026	0,47	3,496	17741,7	3154,08
Heart_lumen	1060	0,51	3,824	0	0
Heart_muscle	1060	0,54	3,72	3942,6	946,224
Hippocampus	1039	1,13	3,675	78852	13996,23
Hypophysis	1066	0,53	3,761	709668	126163,2
Hypothalamus	1050	0,53	3,761	709668	126163,2
Intervertebral_disc	1100	0,47	3,664	17741,7	3154,08
Kidney_cortex	1049	0,52	3,745	532251	94622,4
Kidney_medulla	1044	0,52	3,745	532251	94622,4
Large_intestine	1044	0,56	3,653	104478,9	18727,35
Large_intestine_lumen	1044	0,56	3,9	0	0
Liver	1050	0,51	3,6	134048,4	23655,6
Lung	1050	0,44	3,625	18727,35	3351,21
Mandible	1990	0,4	1,289	6702,42	1202,493
Marrow_red	1027	0,52	3,96	63081,6	11236,41
Medulla_oblongata	1039	1,13	3,675	78852	13996,23
Meniscus	1098	0,47	3,664	17741,7	3154,08
Midbrain	1039	1,13	3,675	78852	13996,23
Mucosa	1050	0,34	3,15	17741,7	3154,08
Muscle	1041	0,53	3,546	3942,6	946,224
Nerve	1038	0,46	3,664	78852	13996,23
Ovary	1048	0,53	3,6	709668	126163,2
Pancreas	1045	0,49	3,452	80823,3	14390,49
Patella	1990	0,4	1,289	6702,42	1202,493

Roberta (continuation)	Density [kg/m³]	Heat conductivity [W/(mK)]	Heat capacity [kJ/(K kg)]	Blood flow [W/(K m³)]	Metabolic rate [W/m³]
Pharynx	1,3	0,03	1,006	0	0
Pinealbody	1050	0,53	3,6	709668	126163,2
SAT	916	0,24	2,524	2956,95	591,39
Skin	1100	0,35	3,437	3351,21	3193,506
Skull	1990	0,4	1,289	6702,42	1202,493
Small_intestine	1044	0,56	3,653	139962,3	25626,9
Small_intestine_lumen	1044	0,56	3,9	0	0
Spinal_cord	1038	0,46	3,664	78852	13996,23
Spleen	1054	0,54	3,603	161646,6	29569,5
Stomach	1050	0,53	3,553	57167,7	10250,76
Stomach_lumen	1050	0,56	3,9	0	0
Teeth	2160	0,4	1,34	6702,42	1202,493
Tendon_Ligament	1110	0,5	3,5	17741,7	3154,08
Thalamus	1039	1,13	3,675	78852	13996,23
Thymus	1026	0,52	3,96	709668	126163,2
Tongue	1041	0,53	3,546	3942,6	946,224
Trachea	1100	0,47	3,664	17741,7	3154,08
Trachea_lumen	1,3	0,03	1,006	0	0
Ureter_Urethra	1056	0,46	3,456	17741,7	3154,08
Uterus	1052	0,5	3,58	35483,4	7096,68
Vagina	1044	0,56	3,653	104478,9	18727,35
Vein	1060	0,51	3,824	0	0
Vertebrae	1990	0,4	1,289	6702,42	1202,493

Table A.3-6: Thermal properties including the heat conductivity, the heat capacity, the blood flow and the metabolic rate of the model Roberta.

Louis	Density [kg/m³]	Heat conductivity [W/(mK)]	Heat capacity [kJ/(K kg)]	Blood flow [W/(K m³)]	Metabolic rate [W/m³]
Source: [114] [103] [115] [27] [116] [117] [64]					
Adrenal_gland	1025	0,39	3,128	338175	60120
Air_internal	1,3	0,03	1,006	0	0
Artery	1060	0,51	3,824	0	0
Bladder	1040	0,56	3,9	11272,5	200,4
Blood_vessel	1060	0,51	3,824	0	0
Bone	1990	0,4	1,289	4258,5	764,025
Brain_grey_matter	1039	1,13	3,675	50100	8892,75
Brain_white_matter	1043	0,5	3,621	50100	8892,75
Bronchi	1063	0,46	3,456	11898,75	2129,25
Bronchi_lumen	1,3	0,03	1,006	0	0
Calcaneus_left	1990	0,4	1,289	4258,5	764,025
Calcaneus_marrow_left	1027	0,52	3,96	40080	7139,25
Calcane-	1027	0,52	3,96	40080	7139,25
Calcaneus_right	1990	0,4	1,289	4258,5	764,025
Capitatum_left	1990	0,4	1,289	4258,5	764,025
Capita-	1027	0,52	3,96	40080	7139,25
Capita-	1027	0,52	3,96	40080	7139,25
Capitatum_right	1990	0,4	1,289	4258,5	764,025
Cartilage	1100	0,47	3,664	11272,5	2004
Cerebellum	1040	0,53	3,64	50100	8892,75
Cerebrospinal_fluid	1007	0,6	4,191	0	0
Commissura_anterior	1043	0,5	3,621	50100	8892,75
Commissura_posterior	1043	0,5	3,621	50100	8892,75
Connective_tissue	1013	0,37	3,035	6575,625	1189,875
Cornea	1076	0,52	3,793	0	0
Diaphragm	1041	0,53	3,546	2505	601,2
distalis_I_left	1990	0,4	1,289	4258,5	764,025
distalis_I_right	1990	0,4	1,289	4258,5	764,025
distalis_II_left	1990	0,4	1,289	4258,5	764,025
distalis_II_right	1990	0,4	1,289	4258,5	764,025
distalis_III_left	1990	0,4	1,289	4258,5	764,025
distalis_III_right	1990	0,4	1,289	4258,5	764,025
distalis_IV_left	1990	0,4	1,289	4258,5	764,025
distalis_IV_right	1990	0,4	1,289	4258,5	764,025
distalis_V_left	1990	0,4	1,289	4258,5	764,025
distalis_V_right	1990	0,4	1,289	4258,5	764,025
Ear_cartilage	1100	0,47	3,664	11272,5	2004
Ear_skin	1100	0,35	3,437	2129,25	2029,05
Epididymis	1050	0,53	3,761	450900	80160
Esophagus	1040	0,53	3,5	36322,5	6513
Esophagus_lumen	1050	0,03	1,006	0	0
Eye_lens	1090	0,4	3,664	0	0
Eye_Sclera	1032	0,4	3	93937,5	27555

Louis (continuation)	Density [kg/m³]	Heat conductivity [W/(mK)]	Heat capacity [kJ/(K kg)]	Blood flow [W/(K m³)]	Metabolic rate [W/m³]
Eye_vitreous_humor	1009	0,59	3,932	0	0
Fat	916	0,25	2,524	2129,25	375,75
Femur_left	1990	0,4	1,289	4258,5	764,025
Femur_marrow_left	1027	0,52	3,96	40080	7139,25
Femur_marrow_right	1027	0,52	3,96	40080	7139,25
Femur_right	1990	0,4	1,289	4258,5	764,025
Fibula_left	1990	0,4	1,289	4258,5	764,025
Fibula_marrow_left	1027	0,52	3,96	40080	7139,25
Fibula_marrow_right	1027	0,52	3,96	40080	7139,25
Fibula_right	1990	0,4	1,289	4258,5	764,025
Gallbladder	1026	0,47	3,496	11272,5	2004
Hamatum_left	1990	0,4	1,289	4258,5	764,025
Hamatum_marrow_left	1027	0,52	3,96	40080	7139,25
Hamatum_marrow_righ	1027	0,52	3,96	40080	7139,25
Hamatum_right	1990	0,4	1,289	4258,5	764,025
Heart_lumen	1060	0,51	3,824	0	0
Heart_muscle	1060	0,54	3,72	2505	601,2
Hippocampus	1039	1,13	3,675	50100	8892,75
Humerus_left	1990	0,4	1,289	4258,5	764,025
Humerus_marrow_left	1027	0,52	3,96	40080	7139,25
Humerus_marrow_right	1027	0,52	3,96	40080	7139,25
Humerus_right	1990	0,4	1,289	4258,5	764,025
Hypophysis	1066	0,53	3,761	450900	80160
Hypothalamus	1050	0,53	3,761	450900	80160
Intervertebral_disc	1100	0,47	3,664	11272,5	2004
Kidney_cortex	1049	0,52	3,745	338175	60120
Kidney_medulla	1044	0,52	3,745	338175	60120
Large_intestine	1044	0,56	3,653	66382,5	11898,75
Large_intestine_lumen	1044	0,56	3,9	0	0
Larynx	1082	0,47	3,664	11272,5	2004
Liver	1050	0,51	3,6	85170	15030
Lunatum_left	1990	0,4	1,289	4258,5	764,025
Lunatum_marrow_left	1027	0,52	3,96	40080	7139,25
Lunatum_marrow_right	1027	0,52	3,96	40080	7139,25
Lunatum_right	1990	0,4	1,289	4258,5	764,025
Lung	1050	0,44	3,625	11898,75	2129,25
Mandible	1990	0,4	1,289	4258,5	764,025
Marrow_red	1027	0,52	3,96	40080	7139,25
media_II_left	1990	0,4	1,289	4258,5	764,025
media_II_right	1990	0,4	1,289	4258,5	764,025
media_III_left	1990	0,4	1,289	4258,5	764,025
media_III_right	1990	0,4	1,289	4258,5	764,025
media_IV_left	1990	0,4	1,289	4258,5	764,025
media_IV_right	1990	0,4	1,289	4258,5	764,025
media_V_left	1990	0,4	1,289	4258,5	764,025

Louis (continuation)	Density [kg/m³]	Heat conductivity [W/(mK)]	Heat capacity [kJ/(K kg)]	Blood flow [W/(K m³)]	Metabolic rate [W/m³]
media_V_right	1990	0,4	1,289	4258,5	764,025
Medulla_oblongata	1039	1,13	3,675	50100	8892,75
Meniscus	1098	0,47	3,664	11272,5	2004
Metacarpus_I_left	1990	0,4	1,289	4258,5	764,025
Metacar-	1027	0,52	3,96	40080	7139,25
Metacar-	1027	0,52	3,96	40080	7139,25
Metacarpus_I_right	1990	0,4	1,289	4258,5	764,025
Metacarpus_II_left	1990	0,4	1,289	4258,5	764,025
Metacar-	1027	0,52	3,96	40080	7139,25
Metacar-	1027	0,52	3,96	40080	7139,25
Metacarpus_II_right	1990	0,4	1,289	4258,5	764,025
Metacarpus_III_left	1990	0,4	1,289	4258,5	764,025
Metacar-	1027	0,52	3,96	40080	7139,25
Metacar-	1027	0,52	3,96	40080	7139,25
Metacarpus_III_right	1990	0,4	1,289	4258,5	764,025
Metacarpus_IV_left	1990	0,4	1,289	4258,5	764,025
Metacar-	1027	0,52	3,96	40080	7139,25
Metacar-	1027	0,52	3,96	40080	7139,25
Metacarpus_IV_right	1990	0,4	1,289	4258,5	764,025
Metacarpus_V_left	1990	0,4	1,289	4258,5	764,025
Metacar-	1027	0,52	3,96	40080	7139,25
Metacarpus_V_right	1990	0,4	1,289	4258,5	764,025
Midbrain	1039	1,13	3,675	50100	8892,75
Mucosa	1050	0,34	3,15	11272,5	2004
Muscle	1041	0,53	3,546	2505	601,2
Nerve	1038	0,46	3,664	50100	8892,75
Pancreas	1045	0,49	3,452	51352,5	9143,25
Patella	1990	0,4	1,289	4258,5	764,025
Penis	1060	0,46	3,456	2505	601,2
Pharynx	1,3	0,03	1,006	0	0
Pinealbody	1050	0,53	3,6	450900	80160
Pisiforme_left	1990	0,4	1,289	4258,5	764,025
Pisiforme_right	1990	0,4	1,289	4258,5	764,025
Pons	1039	1,13	3,675	50100	8892,75
Prostate	1045	0,53	3,761	450900	80160
proximalis_I_left	1990	0,4	1,289	4258,5	764,025
proximal-	1027	0,52	3,96	40080	7139,25
proximalis_I_right	1990	0,4	1,289	4258,5	764,025
proximalis_II_left	1990	0,4	1,289	4258,5	764,025

Louis (continuation)	Density [kg/m³]	Heat conductivity [W/(mK)]	Heat capacity [kJ/(K kg)]	Blood flow [W/(K m³)]	Metabolic rate [W/m³]
proximalis_II_right	1990	0,4	1,289	4258,5	764,025
proximalis_III_left	1990	0,4	1,289	4258,5	764,025
proximalis_III_right	1990	0,4	1,289	4258,5	764,025
proximalis_IV_left	1990	0,4	1,289	4258,5	764,025
proximal-	1027	0,52	3,96	40080	7139,25
proximalis_IV_right	1990	0,4	1,289	4258,5	764,025
proximalis_V_left	1990	0,4	1,289	4258,5	764,025
proximalis_V_right	1990	0,4	1,289	4258,5	764,025
Radius_left	1990	0,4	1,289	4258,5	764,025
Radius_marrow_left	1027	0,52	3,96	40080	7139,25
Radius_marrow_right	1027	0,52	3,96	40080	7139,25
Radius_right	1990	0,4	1,289	4258,5	764,025
SAT	916	0,24	2,524	1878,75	375,75
Scaphoideum_left	1990	0,4	1,289	4258,5	764,025
Scaphoideum_right	1990	0,4	1,289	4258,5	764,025
Skin	1100	0,35	3,437	2129,25	2029,05
Skull	1990	0,4	1,289	4258,5	764,025
Small_intestine	1044	0,56	3,653	88927,5	16282,5
Small_intestine_lumen	1044	0,56	3,9	0	0
Spinal_cord	1038	0,46	3,664	50100	8892,75
Spleen	1054	0,54	3,603	102705	18787,5
Stomach	1050	0,53	3,553	36322,5	6513
Stomach_lumen	1050	0,56	3,9	0	0
Talus_left	1990	0,4	1,289	4258,5	764,025
Talus_marrow_left	1027	0,52	3,96	40080	7139,25
Talus_marrow_right	1027	0,52	3,96	40080	7139,25
Talus_right	1990	0,4	1,289	4258,5	764,025
Teeth	2160	0,4	1,34	4258,5	764,025
Tendon_Ligament	1110	0,5	3,5	11272,5	2004
Testis	1044	0,53	3,746	450900	80160
Thalamus	1039	1,13	3,675	50100	8892,75
Thymus	1026	0,52	3,96	450900	80160
Thyroid_gland	1050	0,53	3,553	450900	80160
Tibia_left	1990	0,4	1,289	4258,5	764,025
Tibia_marrow_left	1027	0,52	3,96	40080	7139,25
Tibia_marrow_right	1027	0,52	3,96	40080	7139,25
Tibia_right	1990	0,4	1,289	4258,5	764,025
Tongue	1041	0,53	3,546	2505	601,2
Trachea	1100	0,47	3,664	11272,5	2004
Trachea_lumen	1,3	0,03	1,006	0	0
Trapezium_left	1990	0,4	1,289	4258,5	764,025
Trapezium_marrow_left	1027	0,52	3,96	40080	7139,25
Trapezium_marrow_right	1027	0,52	3,96	40080	7139,25
Trapezium_right	1990	0,4	1,289	4258,5	764,025
Trapezoideum_left	1990	0,4	1,289	4258,5	764,025

Louis (continuation)	Density [kg/m³]	Heat conductivity [W/(mK)]	Heat capacity [kJ/(K kg)]	Blood flow [W/(K m³)]	Metabolic rate [W/m³]
Trapezoideum_right	1990	0,4	1,289	4258,5	764,025
Triquetrum_left	1990	0,4	1,289	4258,5	764,025
Triquetrum_right	1990	0,4	1,289	4258,5	764,025
Ulna_left	1990	0,4	1,289	4258,5	764,025
Ulna_marrow_left	1027	0,52	3,96	40080	7139,25
Ulna_marrow_right	1027	0,52	3,96	40080	7139,25
Ulna_right	1990	0,4	1,289	4258,5	764,025
Ureter_Urethra	1056	0,46	3,456	11272,5	2004
Vein	1060	0,51	3,824	0	0
Vertebrae	1990	0,4	1,289	4258,5	764,025

Table A.3-7: Thermal properties including the heat conductivity, the heat capacity, the blood flow and the metabolic rate of the model Louis.

Femonum	Density [kg/m³]	Heat conductivity [W/(mK)]	Heat capacity [kJ/(K kg)]	Blood flow [W/(K m³)]	Metabolic rate [W/m³]
Source: [114] [103] [115] [27] [116] [117] [64] [98] [97]					
Amniotic_Fluid	1000	0,5	3,84	0	0
Bladder	1040	0,43	3,3	9000	1600
Bladder 2	1040	0,43	3,3	9000	1600
Brain	1030	0,6	4,5	30000	6200
Brain 2	1030	0,6	4,5	30000	6200
CSF	1030	0,6	4,191	0	0
CSF 2	1030	0,6	4,191	0	0
Eyes	1009	0,6	4,05	0	0
Eyes 2	1009	0,6	4,05	0	0
Fetus	1040	0,52	3,73	8000	3200
Fetus 2	1040	0,52	3,73	8000	3200
Heart	1060	0,54	3,72	2000	480
Heart 2	1060	0,54	3,72	2000	480
Hypothalamus	1050	0,53	3,761	360000	64000
Lungs	1050	0,44	3,625	9500	1700
Lungs 2	1050	0,44	3,625	9500	1700
Mother	1100	0,45	3,11	8828	1711
Placenta	995	0,5	3,84	114000	22900
Stomach	1050	0,53	3,553	29000	5200
Stomach 2	1050	0,53	3,553	29000	5200
Umbilical Cord	995	0,4	3,8	2000	480
Umbilical Cord 2	995	0,4	3,8	2000	480
UterusWall Placenta	1030	0,506	3,57	51600	10400

Table A.3-8: Thermal properties including the heat conductivity, the heat capacity, the blood flow and the metabolic rate of the FEMONUM models.

A.4 Temperature Elevation in Children during Magnetic Resonance Imaging

	Spatially localized temperature limit			Average temperature in the head
	Head	Trunk	Extremities	
Louis 170 MHz	2	9	>60	6
Louis 127 MHz	2	5	>60	4
Louis 64 MHz	2	4	12	4
Eartha 170 MHz	3	7	18	7
Eartha 127 MHz	3	6	>60	5
Eartha 64 MHz	3	5	25	5
Roberta 170 MHz	4	14	>60	9
Roberta 127 MHz	4	14	>60	8
Roberta 64 MHz	3	16	>60	6

Table A.4-1: Time needed (in minutes) to exceed the localized temperature limits for a SAR_{WB} of 2 W/kg: Head= 38°C, Trunk= 39°C, Extremities= 40°C. In addition to that, the time needed to elevate the average temperature in the head by 0.5°C was evaluated.

	Spatially localized temperature limit			Average temperature in the head
	Head	Trunk	Extremities	
Louis 170 MHz	< 1	5	>60	3
Louis 127 MHz	< 1	5	>60	2
Louis 64 MHz	< 1	5	5	2
Eartha 170 MHz	< 1	2	13	3
Eartha 127 MHz	< 1	3	>60	2
Eartha 64 MHz	< 1	3	13	2
Roberta 170 MHz	< 1	2	>60	3
Roberta 127 MHz	2	2	>60	3
Roberta 64 MHz	< 1	3	>60	3

Table A.4-2: Time needed (in minutes) to exceed the localized temperature limits for a SARWB of 4 W/kg: Head= 38°C, Trunk= 39°C, Extremities= 40°C. In addition to that, the time needed to elevate the average temperature in the head by 0.5°C was evaluated.